ABSTRACT

DEVELOPMENT OF AN INTEGRATED PHOTONIC SENSOR FOR MONITORING HAZARDOUS ORGANICS

by
DianHong (Diane) Luo

In this study, an integrated photonic sensor has been designed and fabricated for the purpose of monitoring hazardous organics in the environment. The operation of the sensor is based on the principles of the Mach-Zehnder interferometry. The sensor consists of a patterned waveguide structure made of phosphosilicate core and silica cladding. LPCVD processes were developed to produce undoped cladding and doped core silicon dioxide films. Diethylsilane (DES), Trimethylphosphite (TMP) and oxygen were used as the precursors for the deposition process. The effects of the O_2/DES ratio and deposition temperature on the properties of SiO_2 films were investigated. It was observed that the oxide films deposited in the temperature range 550- 700 ^{0}C followed an Arrhenius behavior with an apparent activation energy of 10 KCal/mol. It was found that the optimum conditions to synthesize underlying silicon dioxide films were 775 ^{0}C, 200 mTorr and oxygen to DES flow ratio was 10:1. After 20 hours deposition time under such conditions, the oxide film was ~15 μm thick, stress was compressive with a value of ~20 Mpa, and the refractive index was 1.458. The effect of TMP flow rate on the properties of PSG films was also studied. The composition and refractive index of PSG films varied with temperature and TMP flow rate. Optimum conditions to deposit PSG core layer were found to be at 600 ^{0}C, 250 mTorr, 2 sccm TMP flow rate and an oxygen to DES flow ratio of 10:1.

After 5 hours deposition time under such conditions, Phosphosilicate layer was about 7 μm thick, stress was compressive with a value of 1 Mpa, the refractive index was 1.466, and phosphorous oxide was ~7.5 wt%. The growth rate varied with TMP flow rate and exhibited a maximum value of 254 Å/min at 2.5 sccm and 600 ^{0}C. PECVD processes were used to synthesize the upper cladding silicon dioxide films. The deposition conditions were 250 ^{0}C, 900 mTorr, N_2O flow rate 900 sccm, and 400 sccm SiH_4 (3%) flow rate. After 30 minutes deposition time under such conditions, the oxide film had a thickness of 1.2 μm, stress was compressive with a value of ~110 Mpa, and the refractive index was 1.453. For all deposits, FTIR spectroscopy showed that no carbon was present in the deposits while UV/visible spectroscopy indicated better than 99% optical transmission. Optical analysis proved this integrated photonic sensor could be used as a prototype to monitor the hazardous organics in the environment.

DEVELOPMENT OF AN INTEGRATED PHOTONIC SENSOR FOR MONITORING HAZARDOUS ORGANICS

by
DianHong (Diane) Luo

A Dissertation
Submitted to the Faculty of
New Jersey Institute of Technology
in Partial Fulfillment of the Requirements for the Degree of
Doctor of Philosophy in Materials Science and Engineering

Interdisciplinary Program in Materials Science and Engineering

August 2001

APPROVAL PAGE

DEVELOPMENT OF AN INTEGRATED PHOTONIC SENSOR FOR MONITORING HAZARDOUS ORGANICS

DianHong (Diane) Luo

Dr. Roland A. Levy, Dissertation Advisor — Date
Distinguished Professor of Physics, NJIT

Dr. Gordon A. Thomas — Date
Distinguished Research Professor of Physics, NJIT

Dr. John F. Federici — Date
Professor of Physics, NJIT

Dr. Ivanov Dentcho — Date
Director of Microelectronics Research Center, NJIT

Dr. Matthew Schurman — Date
Director of Operation, Qusion Technology, Inc.

BIOGRAPHICAL SKETCH

Author: DianHong (Diane) Luo

Degree: Doctor of Philosophy

Date: August 2001

Undergraduate and Graduate Education:

- Doctor of Philosophy in Materials Science and Engineering
  New Jersey Institute of Technology, Newark, NJ, 2001

- Master of Science in Metallurgical Engineering
  South Central University of Technology, Hunan, P. R. China, 1992

- Bachelor of Science in Metallurgical Engineering
  Xi'an Institute of Technology, Xi'an, P. R. China, 1989

Major: Materials Science and Engineering

Presentations and Publications:

DianHong Luo and R. A. Levy,
"An Integrated Evanescent Wave Absorbance Sensor For In-Situ Monitoring and Process Control Leading to Reduction of Hazardous Emissions"
(To be submitted)

DianHong Luo and R. A. Levy,
"Fabrication of V-Groove Structures on Silicon"
UNITECH Conference, Newark, NJ, May 2000

DianHong Luo and HongJiu Ren,
"The Study of Extracting Gold from Poor Ore by Three-Phases Fluidization"
The Second Annual Conference of Extracting Technology of Gold and Silver
ShanDong, P. R. China, 1991

To my beloved family

ACKNOWLEDGMENT

I would like to express my deepest appreciation to Dr. Roland A. Levy, who not only served as my research supervisor, providing valuable and countless resources, insight, and intuition, but also constantly gave me support, encouragement, and reassurance.

Special thanks are given to Dr. Gordon A. Thomas, Dr. John F. Federici, Dr. Ivanov Dentcho, and Dr. Matthew Schurman for actively participating in my committee.

Other thanks are given to EPA and the U. S Army for their funding support.

Many of my fellow graduate students in the CVD lab and Microelectrical research center are deserving of recognition for their support. I also wish to thank all the clean room staff for their assistance over the years.

TABLE OF CONTENTS

TABLE OF CONTENTS
(Continued)

TABLE OF CONTENTS
(Continued)

Chapter **Page**

LIST OF TABLES

LIST OF FIGURES

LIST OF FIGURES
(Continued)

LIST OF FIGURES
(Continued)

LIST OF FIGURES
(Continued)

Figure **Page**

CHAPTER 1

INTRODUCTION

The monitoring and control of hazardous emissions is a major concern to industrial and governmental organizations associated with the protection of public health and the environment. Environmental monitoring currently involves collection of air samples that are subsequently analyzed for a large number of hazardous substances such as volatile organic compounds (VOC's). The high cost and time delay associated with such sampling procedure prohibit optimal usage.

Current analytical techniques for environmental monitoring include the Enzyme-Linked Immunosorbent Assay (ELISA) method [1] that provides sensitivity but is complex and other direct detection techniques [2-3] such as surface plasmon resonance [4], grating coupler [5], and RIFS [6] that are relatively less sensitive than ELISA. In this study, we focus on the design, fabrication, and characterization of an integrated photonic sensor that has extremely high sensitivity [7-9] and has the capability of in-situ environmental monitoring [10]. In addition, the sensor has a waveguide structure with an intrinsic reference arm that offers the possibility of reducing thermal drifting defects.

1.1 Mach-Zehnder Interferometer

The operation of the integrated photonic sensor is based on the principle of the Mach - Zehnder interferometer that is an amplitude - splitting device as shown in

Fig. 1.1 [11]. Such an interferometer basically consists of two beam splitters and two totally reflecting mirrors. Two beam waves within the apparatus travel along the separate paths. A difference between the optical paths can be introduced by slightly tilting one of the beam splitters. This difference will result in phase change and interference. The Mach-Zehnder interferometer finds many applications in different fields.

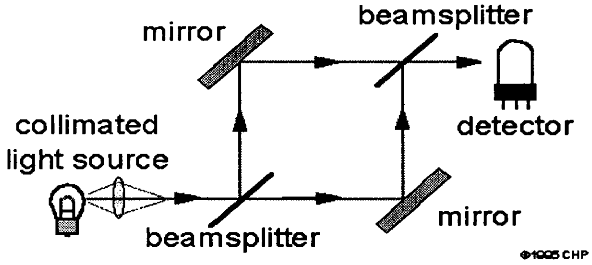

Fig. 1.1 Schematic Mach-Zehnder interferometer

In this study, the silicon processing and optical technology were combined to get the integrated photonic sensor that is essentially a Mach-Zehnder interferometer with sampling capabilities over a large wavelength range (1000-2000 nm). The use of such a sensor permits a shorter active sampling length (~1 cm) as compared to evanescent wave fiber optic sensors (1-10 m) due to the inherent sensitivity of interferometric detection. By using a broad banded light source rather than a single wavelength laser, the interferometer can measure the refractive index difference over the entire near infrared spectrum. Such a detection system would consist of a bright broad banded light source, a coupling lens, optical fibers, and an optical spectrum analyzer (Fig. 1.2).

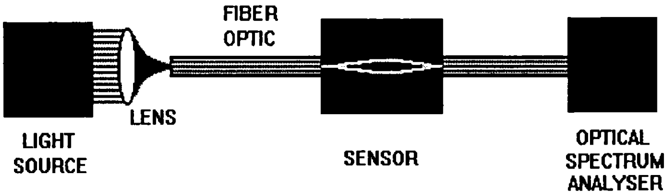

Fig. 1.2 Schematic representation of sensor system

Operation of the sensor, in the interferometric mode, is based on the detection of refractive index changes on waveguide surfaces resulting from the presence of contaminants in the environment. These changes are measured by exposing one arm of a symmertric Mach-Zender interferometer to the analyte, while the other reference arm is protected by an upper cladding layer. The interferometric output can be calculated as a function of refractive index difference between the sampling arm and the reference arm.

The sensor under consideration is a novel device that is based on well-established physical principles [12-14] and one that is non-intrusive for deployment at sites in order to obtain accurate, rapid, and cost effective data. The overall instrument is envisioned to be compact, portable, rugged, and suitable for real time monitoring of organics. An important advantage of this sensor is its size. The distance between the interferometer's arms is on the order of 50 μm while the length of the interferometer is on the order of 1 cm. By placing numerous interferometers parallel to each other, the area of the device occupies an area no bigger than a thumb nail. Another advantage to this approach is the compatibility of the technology with standard silicon-based processing where photolithography and chemical etching steps can be used to mass produce copies of the pattern at a cost of less than a dollar per chip. The use of fiber optics for coupling light in and out of the interferometer offers the additional advantage of remote sensing in environment.

1.1 Chemical Vapor Deposition

The waveguides in this study were fabricated using chemical vapor deposition (CVD), which is a preferred deposition method for a wide range of materials. It is one of the most important methods of film formation used in the fabrication of very large scale integrated (VLSI) silicon circuits, as well as of microelectronic solid state devices in general. In this process, chemical in the gas or vapor phase are reacted at the surface of the substrate where they form a solid product. A large variety of materials, practically all those needed in microelectronic device technology, can be created by CVD. These materials comprise insulators and dielectrics, elemental and compound semiconductors, electrical conductors, superconductors and magnetic material. In addition to its unique versatility, this material synthesis and vapor phase growth method can operate efficiently at relatively low temperature. For example, refractory oxide glasses and metals can be deposited at a temperature of only 300° to 500° C. This feature is very important in advanced VLSI devices with short channel lengths and shallow junctions, where lateral and vertical diffusion of the dopants must be minimized. This also helps in minimizing process-induced crystallographic damage, wafer warpage and contamination by diffusion of impurities.

1.2.1 Fundamental Aspects of CVD

Chemical vapor deposition is the process of chemically reacting a volatile compound of a material to be deposited, with other gases, to produce a nonvolatile solid that deposits atomically on a suitably placed substrate. This product can be in the form of a thin film, a thick coating, or if allowed to grow, a massive bulk. It can be single-crystalline, poly-crystalline, or an amorphous structure. Chemical and physical conditions during the deposition reaction can strongly affect the composition and structure of the product. This deposition technology has become one of the most popular means of creating thin films and coatings in solid state microelectronics where some of the most sophisticated purity and composition requirements must be met. Basic types of CVD include [15]: (1) pyrolysis, (2) reduction, (3) oxidation, (4) compound Formation, (5) disproportionation, and (6) reversible transfer [16].

1.2.2 Thermodynamics of CVD

Thermodynamics addresses several important issues with respect to CVD. It provides an upper limit of what to expect under specified conditions. Thermodynamics does not, however, consider questions related to the speed of the reaction and resulting film growth rates. Indeed, processes that are thermodynamically possible frequently proceed at low rates, due to vapor transport kinetics and vapor-solid reaction limitations, therefore at times unfeasible in practice. Furthermore, the use of thermodynamics implies that chemical equilibrium has been attained. Although this may occur in a closed system, it is not the general case in an open or flow reactor where gaseous reactants and products are continuously introduced and removed. Thus, CVD may be presently viewed as an empirical science with thermodynamic guidelines.

Many simple consequences of thermodynamics with respect to CVD can be understood. For example, consider the requirements for suitable chemical reactions in order to grow single-crystal films. It is essential that a single nucleus form as an oriented seed for subsequent growth. A small negative value of ΔG_v, the chemical free energy per unit volume, is required to foster a low nucleation rate. This, in turn, would require a ΔG^0 value close to zero. If ΔG_v were large, the likelihood of a high rate of heterogeneous nucleation, or even homogeneous nucleation of solid particles within the gas phase, would be enhanced [17]. For analysis of chemical reactions, good values of thermodynamic data are essential. Several sources of this information are listed among the reference [18-19].

1.2.3 Growth Kinetics of CVD

The growth kinetics of CVD films depends on several factors and is always a heterogeneous reaction. The sequence of steps in the usual heterogeneous processes can be described as: (1) Arrival of the reactants, (2) Surface chemistry, and (3) Removal of by-products. These steps are sequential and displayed schematically in Fig.1.3. The slowest process is the rate control step.

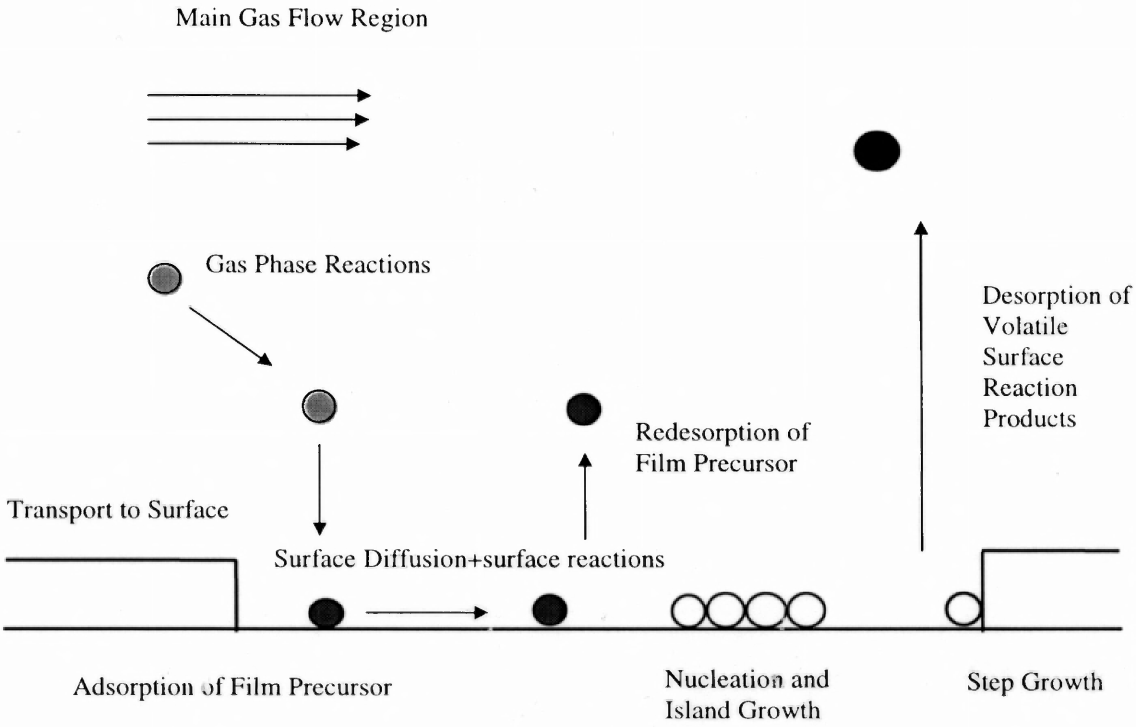

Fig. 1.3 Scheme of transport and reaction processes of CVD

The intimate microscopic details of these steps are usually unknown, and, therefore, the growth kinetics is frequently modeled in macroscopic terms. Grove [20] produced the treatment of kinetics of film growth.

$$C_s = \frac{Cg}{1 + K_s / H_g}$$

$$G = \frac{Ks \times Hg \times Cg}{(Ks + Hg) \times No}$$

Cs – concentration of the reactant at the interface

Cg – concentration of the reactant in the bulk

Ks – rate constant for surface reaction

Hg – gas-phase mass-transfer coefficient

G – film growth rate

No – atomic density or number of atoms incorporated into the film per unit volume

This formula predicts that the surface concentration drops to zero if Ks>>Hg, a condition referred to as mass-transfer control. In this case, low gas transport through the boundary layer is limited regime. Conversely, surface reaction control dominates where Hg>>Ks, in which case Cs approaches Cg. Here the surface reaction is sluggish even through sufficient reactant gas is available.

So, the deposition process can be grouped into: (1) mass-transfer limited regime, and (2) surface-reaction limited regime. If the deposition processes are limited by the mass transfer, the transport process occurred by the gas-phase diffusion is proportional to the diffusivity of the gas and the concentration gradient. The mass transport process which limits the growth rate, G =Hg*Cg/No, is only weakly dependent on temperature (Hg is relatively insensitive to variations in temperature). On the other hand, it is very important that the same concentration of reactants be present in the bulk gas regions adjacent to all locations of a wafer, as the arrival rate is directly proportional to the concentration in the bulk gas. Thus, to ensure films of uniform thickness, the reactors that are operated in the mass-transport-limited regime must be designed so that all locations of wafer surfaces and all wafers in a run are supplied with an equal flux of reactant species. If the deposition process is limited by the surface reaction, the growth rate, G, of the film deposited can be expressed as G = Ks*Cg/ No and Ks ~ exp ($-E_a/RT$) where E_a is the characteristic activation energy - usually 25-100 kcal/mole for surface process, R is the gas constant, and T, the absolute temperature. In the operating regime, the deposition rate is a strong function of the temperature and an excellent temperature control is required to achieve the film thickness uniformity that is necessary for controllable integrated circuit fabrication. On the other hand, under such conditions the rate at which reactant species arrive at the surface is not as important. Thus, it is not as critical that the reactor be designed to supply an equal flux of reactants to all locations of the wafer surface. It will be seen that in horizontal low pressure CVD reactors, wafers can be stacked vertically and at very close spacing because such systems operate in a surface-reaction-rate limited regime. In deposition processes that are mass-transport limited, however, the temperature control is not nearly as critical. As shown in Fig. 1.4, a relatively steep temperature range, and a milder dependence in the upper range, indicating that the nature of the rate-controlling step changes with temperature

The actual film and coating structural morphopogies that develop during CVD are the result of a complex sequence of atomic migration events on substrates leading to observable nucleation and growth process [21]. The two most important variables affecting growth morphologies are vapor super-saturation and substrate temperature. The former influences the film nucleation rate, whereas the latter affects the growth rate. In general, lower temperature and higher gas phase concentration favor formation of polycrystalline deposits. Under these conditions, the arrival rate at the surface is high, but the surface mobility of absorbed atoms is low. Many nuclei of different orientation are formed that upon coalescence result in a film consisting of many differently oriented grains. Further decrease in temperature and increase in super-saturation result in even more nuclei, and consequently in finer – grained films, eventually leading to the formation of amorphous films when crystallization is completely prevented. Amorphous films include oxides, nitrides, carbides and glasses that are of great technical

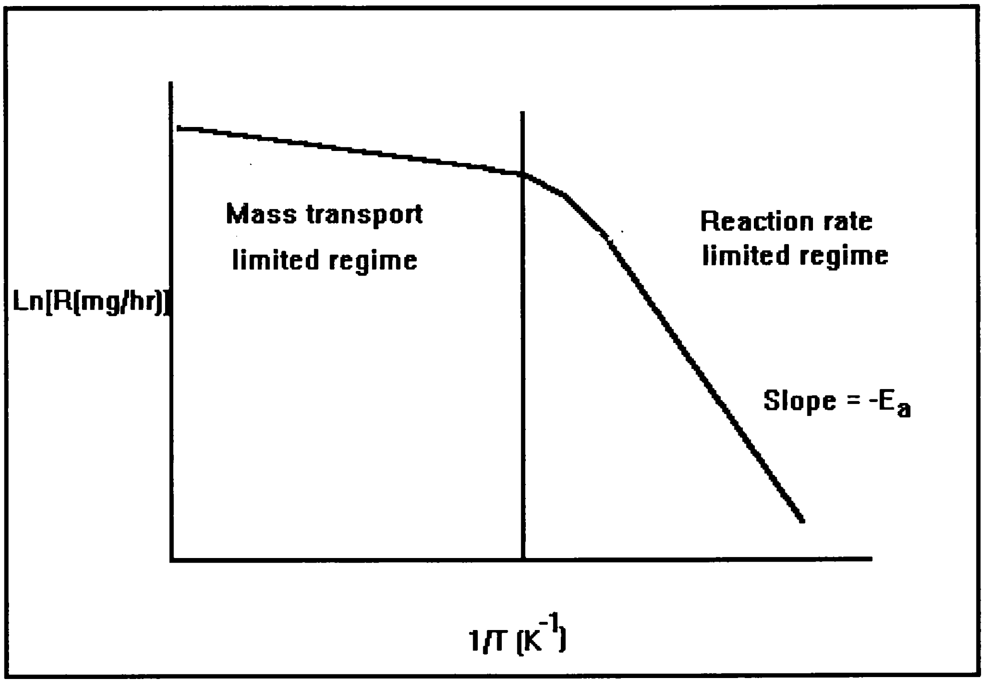

Fig. 1.4 Deposition rate as a function of substrate temperature

importance for microelectronics applications. Single-crystal growth is favored by low gas supersaturation and high substrate temperature.

Deposition variables such as temperature, pressure, input concentrations, gas flow rates, reactor geometry and reactor operating principle determine the deposition rate and the properties of the film deposit.

1.2.4 CVD Processes

The great variety of materials deposited by CVD methods has inspired the design and construction of an equally large number of processes and systems. These have been broadly categorized and described by such terms as low and high temperature, atmospheric and low pressure, cold and hot wall, closed and open in order to differentiate them. Incorporation of physical deposition features such as plasmas and evaporation sources has further enriched and expanded the number of the potential CVD processes.

1.2.4.1 Atmospheric Pressure CVD The reactant gases are allowed into the chamber at normal atmospheric pressure in APCVD. Therefore no vacuum pumps are needed. Energy is supplied by heating the substrate directly. The temperature and the reactant flow rate determine the film growth rate. The advantages of APCVD are high deposition rates, simplicity, and low cost.

The typical application of APCVD is listed in table 1.1. The disadvantage of the APCVD is the tendency towards homogeneous gas phase nucleation, which leads to particle contamination, unless special gas injection techniques are used. The deposition rate and uniformity of the films deposited using CVD process can be determined by the rate of mass transfer of reactant gases to the substrate, or the rate of surface reaction of the reactants gases. In the APCVD, these two rates are of the same magnitude.

Table1.1 APCVD Film Application

Application	Substrate	Thin film	Film properties
Transparent Conductive Oxide LDC's, Solar Cells, Flashtubes, Heating System	Glass (BSG, Soda-Lime)	SnO_2-F	Bulk Resistivity: <600 micro-ohm-cm. Sheet resistance to 10 ohms/sq. greater then 85% Optical Transmission
Anti-Static Films	Glass	SnO_2	5-100 k-ohms/sq. clear, color-less below 400 A
Barrier Undercoat	Soda-Lime Glass	SiO_2	In-line barrier pre-coat for SnO2, 250A to 2500A
Insulator	Glass, Silicon Wafer	SiO_2	Applications from 500A to 2500A
Anti-Reflective Layer Reflective Layer	Glass, Silicon Wafer	TiO_2	2% Refractive index uniformity

1.2.4.2 Low Pressure CVD One of the recent significant developments in CVD processing has been the introduction of low pressure reactor systems for use in the semiconductor industry. These reactors can be divided into hot and cold wall systems. Hot wall systems have the advantage of uniform temperature distribution and reduced convection effects. Cold wall systems are able to reduce the deposition on the wall. These deposits can lead to depletion of deposition species and the formation of the particles, which may flake off the wall and fall on the wafers. For this reason hot wall reactors must be dedicated to the growth of a particular film.

The gas pressure of ~ 0.1 to 1 Torr employed in LPCVD reactors distinguishes it from conventional CVD systems operating at 760 Torr. To compensate for the low pressure, the input reactant gas concentration is correspondingly increased relative to the atmospheric reactor case. Low gas pressure primarily enhanced the mass flux of gaseous reactants and products through the boundary layer between the laminar gas stream and substrates. Since the mass flux of the gaseous specie is given by:

$$J = -\frac{D\times(Pi - Pio)}{\delta\times R\times T}$$

J — mass flux

D — diffusivity

Pi, Pio — the vapor pressure in the bulk and at the surface

δ — thickness of stagnant boundary layer

T – absolute temperature

The diffusivity varies inversely with the pressure. D is roughly 1000 times higher in the case of LPCVD. This more than offsets the increase in δ which is inversely proportional to the square root of the Reynolds number. In an LPCVD reactor, the gas flow is generally a factor 10-100 times higher, the gas density a factor of 1000 lower, and viscosity unchanged to the atmospheric CVD case. Therefore, Re is a factor of 10 to 100 times lower, and δ is about 3 to 10 times larger. Because the change of D dominates that of δ, a mass-transport enhancement of over an order of magnitude can be expected for LPCVD. The increased mean-free path of the gas molecules means that substrate wafers can be stacked closer together resulting in higher throughput. When normalized to the same reactant partial pressure, LPCVD film growth rates exceed those for conventional atmospheric CVD. Instead of a dilute gas, the use of low pressures reduces gas phase nucleation. It is easy to achieve reasonable deposition uniformity in LPCVD.

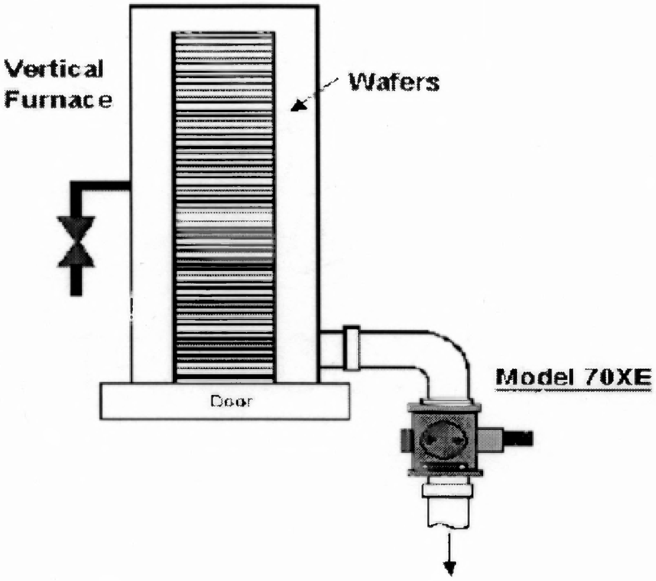

Fig. 1.5 Diagram of vertical LPCVD reactor

The most common reactor is horizontal [22]. This consists of cylindrical quartz tubes heated by wire wound elements. Large mechanical pumps as well as blower booster pumps are required to accommodate the gas flow rates employed—e.g., 50-500 standard cm^3/ min at 0.5 Torr—and maintain the required operating pressure. The problem of LPCVD is the dense adherent deposits that accumulate on the hot wall of the reactors, which may fall down to the wafer.

A recent innovation in the LPCVD area is the introduction of vertical chamber as shown in Fig. 1.5. These systems have several advantages over standard tubes. Since the wafers are all held by gravity, the spacing between the wafers in the reactor is more uniform. Vertical CVD systems are more easily integrated into automated factories since the wafers do not have to be tipped to the vertical allowing easier robotic handling. The most important advantage of vertical LPCVD system is the reduced particle counts. However, the cost of these systems is considerably higher compared to the cost of conventional LPCVD systems.

1.2.4.3 Plasma Enhanced CVD Plasma enhanced chemical vapor deposition (PECVD) is an excellent alternative for depositing a variety of thin films at lower temperatures than those encountered in CVD reactors without compromising film quality. For example, high quality silicon dioxide films can be deposited at < 400^0 C while CVD requires temperatures in the range of 650^0 C to 850^0 C to produce similar quality films.

PECVD uses electrical energy to generate a glow discharge in which the energy is transferred into a gas mixture. Generally, the ratio frequencies employed, range from about 100 KHz to 40 MHz at gas pressures between 50 mTorr to 5 Torr. Under this condition, electron and positive-ion densities number between 10^9 and $10^{12} / cm^3$, and average electron energies range from 1 to 10 eV. This energetic discharge environment is sufficient to decompose gas molecules into a variety of component species, such as electrons, ions, atoms, and molecules in ground and excited states, free radicals, etc. [23] These atomic and molecular fragments interact with a substrate and depending on the nature of these interactions, either etching or deposition processes occur at the substrate. Since the formation of the reactive and energetic species in the gas phase occurs by collision processes, the substrate can be maintained at a low temperature. Hence, film formation can occur on substrates at a lower temperature than is possible in the conventional CVD process, which is a major advantage of PECVD. Some of the desirable properties of PECVD films are good adhesion, low pinhole density, good step coverage and uniformity. Fig..1.6 is the simple diagram of PECVD.

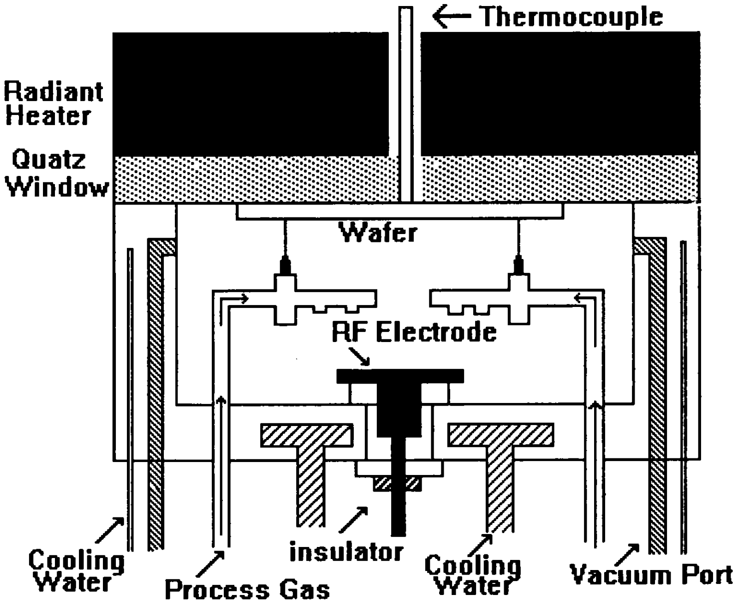

Fig. 1.6 Schematic diagram of PECVD

Semiconductor technology first used plasma CVD and till date remains its major user. Recently plasma has emerged as an application in deposition of films for cutting tools and wear and corrosion protection. The most important materials used in film products are listed in ref. [23-26].

1.2.4.4 Photo-Enhanced CVD This type of process is based on activation of the reactants in the gas or vapor phase by electromagnetic (usually short wave ultraviolet) radiation [27-28]. Selective absorption of photonic energy by the reactant molecules or atoms initiates the process by forming reactive free radical species that interact to form a desired film product. The advantages of this promising CVD process is the low temperature needed to form films and the greatly reduced radiation damage (compared to PECVD). The limitation is the need for photoactivation with mercury to achieve acceptable rates of film deposition.

1.2.4.5 Laser-Enhanced CVD It involves the use of laser and is divided into two types [29]: (1) pyrolysis that uses laser to heat the substrate, decompose the gases and enhance the rates of chemical reactions. (2) photolysis which, on the other hand, involves direct dissociation of molecules by energetic photons. The advantages of these techniques are the spatial resolution and the ability to interface with laser annealing, diffusion, and localized heat treatments. LCVD is still in its early development.

1.2.5 Advantages of CVD

Thin films are used in a host of applications in VLSI fabrication, and can be synthesized by a variety of techniques. Regardless of the method by which they are formed, however, the process must be economical, and the resultant films must exhibit uniform thickness, high purity and density, controllable composition and stoichiometries, high degree of structural perfection, excellent adhesion and good step coverage. CVD processes are often selected over competing deposition techniques because they offer the following advantages:

1. A variety of stoichiometric and non stoichiometric compositions can be deposited by accurate control of process parameters
2. High purity films can be deposited that are free from radiation damage without further processing
3. Results are reproducible
4. Uniform thickness can be achieved by low pressures
5. Conformal step coverage can be obtained
6. Selective deposition can be obtained with proper design of the reactor
7. The process is very economical because of its high throughput and low maintenance costs

1.2.6 Limitations of CVD

Fundamental limitations of CVD are the chemical reaction feasibility and the reaction kinetics that governs the CVD processes. Technological limitations of CVD include the unwanted and possibly deleterious but necessary by-products of reaction that must be eliminated, and also the particle generation induced by homogeneous gas phase nucleation that must be minimized.

Table 1.2 Evaporation vs. Sputtering

Evaporation	Sputtering

A. Production of Vapor Species

1. Thermal evaporation mechanism	1. Ion bombardment and collision momentum transfer
2. Low kinetic energy of evaporation atoms (@ 1200 K , E = 0.1 eV)	2. High kinetic energy of sputtered atoms (E = 2-30 eV)
3. Evaporation rate ~ 1.3 x 10^{17} atoms/cm^2-sec	3. Sputter rate ~ 3 x 10^{16} atoms/cm^2-sec
4. Directional evaporation according to cosine law	4. Directional sputtering according to cosine law at high sputter rates
5. Fractionation of multicomponent alloys, decomposition, and dissociation of compounds	5. Generally good maintenance of target stoichiometry, but some dissociation of compounds
6. Availability of high evaporation source purities	6. Sputter target of all materials are available; purity varies with material

B. The Gas Phase

1. Evaporant atoms travel in high or ultrahigh vacuum ambient (~ 10^{-6} - 10^{-10} torr)	1. Sputtered atoms encounter high pressure discharge region (~ 100 mtorr)
2. Thermal velocity of evaporation 10^5 cm/sec	2. Neutral atom velocity ~ 5 x 10^4 cm/sec
3. Mean-free path is larger than evaporant-substrate spacing; evaporant atoms undergo no collisions in vacuum	3. Mean-free path is less than target-substrate spacing; Sputtered atoms undergo many collisions in the discharge

C. The Condensed Film

1. Condensing atoms have relatively low energy	1. Condensing atoms have high energy
2. Low gas incorporation	2. Some gas incorporation
3. Grain size generally larger than for sputtered film	3. Good adhesion to substrate
4. Few grain orientations (textured films)	4. Many grain orientations

1.3 Physical Vapor Deposition

Physical vapor deposition (PVD) is mainly divided into two categories, evaporation and sputtering. The objective of these deposition techniques is to controllably transfer atoms from a source to a substrate where film formation and growth proceed atomically, without the need of a chemical reaction. In general, the properties of the film obtained by PVD are governed by the following: evaporation rate of the atoms, vapor pressure of the target materials, deposition geometry, temperature, pressure, and thermal history of the substrate [30]. In sputtering technique, the properties of the film are also decided by the power, radio frequency, bias, and magnetron variants. A comparison of the two is given in Table 1.2

1.4 Photolithography

Fabrication of micro electro mechanical devices or optic devices on a silicon substrate requires working on a tiny region of the substrate. The patterns that define such regions are created by lithography, which is the process of drawing or painting the pattern of an integrated circuit in a resist material. Photoresist materials are first spin coated onto the wafer substrate. Next the resist layer is selectively exposed to a form of radiation, such as ultra violet light, electrons, or x rays. An exposure tool and mask, or a data tape in electron beam lithography is used to affect the desired selective exposure. The patterns in the resist are formed when the wafer undergoes the subsequent "development" step. The areas of the resist remaining after development protect the substrate regions they cover. Locations from resist that have been removed can be subjected to a variety of additive or subtractive processes that transfer the pattern onto the substrate surface.

In the lithographic process, firstly the photoresist (PR) is applied as a thin film to the substrate (e.g. SiO_2 on Si), and subsequently exposed through a mask. The mask contains clear and opaque features that define the pattern to be created in the PR layer. The PR area that is exposed to light is made soluble or insoluble in a specific solvent known as developer. In the case when irradiated (exposed) regions are soluble, a positive image of the mask is produced in the resist. Therefore, such a material is termed as a positive photoresist. On the other hand, a negative image results if the non-irradiated regions are dissolved by the developer. Hence, the resist is termed as a negative resist. After development, the regions of SiO_2 no longer covered by resist, are removed by etching, thereby replicating the mask pattern in that oxide layer.

The resist performs two roles in this process. First, it responds to the exposing radiation in such a way that mask image is replicated in the resist. Second, the remaining areas of resist protect the underlying substrate during subsequent processing. In fact the name resist evolved from the ability to resist etchants.

Although both negative and positive resists are used to manufacture semiconductor components, the higher resolution capabilities of positive resists have virtually made them exclusive choice for VLSI applications. Conventional positive optical lithographic processes and resists are capable of producing images on VLSI substrates with dimensions as small as 0.8-1.5μm. For submicron features, however, the diffraction effects during exposure may ultimately cause other higher resolution techniques to replace optical lithography.

1.5 Etching

Etching in microelectronic fabrication is a process by which material is removed from the silicon substrate or from thin films on the substrate surface. The mask layer is used to protect specific regions of the wafer surface. The goal of etching is to remove the material that is not covered by the mask.

In general etching process is not completely attainable. That is, etching process is not capable of transferring the pattern established by protective mask into the underlying material. Degree to which the process fails to satisfy the ideal is specified by two parameters: bias and tolerance. Bias is the difference between the etched image and mask image. Tolerance is a measure of statistical distribution of bias values that characterizes the uniformity of etching. The rate at which material is removed from the film by etching is known as etch rate. The units of etch rate are Å/min, µm/min, etc. Generally high etch rates are desirable as they allow higher production throughputs, but in some cases high etch rates make the control of lateral etching a problem. That is since material removal can occur in both horizontal and vertical directions, the horizontal etch rate as well as vertical etch rate may need to be established in order to characterize an etching process. The lateral etch ratio, L_R, is defined as the ratio of the etch rate in a horizontal direction to that in a vertical direction. Thus:

$$L_R = \frac{\text{Horizontal etch rate of material}}{\text{Vertical etch rate of material}}$$

In the case of an ideal etch process, the mask pattern would be transferred to the underlying layer with a zero bias. This would then create a vertical edge of the mask. Therefore the lateral etch rate would also have to be zero. For nonzero L_R, the film material is etched to some degree under the mask and this effect is called undercut. When the etching proceeds in all directions at the same rate, it is said to be isotropic. Then by definition, however, any etching that is not isotropic is anisotropic. If etching proceeds exclusively in one direction (e.g. only vertically), the etching process is said to be completely anisotropic. The typical isotropic and anisotropic etch profile is shown in the Fig. 1.7.

So far, it has been assumed that the mask as well as the layers under the mask was not attacked by the etchant. In fact both the mask and the underlying layer materials are generally etchable, and these effects may play a significant role in specifying etch processes. The underlying material subject to attack may either be the silicon wafer itself, or a film grown or deposited during a previous fabrication step. The ratio of the etch rates of different materials is known as selectivity of an etched process. Thus both the selectivity with respect to the mask material and the selectivity with respect to the substrate materials are important characteristics of an etch process.

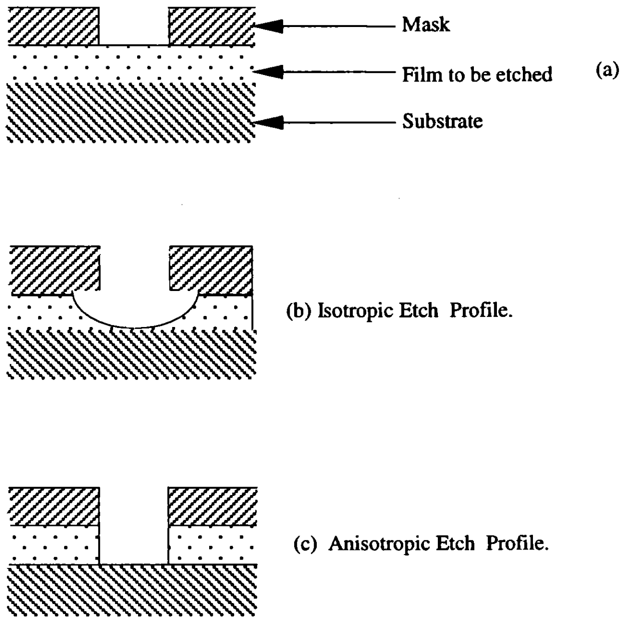

Fig. 1.7 In the process of mask-layer definition and subsequent pattern transfer, a wafer must be patterned before plasma etching. Features may be etched isotropically or anisotrpically .

1.5.1 Wet Etching

Wet etching is purely a chemical process that can have serious drawbacks: a lack of anisotrophy, poor process control, and excessive particle contamination. However, wet etching can be highly selective and often does not damage the substrate. As a result, even though the process is much less popular than it once was, it continues to be used for a wide range of "noncritical" tasks.

Since the reactive species are normally present in the etchant solution, wet chemical etching consists of three processes: movement of the etchant species to the surface of the wafer, a chemical reaction with the exposed film that produces soluble byproducts, and movement of the reaction products away from the substrate of the wafer. Since all three steps must occur, the slowest one, called the rate limiting step, determines the etch rate. Since it is generally desirable to have a large, uniform, well controlled etch rate, the wet etch solution is often agitated in some manner to assist in the movement of the etchant to the surface and the removal of the etch product. Some wet etc processes use a continuous acid spray to ensure a fresh supply of the etchant.

For most wet etch processes, the film to be etched is not directly soluble in the etchant solution. It is usually necessary to change the material to be etched from a solid to a liquid or a gas. If the etching process produces a gas, this gas can form bubbles that can prevent the movement of fresh etchant to the surface. This is an extremely serious problem since the occurrence of the bubbles cannot be predicted. This problem is most pronounced near the pattern edges. In addition to assisting the movement of fresh etchant chemicals to the surface of the wafer, agitation in the wet chemical bath may also reduce the ability of the bubbles to adhere to the wafer. Even in the absence of bubbles, small geometry features may etch slowly, due to the difficulty in removing of the etch products. This phenomenon has shown to be related to microscopic bubbles of trapped gas [31]. Another common problem for wet etch processes is undetected resist scumming. This occurs when some of the exposed photoresist is not removed in the develop process. Common causes are incorrect or incomplete exposures and insufficient developing of the pattern. Due to their high selectivity, even a very thin layer of resist residue is sufficient to completely block the wet etch process [32].

1.5.2 Dry Etching

Wet etching processes are typically isotropic. Therefore if the thickness of the film being etched is comparable to the minimum pattern dimension, undercutting due to isotropic etching becomes intolerable. One alternative pattern transfer method that offers the capability of non-isotropic (or anisotropic) etching is "dry etching". As a result, considerable effort has been expended to develop dry etch processes as replacements for wet etch processes.

As mentioned earlier, the overall goal of an etch process is to be able to reproduce the features on the mask with fidelity. This should be achievable together with control of following aspects of etched features:

1. The slope of the feature sidewalls (e.g. the slope of the sidewalls of the etched feature should have the desired angle, in some cases vertical)
2. The degree of undercutting (i.e. usually the less undercutting the better)

There are a variety of dry etch processes. The mechanism of etching in each type of process can have a physical bias (e.g. glow-discharge sputtering), a chemical bias (e.g. plasma etching), or a combination of the two (e.g. reactive ion etching (RIE), and reactive ion beam etching (RIBE))

In processes that rely predominantly on the physical mechanism of sputtering (including RIBE), the strongly directional nature of the incident energetic ions allows substrate material to be removed in a highly anisotropic manner (i.e. essentially vertical etch profiles are produced). Unfortunately such material mechanisms are non selective against both masking material and materials underlying the layers being etched. That is, the selectivity depends largely on sputter yield differences between materials.

On the other hand, purely chemical mechanisms for etching can exhibit very high selectivity against both mask and underlying substrate material. The basic concept of plasma etching is rather direct. A glow discharge is utilized to produce chemically reactive species from a relatively inert molecular gas. The etching gas is chosen so as to generate species that react chemically with the material to be etched, and whose reaction product is volatile. Such purely chemical etching mechanisms, however, typically etch in an isotropic fashion.

By adding a physical component to a purely chemical etching mechanism, however, the shortcomings of both sputter based and purely chemical dry etching process can be surmounted. Plasma etching process is a purely chemical process and reactive ion etching processes is a physical/chemical process.

An ideal dry etch process based solely on chemical mechanisms for material removal, can thus be broken down into six steps: (1) Reactive species are generated in a plasma, (2) These species diffuse to the surface of the material being etched, (3) The species are absorbed on the surface, (4) A chemical reaction occurs with the formation of a volatile by product, (5) The by product is desorbed from the surface, (6) The desorbed species diffuse into the bulk of the gas

If any of these steps fail to occur, the overall etch process ceases. Many reactive species can react rapidly with a solid surface, but unless the product has a reasonable vapor pressure so that desorption occurs, no etching takes place.

CHAPTER 2

REVIEW OF LITERATURE

In this chapter, a history review of the optical sensor, a development of the Mach-Zehnder interferometer, and the deposition techniques of the waveguide will be discussed. A brief comparison of the properties of silicon dioxide films deposited by different techniques will also be made.

2.1 Integrated Optical Sensor

2.1.1 Introduction of Optical Fiber Sensor

Optical sensors exhibit interesting properties for sensing physical and chemical magnitudes. The most significant advantages of optical sensors are their immunity to electromagnetic interference, non-interactivity with the sensor environment, low loss for long length sensing, flexibility for easy distribution, and high sensitivity.

The fiber sensors use an optical fiber as a transmission line of the light signal and as a sensing element also. Temperature fiber sensors used in high voltage environment, gas pipe, and storage vessels already have some practical applications. Their performance was discussed in ref. [33]. Their resolution is listed in table 2.1. Strain fiber sensor has reached nearly practical level [34] as shown in Fig 2.1. During recent years, the fiber-optic evanescent wave sensors have been coming up. New spectroscopic techniques in the infrared (IR) and near-

Table 2.1 Resolution of temperature fiber sensor at different time

Year	**Spatial Resolution (m)**	**Temperature Resolution (^{0} C)**	**Range (Km)**
1995	600	6.5	12.9
1996	130	1.4	12.9
1997	40	2.9	12.9
1997	10	1.4	6
1998	3	1.4	16
End of 1998	2	1	20

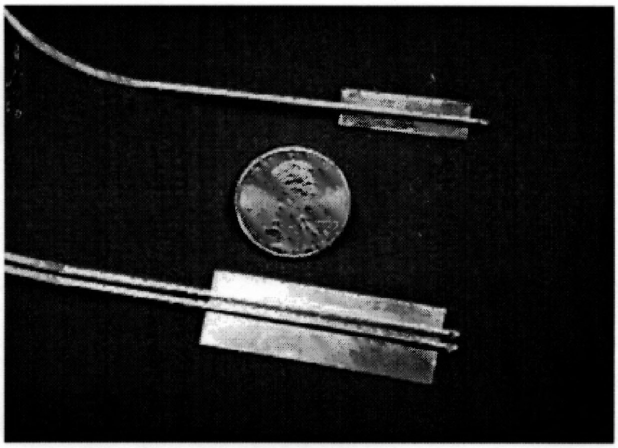

Fig. 2.1 Picture of strain optic fiber sensor

infrared (NIR) spectral region for the detection of non-polar organic substances in water based on the evanescent wave sensing principle are promising [35-41]. These techniques combine the enrichment of organic analyte molecules in the hydrophobic polymer coating of a light-conducting internal reflection element (IRE) with the direct spectroscopic measurement of the “extracted ” species in the polymer. Polyethylene in the IR region [42-43], and polyalkyl (aryl) siloxanes in the NIR region [44] are two favorable cladding materials to construct evanescent wave sensors for non-polar organic species. Whereas the mid-IR spectral region contains much useful qualitative and quantitative information, mid-IR fibers are not available in lengths longer than a few meters and still suffer from poor mechanical, chemical stability and high transmission losses. So they are not suitable for remote sensing application at present. Therefore, the NIR region is currently used for the multicomponent analyses with the optical fibers allowing distances of up to a few hundred meters between spectrometer and sensing element. This kind of fiber sensor can be used to quantitatively determinate the concentration of chlorinated hydrocarbons, aromatic substances, crude oil, fuel oil, and residual distillates [45-49] in the water. The limits of detection are listed in table 2.2 [36].

Table 2.2 Limits of detection of non-polar organic substances obtained using an NIR fiber-optic evanescent wave sensor

Substances	Limits of detection (mg/l or ppm)
Dichloromethane	80
Trichloromethane	18
1,1-Dichloroethene	1.3
Trichloroethene	0.8
Toluene	0.9
Chlorobenzene	0.4
P-Xylene	0.4
1,2,4,-Trichlorobenzene	0.1

The fibers used for these experiments were polydimethylsiloxane-clad silica fibers with fiber lengths of up to 10.58 m that were coiled as a spiral on a Teflon support of cylindrical geometry. The set-up is discussed in detail in reference [50].

The limits of the optical fiber sensor include poor mechanical stability, long response time, lack of the integration, and the difficulty of performing multiple tests simultaneously [51].

2.1.2 Development of Mach-Zender Interferometer

The term "integrated optics" was coined in the late 1960s to emphasize the similarities between planar optical circuit technology and the integrated electronics technology. The first optical waveguides, fabricated in the late 1960s and early 1970s, were two-dimensional, or planar, devices. By the mid 1970s, three-dimensional waveguides were demonstrated in a variety of materials - from glass to semiconductors. Integrated optics covers a wide variety of devices types [52]. The combination of integrated optics and micromechanical structure on silicon creates a new class of microoptoelectromechanical (MOEM) devices and offers new integration potentials for sensing applications. It is possible to build an optical sensor by using waveguides that guide the light by altering the refractive index of one of the guiding region, therefore developing a phase change. The Mach-Zehnder interferometer (Fig. 2.2) is one of these integrated optical sensors, which has two arms. Light is divided by Y-splitter into 50/50 and goes through the two arms, then two half light signals will combine at the other Y-splitter. The interference will occur if there is phase shift between two half signals. The detector can catch the change of intensity and analyze the results.

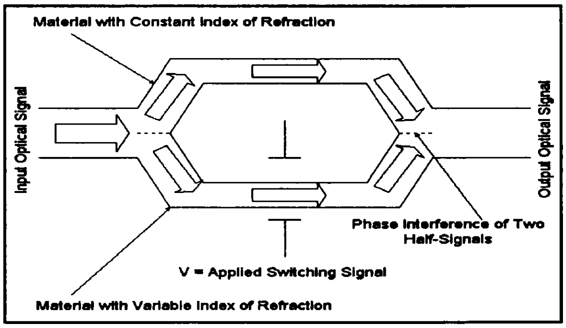

Fig. 2.2 Schematic diagram of Mach-Zender interferometer

The Mach-Zehnder interferometer was used as an acoustooptic phase modulator [53] based on the change in the index of refraction caused by mechanical strain that was introduced by the passage of an acoustic wave. It can also be used as the thermooptic phase modulator [54] to detect temperature. The active device of the Mach-Zehnder interferometer was usually made in Ti diffused $LiNbO_3$, which was used as the electrooptic phase modulator [55]. The Mach-Zehnder interferometer with multiple arms acted as the variable ratio power splitter [56] or the switch [57] (Fig. 2.3).

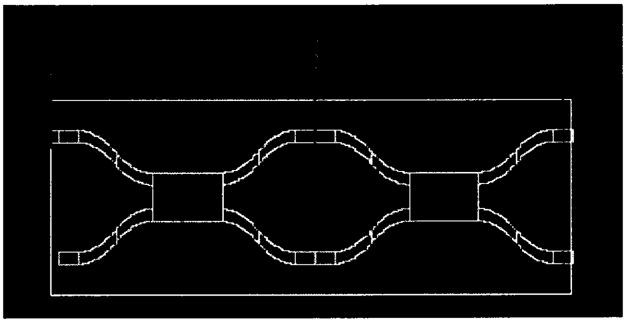

Fig. 2.3 MMI-based Mach-Zehnder (MZI) switch

The developments of the Mach-Zehnder interferometer include a three-waveguides coupler structure at the output [58], which had been thought as the first non-trivial example of NxN-multiport interferometer. The integrated III-V semiconductor waveguide structures have seen the significant progress in recent years. InGaAsP based on the Mach-Zehnder modulator was used in the high speed transmission system [59]. Unbalanced GaAlAs-GaAs integrated Mach-Zehnder interferometer [60] worked as a coding/decoding module.

2.1.3 Proposed Mach-Zehnder Interferometer

The proposed Mach-Zehnder interferometer was used to measure the concentration of the hazardous organics in the environment. The miniaturization of the sensor allowed it to be in-situ monitoring, which found much benefit in the biomedical field. The image of interference using the Mach-Zehnder interferometer was first observed in 1969 [61].

The integrated optic interferometer had been developed for one step, label-free detection of toxins and biological agents. The potassium(KNO_3) ion-exchange-channel-waveguides device in the glass substrate was produced by the standard processing steps and the appropriate photomasks [62]. Antibodies were applied to the glass surface to provide a bioselective coating for a specific biological agent. The device measured the change of the refractive index at the surface of a planar waveguide using interferometry and found the concentration of toxins in blood and bio-warfare agents.

Table 2.3 Measurement limits of KNO_3 ion-exchange channel waveguides

Assay	**Limits (mg/l or ppm)**
Human IgG (hIgG)	100
Ricin toxin	50
Staphylcocus Enterotoxin-B (SEB)	50

Heidman and Kooyman used silicon wafers to fabricate the integrated Mach-Zehnder interferometers that can measure the concentration of 2.5×10^{-8} M (1 mg/l or 1 ppm) [63] of the antigen HCG and 5×10^{-11} M of a 40 K Da protein [64]. They used the evanescent field of the planar optical waveguides as the sensing elements. The waveguides used were optimized to obtain a steep dependence of the propagation velocity on the refractive index near the surface. The absorption of a layer of proteins thus resulted in a phase change that was measured interferometrically using a Mach-Zehnder interferometer set-up. This highly sensitive sensor had a cross section as shown in Fig. 2.4. However, a disadvantage of this earlier optical sensor was its "bulky" structure that made it complex in operation and impossible for the development of the future multichannel sensors.

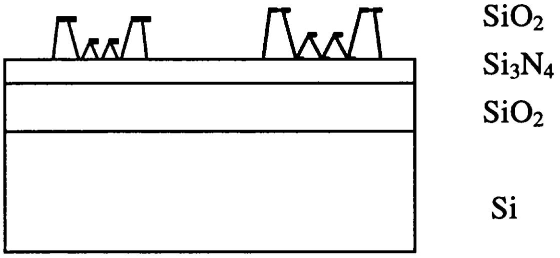

Fig. 2.4 Cross section of bulky waveguide structure

Schipper and Brugman developed more integrated and less complex Mach-Zehnder interferometer sensors [65-66]. They used 1.5 mm thermally oxidized SiO_2 layer with a refractive index of 1.46 as the lower cladding layer. On this SiO_2 layer a LPCVD Si_3N_4 waveguide layer with a high refractive index of 2.0 and a 1.5 μm PECVD SiO_2 cladding layer with a refractive index 1.46 were deposited. The high contrast of the refractive indices between waveguide and cladding was chosen to get maximum sensitivity [67-68]. The cross section of this integrated Mach-Zehnder device can be seen in Fig. 2.5. Jimenez and Bartolome had proposed the design of this Mach-Zehnder interferometer [69]. The limit was difficult to get single mode in the waveguide because of the big difference between the refractive indices. Therefore, the result is not accurate enough.

The critical sensor [70] is a new type of evanescent wave immunosensor that overcomes the drawback of the optical alignment; but it lacks the high sensitivity.

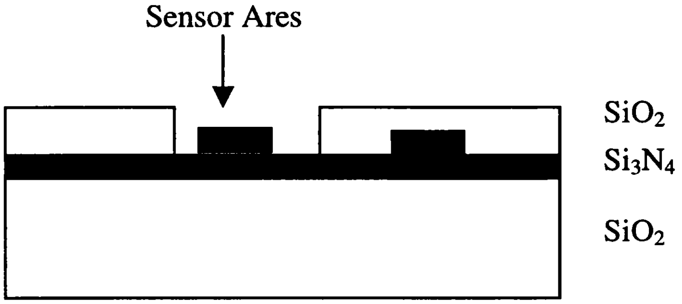

Fig. 2.5 Cross section of Mach-Zehnder interferometer

2.1.4 Waveguide Technology

Practical optical waveguiding has been demonstrated in a wide range of optical materials, including silicon on insulator, silicon oxynitride [71-72], silicon nitride, poly-Si [73], lithium niobateh [52], and silicon oxide. The use of silicon waveguiding technology for optoelectronic components is becoming attractive because silicon manufacture is so mature and the wafer processes offer a scalable route to integration. This maturity in the very high volume manufacturing has made processes controllable and readily available.

The rib-waveguide [74] structure as shown in Fig. 2.6 was built in Silicon On Insulator (SOI) [75-76] wafer. Light is almost entirely confined into silicon, but extends deeply into the planar silicon layer around the ridge due to a small effective index difference in the lateral direction. This combination allows single-mode operation. Another advantage of the SOI waveguide is the possibility of making directional couplers (DC) efficient along the SOI layer. In the design of directional couplers, it must be taken into account that the coupling occurs when bent waveguides approach or diverge from each other in the DC' s ends. The SOI waveguides with the tight bends radiate light due to the small horizontal index difference. However, the high index difference between silicon and silica offers the possibilities for sharp bends via e.g. mirrors or photonic bandgap (PBG) structure. SOI wafers with a "buried oxide" layer were found to be a convenient approach, since the wafer material was readily available and the buried oxide layer was useful as a reference surface. SOI wafers are typically made using either the SIMOX process (separation by implantation of oxygen) or a bond and etch back process.

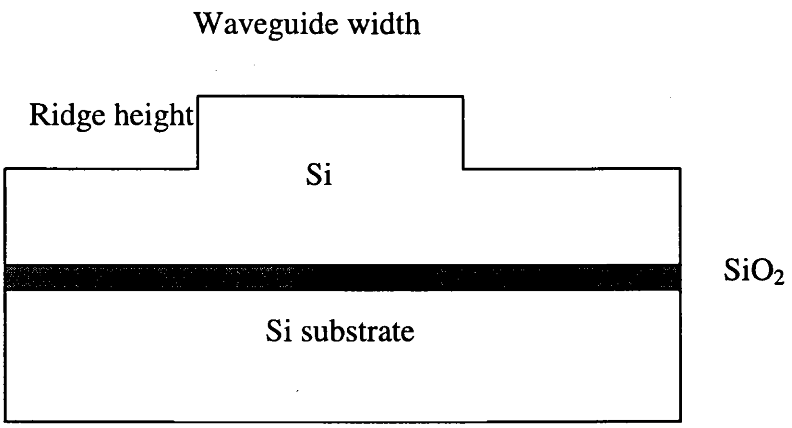

Fig. 2.6 SOI rib waveguide dimensions

Silicon oxinitrides are another choice material for the fabriction of waveguides. Application [77] of this material has been motivated by its excellent optical properties, such as low absorption losses in the visible and near infrared wavelength range. Moreover, impurity doping during the layer growth allows that the refractive index of SiON thin film can be easily adjusted over a large range, i.e., between 1.45 (SiO_2) to 2.0 (Si_3N_4). This large flexibility in choosing the refractive index adds the attractiveness of this material for the designers of integrated optical devices. Depending on the application, different dopants and growth methods can be used. The deposition technologies of silicon oxynitride include: (1) plasma enhanced chemical vapor deposition which use 2% SiH_4-N_2, N_2O, and NH_3, and apply a parallel-plate Electrotech 210 PECVD machine with a low frequency RF-source (187.5KHz); (2) low pressure chemical vapor deposition which use SiH_2Cl_2, O_2 and NH_3 applying a Tempress hot-wall LPCVD reactor.

Silicon nitride waveguide [71] technology offers many types of sensor devices that can be operated with the visible to infrared wavelengths. Etched Si_3N_4 surface had been applied in the integrated optical surface plasmon resonance acting as a mirror. The evanescent wave coupling can be exploited with the sensitive layer on the top of waveguide to make interferometric sensor, which had been discussed before. The large difference of the refractive index between silicon nitride and the surrounding silicon dioxide enable the small radius of curvature in the bent waveguides that had been applied to fabricate the integrated optical ring resonators.

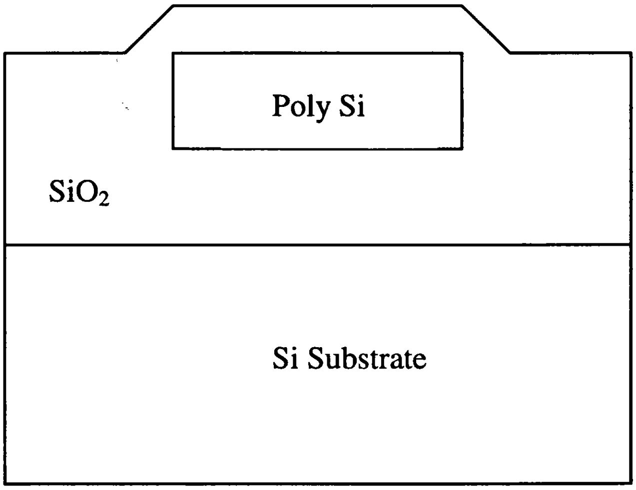

Fig. 2.7 Strip waveguide cross section of poly-Si/SiO_2

Polycrystalline silicon (poly-Si)/SiO_2 [73] is an attractive waveguiding structure that offers significant advantages in both applications with its compact size and compatibility with multilevel CMOS process. Silicon, together with silicon dioxide, forms a high contrast system with a core/cladding index difference of 2.0. This allows silicon waveguide dimensions to be below a micro and enables an optical power distribution system with multiple fanouts to be made in a very small fraction of the chip area. Such dimensions can be compared to those of glass waveguides, which are several orders of magnitude larger. The ease of fabrication and integration with current CMOS technology gives poly-Si / SiO_2 waveguides an added advantage over single crystal silicon/ SiO_2 waveguides. The polycrystalline nature of the guiding materials, however, causes transmission loss which can be attributed to bulk absorption and surface scattering. Using low temperature, crystallization of amorphous silicon achieves smooth surface, which reduced the loss to 10 dB/cm. Fig. 2.7 is the structure of poly-Si/SiO_2 waveguide.

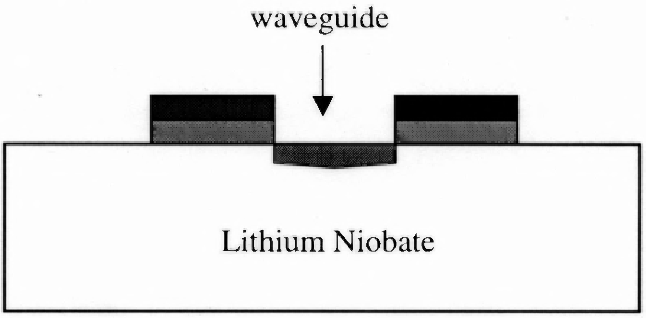

Fig. 2.8 Scheme of a Lithium Niobate integrated optical component

The earlier integrated optics technologies were mainly based on active material like $LiNbO_3$. The manufacturing of $LiNbO_3$ integrated optic components includes the stages-wafer fabrication and the chip package [52]. $LiNbO_3$ wafer fabrication processes are broadly similar to those used for manufacture silicon integrated electronics. Generally, in the industry, the three-inch wafers of $LiNbO_3$ are used since the integrated optical devices tend to be long and thin (typically 2-

mm wide by 40-mm long). Fully processed wafers contain 10-50 devices, depending on the detailed design. The majority of $LiNbO_3$ IOCs are electro-optic. They have both optical and electrical inputs, where the electrical signal controls the optical properties of the devices. As a result, the wafer fabrication is a two-stage process with the formation of the optical layer followed by the electrical layer. The schema of $LiNbO_3$ integrated optical components is shown in Fig. 2.8.

Silica-on-silicon integrated optical devices are expected to have a major impact on the optical networks and the optical signal processing. Silica waveguide on silicon substrate has the following advantages [78]:

1. Optical integrated circuit require low cost substrate that are flat, extremely smooth, and large in area. Commercially available silicon substrates are ideal to this application.
2. Silica is extensively used in the silicon integrated circuit industry and for the manufacture of optical fibers. It has stable well-controlled refractive index and is highly transparent. SiOB waveguide can be entirely processed with the commercially available equipment of this industry.
3. Optical fibers are also made from SiO_2. So that use of an index matching oil or elastomer between waveguide and optical fiber results in a nonreflecting interface. Silica is inherently low loss optical material. Polymer materials have weak vibronic absorption band at optical communication waveguide (high loss). The thermal expansion coefficient of Si is greater than that of doped SiO_2, causing the film to be more

compressive strained after annealing. A film in compression is more stable against cracking.

4. Silicon has good thermal conductivity and can be used as a laser submount.

The silica waveguide made of ASG (arsenosilicate glass) [79] is in the application where the large packing density is essential, the direct coupling to semiconductor lasers is required, or the tight optical confinement allows very small devices to be made. ASG can be produced by CVD technique that is stable, easily processed at relatively low temperatures, and more importantly, can easily control the refractive indices. By controlling the level of arsenic doping in the film, the refractive index can be varied from 1.47 to 1.52. The main disadvantage of this approach is the high loss anticipated when coupling the very small guides to the system fiber. Another waveguide material is PSG (Phosphorous doped SiO_2) [80]. The PSG channel waveguide used in the optical ring resonator has the optical loss of 1 dB/cm at the visible wavelength. The single mode waveguide of PSG with very low loss (0.05 dB/cm at wavelength 1.5μm) was reported. PSG can be obtained by CVD process and will be discussed later.

2.2 Synthesis of Silicon Dioxide

Silicon dioxide is a very important dielectric film in the semiconductor technologies and also a very useful integrated optical material. It could be developed by various methods for different usages [81]: (1) thermal oxidation, (2) sputtering, (3) microwave plasma assisted chemical vapor deposition (MPACVD), (4) plasma enhanced chemical vapor deposition (PECVD), (5) low pressure chemical vapor deposition (LPCVD), (6) flame hydrolysis deposition (FHD), and (7) sol-gel deposition (SGD). Thermal oxidation and sputtering are limited by the doping and growth rate. PECVD has been discussed in Chapter 1. MPACVD is cost-efficient and has a high growth rate although the film is high stress. FHD has a rapid deposition rate [82], but it suffers from the high deposited temperature and high loss when coupling with small Δn.

Table 2.4 Summary of fabrication methods for integrated optics

Methods	Material system	Laboratory	Location
MPACVD	GeO_2:SiO_2/SiO_2 Si_3N_4/SiO_2	GEC GEC	Middlesex, UK
PECVD	Si_3N_4/SiO_2 P_2O_5:SiO_2/SiO_2 P_2O_5:SiO_2/SiO_2	LETI LETI BNR Europe	Grenoble, France Grenoble, France Harlow, UK
LPCVD	Si_3N_4/SiO_2 P_2O_5:SiO_2/SiO_2 As_2O_3:SiO_2/SiO_2	Lucent Lucent BTRL	Murry Hill, USA Murry Hill, USA Ipswich, UK
FHD	TiO_2:SiO_2/SiO_2 GeO_2:SiO_2/SiO_2 TiO_2:SiO_2/SiO_2 GeO_2:SiO_2/SiO_2	NTT NTT Furukawa Electri Co PIRI	Ibaraki, Japan Ibaraki, Japan Chiba, Japan Columbus, USA
SGD	TiO_2:SiO_2/SiO_2 GeO_2:SiO_2/SiO_2	Imperial College Imperial College	London, UK

2.2.1 LPCVD of SiO_2

LPCVD of silicon dioxide is generally based on the reaction of silane and oxygen:

$$SiH_4 + O_2 \text{===>} SiO_2 + 2H_2$$

Various new precursors are now coming up in the place of silane not only for generating good quality films and optimizing the deposition conditions, but also for the safety purpose because silane is a toxic, pyrophoric and potentially explosive gas. Some of these precursors are listed in the table 2.5. Most of the work has been done with TEOS, using both LPCVD [83-88] and PECVD [89-97] techniques. Optimum deposition conditions and their effects on the deposit properties [98] have been shown in table 2.6 and table 2.7.

Table 2.5 New precursors of CVD SiO_2

Name	Formula
Tetraethoxysilane (TEOS) [99]	$Si(OC_2H_5)_4$
Ethyltriethoxysilane [99-102] (ETOS)	$C_2H_5Si(OC_2H_5)_3$
Amyltriethoxysilane [99,100]	$C_5H_{11}Si(OC_2H_5)_3$
Vinyltriethoxysilane [99,100]	$CH_2{=}CHSi(OC_2H_5)_3$
Phenyidiethoxysilane [99,100]	$C_6H_5Si(OC_2H_5)_3$
Dimethyldiethoxysilane [99,100]	$(CH_3)_2Si(OC_2H_5)_2$
Diphenyldiethoxysilane [99,100]	$(C_6H_5)_2Si(OC_2H_5)_2$
Tetrapropoxysilane [99,100]	$Si(OC_3H_7)_4$
Tetrabutoxysilane [101]	$Si(OC_4H_9)_4$
Diacetoxyditertiary-Butoxysilane (DADBS) [103,104]	$(C_2H_5O)_2Si(OC_3H_7)_2$
Diethylsilane (DES) [105]	$SiH_2(C_2H_5)_2$

Table 2.6 Deposited Techniques of CVD Silicon Dioxide

Technique	Reactants	Remarks
LPCVD [83,84]	TEOS; TBOS, N_2O	Deposition temp.690 -810°C, at 0.2-1.0 Torr
LPCVD [104]	$SiH_2(C_2H_5)_2$,O_2	Deposition temp. 475°C,at 0.5 Torr
LPCVD [86,88]	TEOS, N_2O	Deposition temp. 650 - 800°C
LPCVD [84]	SiH_2Cl_2, N_2O	Deposition temp.800-900°C,at 0.5 Torr
APCVD [85]	SiH_4, O_2	Deposition temp. 450°C, at atmospheric pressure
APCVD [89]	TEOS, Ozone	Deposition temp.400°C, at atmospheric pressure
PECVD [93,96]	SiH_2Cl_2, TEOS, O_2/N_2O	Deposition temp. 350° ~ 400°C , $O_2/N_2O:SiH_2Cl_2$ = 15:1 to 30:1

Table 2.7 Properties of silicon dioxide deposited by different methods

Film Type	Thermal	PECVD	APCVD	LPCVD $SiCl_2H_2 + N_2O$	LPCVD DES
Deposition Temp(°C)	800-1200	200	450	900	As low as 350
Step Coverage	Conformal	poor	poor	conformal	conformal
Stress (x 10^9 dynes/cm^2)	3C	3C-3T	3T	3T	<1C
Dielectric Strength (10^6 V/cm)	3-6	8	10	10	
Density (g/cm^3)	2.27	2.1		2.07-2.27	2.25
Ref. index	1.46	1.47		1.46	1.46
Etch Rate (Å/min)	130* 50-80**	1635* 400**	60**	30**	850*

* P-etch (49% HF: 70% HNO_3 : H_2O = 3 : 2 : 60)

** HF: H_2O = 100:1

Diethlysilane (DES), the precursor used in this study, has a vapor pressure as high as 207 Torr at room temperature (20°C). It can be processed into the reactor without the need of a carrier gas. Heating of the liquid source and the delivery line is not necessary either. Also, attractive is the fact that DES is environmentally benign, satisfying and safety or environmental concerns. The main properties of DES are listed in table 2.8.

Table 2.8 Properties of DES

Chemical Name	diethylsilane (DES)
Chemical formula	$SiH_2(C_2H_5)_2$
General Name	Organohydrosilane
Molecular weight	88.2
Appearance	Clear colorless liquid. No odor
Solubility in water	Insoluble
Autoignition Temperature	218°C
Normal Boiling point	56°C
Freezing point	-134°C
Vapor density (air=1)	3
Density	0.681 g/cm^3@20°C
Vapor pressure	207 torr @20°C

2.2.2 Properties of SiO_2

In general, the deposited oxide films must exhibit uniform thickness and composition, low particulate and chemical contamination, good adhesion to the substrate, low stress to prevent cracking, good integrity for high dielectric breakdown, conformal step coverage for multilayer systems, low pinhole density, and high throughput for manufacturing. Some of the properties obtained for thermal oxide are shown in table 2.9 [106].

CVD silicon dioxide is an amorphous structure of SiO_4 tetrahedra with an empirical formula SiO_2. Depending on deposition conditions, CVD silicon dioxide may have a lower density and slightly different stoichiometry from thermal silicon dioxide, causing changes in mechanical and electrical film properties (such as index of refraction, etch rate, stress, dielectric constant and high electric field breakdown strength). Deposition at higher temperatures, or use of a separate high temperature post-deposition anneal step can make the CVD films approach those of thermal oxide.

Table 2.9 Properties of Thermal Silicon Dioxide

Boiling Point (°C)	~2950
Melting Point (°C)	~1700
Molecular Weight	60.08
Refractive Index	1.46
Specific Heat (J/g°C)	1.0
Stress in film on Si (dyne/cm^3)	2-4 x 10^9, compressive
Thermal Conductivity (W/cm°C)	0.014
Dc Resistivity (Ω-cm), 25°C	10^{14}-10^{16}
Density (gm/cm^3)	2.27
Dielectric constant	3.8-3.9
Dielectric Strength (V/cm)	5-10x10^6
Energy Gap (eV)	~8
Etch rate in buffered HF (Å/min)	1000
Linear Expansion Coefficient (cm/cm°C)	5x10^{-7}

Deviation of the CVD silicon dioxide film's properties from that of the thermal SiO_2 value is often used as an indicator of film quality. For example, the refractive index of CVD SiO_2 greater than 1.46 indicates a silicon rich film, while smaller values indicate a low density, porous film.

Levy et al. [105] used DES as the precursor to deposit SiO_2 by LPCVD. In this work, they studied the film properties obtained by varying temperature, pressure, O_2 flow rate, O_2/DES ratio. It was found that that the deposition rate as a function of temperature showed an Arrhenius behavior and decreased monotonically from 0.75 Torr to 0.35 Torr, where the deposition ceased abruptly. They evaluated the activation energy to be 10 Kcal/mol by studying the variation of deposition rate with temperature (in the range of 350-450°C). The growth rate was observed to increase with higher pressure and to vary as a function of the square root of the DES flow rate and O_2/DES ratio. The films were determined to be essentially carbon free and slightly oxygen rich. The refractive index of the films was in the narrow range 1.453-1.456, independent of deposition conditions. The film stress was measured as a function of oxide film thickness for process conditions of 400°C, 0.5 Torr, 50 sccm DES and 100 sccm of O_2. The stress was found to be compressive and decreased with thickness. The density of the films was found to be 2.25g/cm^3.

2.3 Synthesis of Phosphosilicate Glass

As a core material, PSG (phosphosilicate glass) has only a slightly different refractive index from that of silica. It is easy to form single mode waveguide. PSG can be synthesized by using the same deposition processes of silica.

2.3.1 LPCVD of Phosphosilicate Glass

The addition of small amounts of phosphorus to silica films has several functions including changing the refractive index, lowering the melting point of silica glass and hence reducing the film reflow temperature, reduction of silicon film stress, modification of the thermal expansion coefficient, and densification of the silica-based film. Therefore, the properties of phosphorus doped silicon dioxide are considerably different from those of undoped CVD SiO_2. For example APCVD PSG shows reduced stress and somewhat improved step coverage as compared to the undoped oxide.

Low pressure chemical vapor deposition (LPCVD) of PSG films has generally been deposited using oxidation of silane and phosphorus by nitrous oxide, which is assumed to be

$$SiH_4 + 4N_2O \Longrightarrow SiO_2 + 2H_2O + 4N_2$$

$$2PH_3 + 8N_2O \Longrightarrow P_2O_5 + 3H_2O + 8N_2$$

For the SiH_4 and O_2 reaction, the overall reaction can be summarized as

$$SiH_4 + O_2 \Longrightarrow SiO_2 + 2H_2$$

$$4PH_3 + 5O_2 \Longrightarrow 2P_2O_5 + 6H_2$$

Since PSG consists of two compounds, P_2O_5 and SiO_2, it is a binary glass. It is relatively easy to incorporate the P_2O_5 into the PSG, as the SiH_4:PH_3 ratio in the gas flow controls the SiO_2:P_2O_5 ratio in the deposited film. PSG becomes increasingly hygroscopic at high P concentrations. Thus the P content should be maintained at 6-8 wt % to minimize phosphoric acid formation [107].

Due to the advantages of LPCVD, silicon dioxide films have been deposited at reduced pressure and low temperatures. Unfortunately, the advantages of LPCVD do not exist when phosphorus-doped silicon dioxide is deposited at reduced pressure using the reaction of silane, phosphine, and oxygen at 350^0 -400^0C. The step coverage of films deposited at these low temperatures is non-conformal. Heat-treatment at ~1100^0C is usually used to flow the glass in order to get uniform step coverage. This high temperature treatment is not acceptable for very short channel devices where shallow junctions are required. Hence, there have been some reports of the deposition of PSG films in the mid-temperature range (600^0-800^0C) at reduced pressure, using the decomposition of organosilicon and organophosphorus compound to get improved step coverage.

2.3.2 PSG Structure

PSG is a binary glass that consists of two compounds — P_2O_5 and SiO_2. It is expected that physical characteristics of the phosphorus doped silica glass be related to the chemical structure and composition of the phosphorus species in the silica network. However, since electron diffraction of the PSG film gives holo pattern in every case, sufficient knowledge in the film structure has not yet been obtained. Tien et al [108] has reported a phase diagram of SiO_2-P_2O_5 system, by saturated equilibration and quenching technique on bulk materials. Eldridge et al.[109] dealt with PSG film with gaseous P_2O_5 over a temperature range from 800^0 to 1200^0C. According to their results, small, water-soluble crystallites were formed at 870^0C or less on the surface of a film, and from the SiO_2-P_2O_5 phase diagram of Tien et al., these small crystallites were assumed to be $2SiO_2 \cdot P_2O_5$ or

$SiO_2 \cdot P_2O_5$. When the PSG films were formed at a relatively low temperature, phosphorus in the film was considered to be in such a state that small particles of phosphorus oxide P_2O_5, rather than a compound such as $2SiO_2 \cdot P_2O_5$ or $SiO_2 \cdot P_2O_5$, were dispersed in the SiO_2 matrix [110]. At low phosphorus oxide concentration in the PSG film, the SiO_2 matrix which is water-insoluble protects the phosphorus oxide from being attacked by water. However, as the phosphorus oxide concentration increases to certain critical concentration, the volume fraction of phosphorus oxide to the SiO_2 matrix increases, and the SiO_2 matrix is no longer effective in protecting the phosphorus oxide from a moisture attack. The SiO_2 matrix has a larger angular distribution width of Si-O-Si bond when it is formed at low temperature [111]. Also, it is highly porous [112]. This probably allows water to penetrate into the film with ease causing phosphorus oxide to dissolve. Heat-treatment densifies the SiO_2 matrix, which in turn makes it hard for water vapor to diffuse and attack the phosphorus oxide. It is likely that heat-treatment leads to reaction of the phosphorus oxide with the SiO_2 matrix, and results in formation of water-insoluble compound such as $(SiO_2)_x(P_2O_5)_y$.

2.3.3 Phosphorus Content and Measurement

Phosphorus oxide concentration is an important parameter of the PSG film. It is known empirically that, as the phosphorus oxide concentration increases, the film will absorb water more easily. The film properties, e.g., reflow temperature and thermal expansion, are controlled largely by fixing the phosphorus content of the films [113]. The phosphorus content, in the form of P_2O_5, in annealed PSG films, is typically held within a 2 to 8 wt% range. At 8 wt% P and above, the films can become excessively hygroscopic, produce corrosive compounds, and form microcrystallites, while at 2 wt% P and below the P doping does not modify the film properties enough to be useful. So it is important to be able to control and determine this composition. Composition control is frequently achieved by controlling temperature and reactant gas composition during chemical vapor deposition of the PSG film.

Phosphorus content is an important factor in the fabrication of the waveguide used for the integrated device. A balance has to be considered so the P content should be high enough for the required refractive index, but it should not be very high else the film will become hygroscopic. Another important aspect to be kept in mind is that excess P (above 7.5%) would make the film absorb moisture, which is undesirable. The properties of PSG that make it useful in a given application may depend on its composition. Hence, it must be possible to determine and control this composition [114]. Work had been done by Murarka and Adams [115] on measuring the P concentrations in PSG films. They compared the accuracy of measuring P concentration by each different technique.

2.4 Other Silicon Dioxide Technology

2.4.1 Sputtering of SiO_2

When an ion approaches the surface of a solid usually called the Target, one or all of the following phenomena [116] may occur: First, the ion may be reflected, probably being neutralized in the process. This reflection is known as Ion Scattering. Second, the impact of the ion may cause the target to eject an electron usually referred to as Secondary Electron. Third, the ion may become buried in the target. This is Ion Implantation. The ion impact may also be responsible for some structure rearrangements in the target material, or may set up a series of collisions between atoms of the target, possibly leading to the ejection of one of these atoms. This ejection process is known as Sputtering. Any suitably energetic atomic particle impinging against a surface can cause sputtering. Fig. 2.9 simply shows a sputtering system.

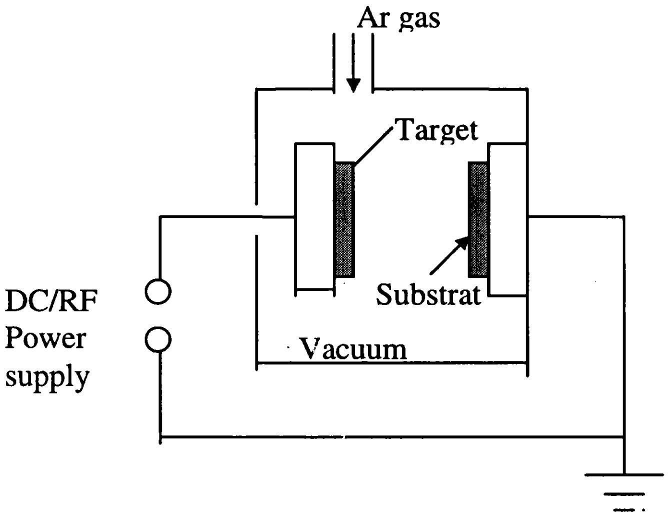

Fig. 2.9 Scheme of a sputtering system

Physical sputtering is a non-thermal vaporization process. The surface atoms are physically ejected by momentum transferring from the energetic bombardment particles that are usually the accelerated ions from plasma. Sputter deposition may be performed at low gas pressure (<5 mTorr) where the sputtered particles do not suffer gas phase collisions or in a higher gas pressure (5-30 mTorr) where energetic particles from sputtering target are thermallized by gas phase collisions before they reach the substrate surface [117]. The applications of sputtering system for silicon dioxide films had been discussed in ref. [118-119].

2.4.2 Thermal Oxidation

The formation of silicon oxide on a silicon surface is termed as oxidation. The ability to form this oxide (SiO_2), which is stable and tenacious, provides the foundation for planar processing of silicon integrated circuits. Although there are several ways to produce SiO_2 directly on the Si wafer, it is most often accomplished by thermal oxidation, in which the silicon is exposed to an oxidizing ambient (O_2, H_2O) at elevated temperatures. Thermal oxidation is capable of producing SiO_2 films with controlled thickness and Si/SiO_2 interface properties.

Thermally grown SiO_2 of VLSI applications is in the thickness ranging from 60 Å to 10,000 Å. The functions of these films include: (1) mask against ion implantation and diffusion, (2) passivation of the silicon surface, (3) isolation of individual devices (e.g. local oxidation of silicon, or LOCOS), (4) gate oxide and capacitor dielectric in MOS devices, and (5) tunneling oxide in electrically alterable ROMs. Table 2.10 [120] lists the range of oxide thickness commonly used for these applications.

Thermally grown SiO_2 film has an amorphous structure with random network of polyhedra. The density of thermally grown fused silica (2.15-2.25 g/cm^3) is less than that of crystalline quartz (2.65 g/cm^3). The lower density implies a more open structure. The specification of SiO_2 film is listed in table 2.9. Other advanced thermal processes had been discussed in ref. [121-123].

Table 2.10 Range of thermal SiO_2 thickness used in VLSI

SiO_2 Thickness (Å)	Application
60-100	Tunneling Oxides
150-500	Gate Oxides, Capacitor Dielectrics
200-500	LOCOS Pad Oxide
2000-5000	Masking Oxides, Surface Passivation Oxides
3000-10000	Field Oxides

2.4.3 Microwave Plasma Assisted CVD (MPACVD)

The fabrication process of MPACVD is cost efficient, and compatible with that used for Si-based microelectronics. It is used to produce a superior quality, low birefringence, low loss planar waveguide for integrated optical devices on either silica or silicon substrate. By using this technique, a Ge-doped silica layer was deposited on the substrate where a higher growth rate (0.4~0.5μm/min) compared to the typical chemical vapor deposition was observed [124]. Fig. 2.10 is the diagram of MPACVD.

The dielectric thin films deposited by MPACVD have excellent optical qualities including lower scatter and less strain than the most conventional coatings. An important feature of this process is that both the deposition rate and the composition of the film can be adjusted automatically during the deposition process. This degree of control allows the deposition of both graded and even more complicated refractive index profiles. The technique therefore allows the successful realization of highly sophisticated coating designs (e.g. Fourier). The process has been used to fabricate a range of dielectric designs, including narrow band high reflectivity coatings with minimal sidebands, using silicon oxynitride on fused silica substrates [125]. The disadvantage of MPACVD is that the film has higher compressive stress, since higher power levels increase plasma density, thus resulting in greater ion bombardment density.

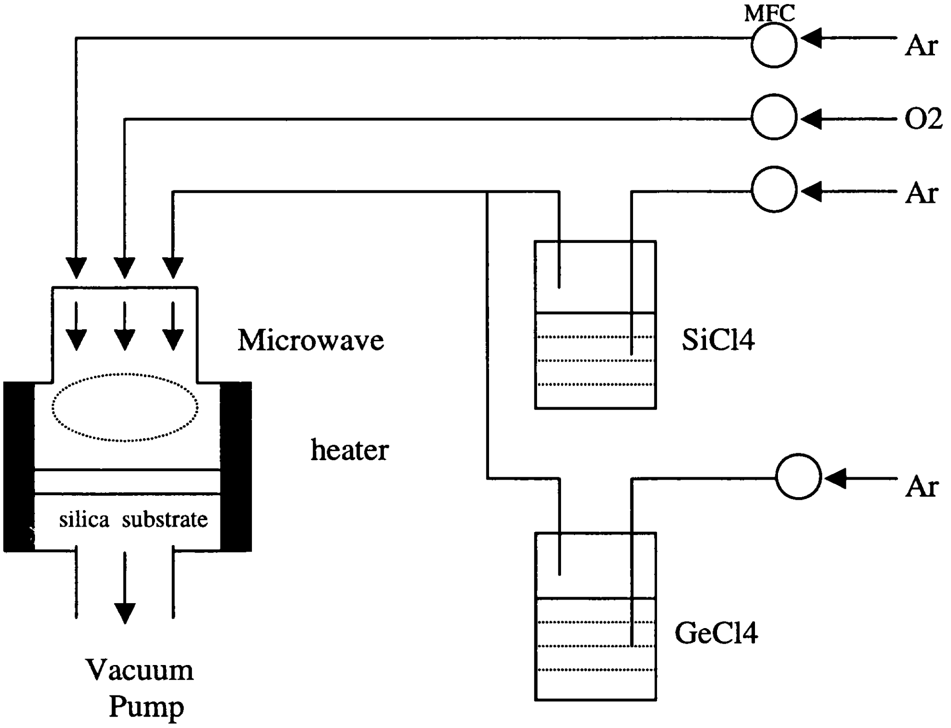

Fig. 2.10 A schematic drawing of the MPACVD system

2.2.4 Flame Hydrolysis Deposition

The vapor phase deposition techniques of fiber can be divided into two broad categories: flame hydrolysis and chemical vapor deposition. The individual techniques of flame hydrolysis are considered [126] as vapor axial deposition (VAD) and outside vapor phase oxidation process (OVPO).

OVPO process (Fig. 2.11) was used to produce the first fiber with losses of less than 20dB/Km. In this technique, the required glass composition is deposited laterally from a "soot" generated by hydrolyzing the halide vapors in an oxygen-hydrogen flame. The purity of the glass fiber depends on the purity of the feeding materials and also upon the amount of OH impurity. Other problems stem from the use of mandrel which can produce some difficulties in the forming of the fiber perform.

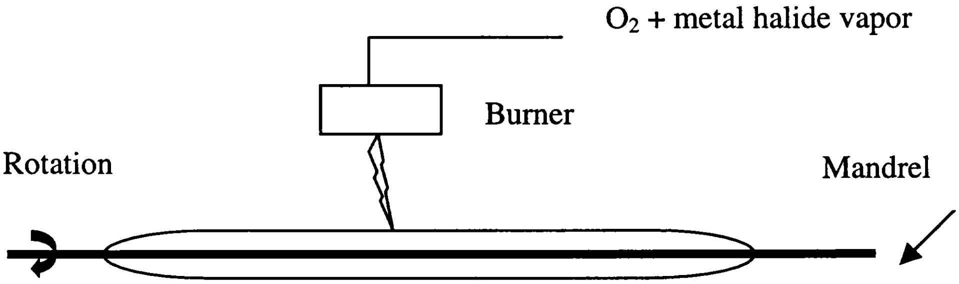

Fig. 2.11 Schematic diagram of the OVPO process

The VAD technique uses an end-on deposition onto a rotating fused silica target. The vaporized constituents are injected from burners and react to form silica soot by flame hydrolysis. Fibers produced by the VAD process still suffer from some OH impurity content due to the flame hydrolysis and hence very low loss fibers have not been achieved using this method.

Flame hydrolysis deposition process allows buried optical waveguide structures [127] to be produced, which are isolated from the surface using a glass overlayer, or cladding. FHD still is an important process for planar lightwave circuits [128]. The fabrication of the birefringence free planar optical waveguides has been reported [129].

2.4.5 Sol-Gel Deposition

Sol-gel deposition process is a method of making glass that does not involve a melting process. The starting materials used in the preparation of the "sol" are usually inorganic metal salts or metal organic compounds such as metal alkoxides. In a typical sol-gel process, the precursor is subjected to a series of hydrolysis and polymeration reactions to form a colloidal suspension, or a "sol". Further processing of the "sol" enables one to make ceramic materials in different forms. Thin films can be produced on a piece of substrate by spin-coating or dip-coating. When the "sol" is cast into a mold, a wet "gel" will form. With further drying and heat-treatment, the "gel" is converted into dense ceramic or glass articles. If the liquid in a wet "gel" is removed under a supercritical condition, a highly porous and extremely low density material called "aerogel" is obtained. As the viscosity of a "sol" is adjusted into a proper viscosity range, ceramic fibers can be drawn from the "sol". Ultra-fine and uniform ceramic powders are formed by precipitation, spray pyrolysis, or emulsion techniques. The quality and uniformity of the film fabricated by sol-gel deposition depends upon the coat-spin process. Sol-Gel processes have already been commercialized for a high-volume production in coatings, fibers, and semiconductor doping. Passive, active, and nonlinear optical materials for optical devices like sensor [130] and scanners [131] are accessible by sol-gel methods.

CHAPTER 3

PRINCIPLE AND EXPERIMENT SET UP

3.1 Mach-Zehnder Interferometer Under Study

Previous studies have suggested optical techniques for on-site/real-time monitoring of organic contaminants. These sensing methods rely on the use of optical fibers or planar waveguide sensing devices. In this program, we used the optical principles of the interferometry to produce a novel integrated optical sensor capable of monitoring and determining in-situ the concentration of numerous analyte species. The sensor could operate in either gaseous or aqueous environment. The output signal from this sensor can be used in a closed loop control manner to reduce environmentally hazardous emissions associated with manufacturing processes through fast response process control. Process control sensor systems are needed for both military and commercial application. This novel device is based on well established physical principles. It is non-intrusive for deployment at manufacturing sites in order to obtain accurate, rapid, and cost effective data. The overall instrument is envisioned to be compact, portable, rugged, and suitable for real-time monitoring of toxic environment. It offers numerous advantages over conventional analytical techniques such as gas chromatography and mass spectrometry including small physical size, geometric flexibility, environmental versatility, real-time and in-situ analysis, instrumental reliability, analyte specificity, insensitivity to electromagnetic interference, and low power requirements.

The fabrication of this sensor is based on the technology with standard large scale integrated silicon processing where photolithography and reactive ion etching steps can be used to mass produce copies of the pattern at low cost. Through electronic integration, components can be added on the same device for signal processing and sensor resetting purposes. A resistor, for example, can easily be designed on the chip to heat the sensing element for desorbing the analyte and regenerating the sensor. This surface desorption process which does not involve diffusion or a chemical reaction is very fast and expected to take less than one second. Through photonic integration, light sources and detectors can be placed on such a sensor eliminating the use of coupling of fibers. In addition to offering the advantage of miniaturization, this technology offers high throughout (hundreds of sensors per silicon wafer) which translates into low cost (less than a couple of dollars) per device.

3.1.1 Principle of Mach-Zehnder Interferometer

The designed sensor consists of a Mach-Zehnder integrated interferometer constructed from a single mode waveguide. The waveguide consists of a Y-shaped splitter that divides an incident guided optical mode into each arm of the interferometer and interferes the resulting guided optical modes at an emerging Y-shaped splitter. One of the arms of the interferometer is covered by a protective oxide layer to give it a constant effective refractive index, while the other is exposed to the environment through a "window" in the protective layer to allow the effective index of the guide to vary with external conditions. The two resulting modes are interfered which results in an intensity change of the output signal that depends on the differences in the effective indices of each guide

External organic pollutants were detected through their coupling with the evanescent component of the exposed guided optical mode. The strong variation of the sensor's output intensity to index changes was used to construct a unique profile of the strong index changes for a polluting substance or mixture of substances. The results of the profile were used for the detection of a substance if either a selective film is placed in the sensor window to select out certain polluting substances from the surrounding environment or a suitable method of reference can be used to distinguish the various components of the mixture. The evanescent absorption of light by organic pollutants in the near-IR was also used to determine their concentration. The change in the refractive index of water or air caused by the presence of pollutant molecules could be readily detected by the exposed sampling arm. Therefore, a phase difference, $\Delta\Phi$, developed between the sampling and reference arm. When lights from the two interferometric arms recombine, interference occurs and the light intensity exiting the interferometer, I_x, ratio to input light, I_o, is given by:

$$I_x / I_o = 1/2\ (1+\cos \Delta\Phi) \qquad (3.1)$$

Where

$$\Delta\Phi = 2\times\pi\times L\ (n_1 - n_2)/\lambda_0 \qquad (3.2)$$

with L being the common length for both arms of the interferometer, n_i the effective index of arm i. λ_0 is the input light wavelength. Therefore, the phase difference is directly proportional to the effective index difference ($\Delta n_{eff}=n_2-n_1$)

between the waveguide arms. Since the pollutant level affects Δn_{eff} (gas and solution absorption will change the refractive index [132] and surface roughness [133], we use effective index instead of ideal index), then the output intensity changes with the concentration of pollutants present in the sample. For a typical arm length L =0.6 cm, and a λ_0 = 633 nm, $\Delta\Phi = \pi$ (i.e., 1 fringe shift or 100% signal modulation) for a $\Delta n_{eff} = 6\times10^{-5}$. Therefore, extremely small changes in the effective index caused by the presence of low concentrations of pollutants can be measured using this interferometeric approach. Theoretical calculations [134] have indicated that the concentration of the pollutants in water can be measured down to 20 ppm for sensor with uncoated sampling arms and sub-ppb levels (1-10 ppb) for presence of a polymer coating (i.e., polyalkylsiloxane type) on the waveguide sampling arm since the polymer can provide sensor specificity and enhance the concentration measurement. Furthermore, the polymer coating is naturally hydrophobic and precludes water absorption that might interfere with the near IR absorption spectra when monitoring aqueous mixtures.

The principle of the Mach-Zehnder on study is schematic as following:

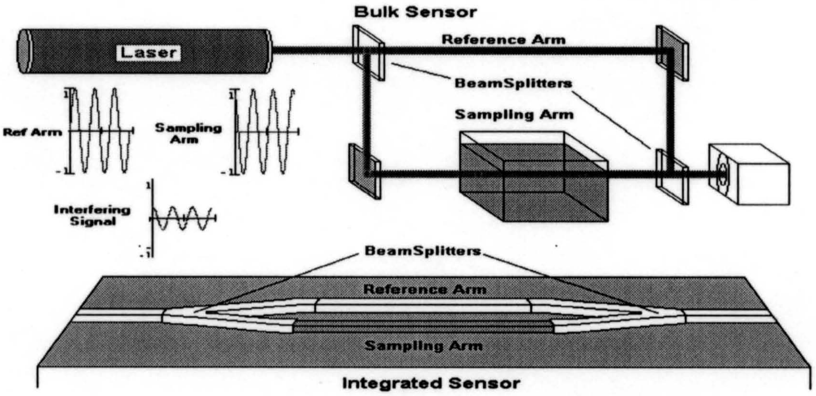

Fig. 3.1 Schematic principle of Mach-Zehnder interferometer on study

At any single wavelength, this Mach-Zehnder cannot distinguish one pollutant from another since it only measures an average regractive index of all pollutants at that wavelength. However, by using a broadband light source, rather than a single wavelength laser, the interferometer can measure the refractive index difference over a wide spectrum. For any material which has a strong absorption over some narrow wavelength range, there is an accompanying rapid change in the index of refraction. For a device with a short interaction length (~1 cm) such as the Mach-Zehnder interferometer, changes in the sensor output due to wavelength dependent direct absorption in the Mach-Zehnder waveguide are small. But the phase changes are large because of the absorbance of the evanescent wave that is due to the penetration of a portion of light into the surrounding medium of the interferometer sampling arm and the interaction of that portion of light with vibrationally active analytes. The wavelength range is chosen to overlap the near infrared regime (1000-2000nm) where many common organic species have characteristic absorption features that provide quantitative chemical information. By measuring the transmission of broadbanded light through the interferometer and matching the recorded spectrum to know standards, the composition and concentration of pollutants in air or water can be readily determined.

In evanescent wave absorption spectroscopy, where the waveguide is essentially a fiber optic, there exists a range of incident angles. Upon total internal reflection of light in the waveguide, a portion of light enters the surrounding medium. This is known as the evanescent wave. Vibrationally active analytes present in the evanescent field above the sampling arm of the sensor will absorb wavelength dependent light according to following relationship [135]:

$$-\log (I_1/I_2) = \alpha_e Lc + 2\log (NA_2/NA_1) \qquad (3.3)$$

Where I_1 is the transmitted light intensity after sensor exposure to analyte, I_2 is the reference intensity with no analyte present, c is a molar concentration, and NA_1 and NA_2 are the sensor numerical apertures with and without analyte present, respectively. The numerical aperture NA determines the amount of light collected by the fiber from an infinite source. It is defined as:

$$NA = n_{ext} \sin\theta_a = [(n_2+n_1)(n_2-n_1)]^{1/2}$$

Where n_{ext} is the refractive index of the external medium and θ_a is acceptance angle of the fiber, n_2 and n_1 represent the core and cladding refractive index. The effective molar absorptivity, α_e, is defined as

$$\alpha_e = \varepsilon \times k/V$$

Where ε is the molar absorptivity of the infrared active species, k is a proportionality constant, determined by Gloge [136] be 1.89 for equilibrium mode distribution in a fiber. V is normalized frequency that will be discussed later.

3.1.2 Design of Mach-Zehnder Interferometer

The Mach-Zehnder interferometeric structures that constitute these sensors have been designed as the TE single mode waveguide. The derivation was limited to the guided modes that according to Fig..3.2 have propagation constants β and $k_0 n_3 < \beta < k_0 n_2$, where, for symmetric slab waveguide, $n_3 = n_1$

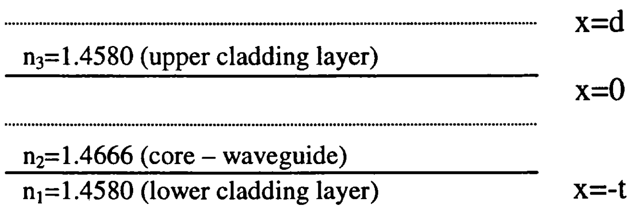

Fig. 3.2. A symmetric slab waveguide

The field components of the TE modes are determined from [137]:

$$\xi y = \begin{cases} C\exp(-qx) & 0 \le x < \infty \\ C(\cos hx - q/h \sin hx) & -t \le x \le 0 \\ C(\cos ht + q/h \sin ht)\exp[p(x+t)] & -\infty < x \le -t \end{cases}$$

$$h = \sqrt{k_0^2 n_2^2 - \beta^2}$$

$$p = q = \sqrt{\beta^2 - k_0^2 n_1^2}$$

t – width of waveguide

k – wavenumber, $2\pi / \lambda$

The acceptable solutions should be continuous at both x = 0 and x = -t;

$$\tan ht = 2ph/(h^2 - p^2)$$

$$\cos ht = (h^2 - p^2)/(h^2 + p^2)$$

$$\text{Total power} = \frac{\beta}{2\omega\mu} \int_{-\infty}^{+\infty} (\xi y)^2 \, dx = 1$$

$$C = 2h\left[\frac{\omega\mu}{\beta\,(1 + 2/p)\,(h^2 + p^2)}\right]^{0.5}$$

Assuming m% of power leakage above upper cladding layer d, so:

$$\frac{\beta}{2\omega\mu} \int_{d}^{+\infty} (\xi y)^2 \, dx = m\%$$

$$d = 1/2p \ln \frac{h^2}{m\%(pt + 2)(h^2 + p^2)} \qquad (3.4)$$

Equation 3.4 is the theoretical thickness of upper cladding layer and beyond it the light leakage will equal to m %. Fig. 3.3 shows the schematic field distribution of the TE mode.

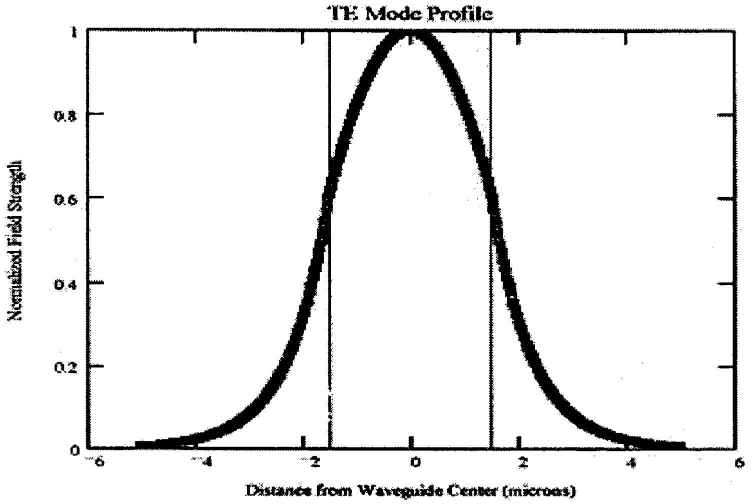

Fig. 3.3 Field distribution of the TE mode waveguide

In order to have a single mode planar waveguide, the width of the guide t must be determined for single mode operation. The following equations [126] give Normalized frequency describing the modes of waveguide, which can be expressed in terms of the numerical aperture NA.

$$V = 2\pi \times \alpha \times NA / \lambda \qquad (3.5)$$

V – normalized frequency

α– radius of fiber core, equal to t /2

NA – numericl frequency

λ – wavelength

Table 3.1 Relationship between V and fiber modes

Normalized frequency (V)	Fiber modes
$0 \leq V < 2.405$	Single mode
$2.405 < V \leq 3.83$	Multiple modes

The cut-off value of normalized frequency for single mode is 2.405, choose V=2.4 and get from (3.5)

$$\alpha = V\lambda/(2\pi^*\ NA)=2.4\lambda/(2\pi^*\ NA) \tag{3.6}$$

$$\lambda = \alpha^*2\pi^*\ NA/2.4 \tag{3.7}$$

$$t = 2\alpha$$

By using the data listed on Fig..3.2, the theoretical results were calculated and listed in table 3.2 and table 3.3. The cross section of the designed Mach-Zehnder interferometer is seen in Fig. 3.4.

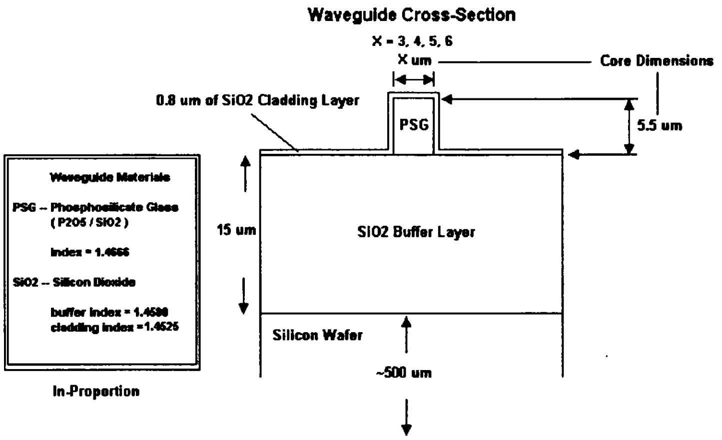

Fig. 3.4 Cross section of designed waveguide

Table 3.2 Theoretical thickness of upper cladding layer (T_{upper}) and core width of single mode waveguide at different wavelength and leakage ($n_1=n_3=1.4580$, $n_2=1.4666$)

Leakage out of upper cladding layer (%)	Wavelength λ (μm)	Fiber Mode	Width of waveguide (μm)	T upper cladding layer (μm)
1	0.628	1	3.03	0.99
	0.8	1	3.86	1.27
	1.5	1	7.23	2.38
2	0.628	1	3.03	0.69
	0.8	1	3.86	0.87
	1.5	1	7.23	1.64
3	0.628	1	3.03	0.50
	0.8	1	3.86	0.64
	1.5	1	7.23	1.20
4	0.628	1	3.03	0.38
	0.8	1	3.86	0.48
	1.5	1	7.23	0.90
5	0.628	1	3.03	0.28
	0.8	1	3.86	0.35
	1.5	1	7.23	0.66

Table 3.3 Theoretical thickness of upper cladding layer (T_{upper}) and wavelength of single mode waveguide at different core width and leakage (n_1=n_3=1.4580, n_2=1.4666)

Leakage out of upper cladding layer (%)	Width of waveguide (μm)	Fiber Mode	Wavelength λ (μm)	T upper cladding layer (μm)
1	3	1	0.62	0.99
	4	1	0.83	1.31
	5	1	1.03	1.64
	6	1	1.24	1.97
2	3	1	0.62	0.50
	4	1	0.83	0.90
	5	1	1.03	1.13
	6	1	1.24	1.36
3	3	1	0.62	0.50
	4	1	0.83	0.67
	5	1	1.03	0.83
	6	1	1.24	1.00
4	3	1	0.62	0.37
	4	1	0.83	0.50
	5	1	1.03	0.62
	6	1	1.24	0.74
5	3	1	0.62	0.27
	4	1	0.83	0.36
	5	1	1.03	0.46
	6	1	1.24	0.54

3.1.3. Mask Design

The fabrication of the sensor involve two lithographic masks, one for patterning the waveguides, and the other for opening windows through the top cladding layer. Two masks were designed with Mentor graphics IC Station on a Sparc 20 workstation network. The UV exposure tool with a resolution limit of 2 μm was used with positive photoresist spun on the wafer.

In order to test the sensor under a variety of waveguide dimensions for optimal performance, several different types of sensors were created with varying lengths and widths. The sensor as illustrated in Fig..3.5 was repeated with varying lengths and widths twenty times in four groups of five. This set composed one "die" of sensors on the wafer. One of the four groups, which is the basic building block of the mask, is shown in Fig.. 3.6.

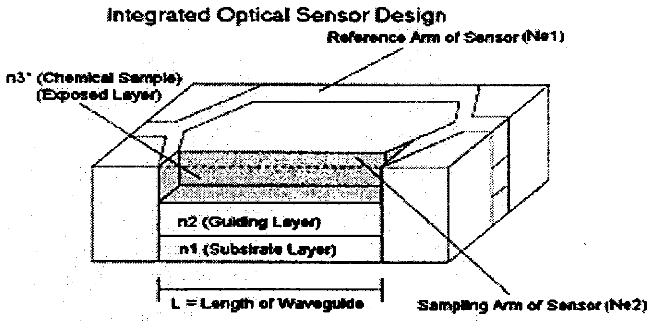

Fig. 3.5 Scheme of the integrated optical sensor

The first mask was used to pattern the actual sensor waveguide structure. The field of the mask was selected to be clear except for the dark regions of the waveguide patterns. For each basic group of 5 waveguides, the sensor's test path-lengths were set at 2, 4, 6, 8, and 10 mm in length. Each group was designed with waveguide widths of 3, 4, 5, and 6 microns. (See Fig.. 3.7). The widths given for each group of waveguides was meant for single mode operation in the near-IR. To ensure that each arm of the interferometer does not couple with each other, they were designed to be separated by 50 microns.

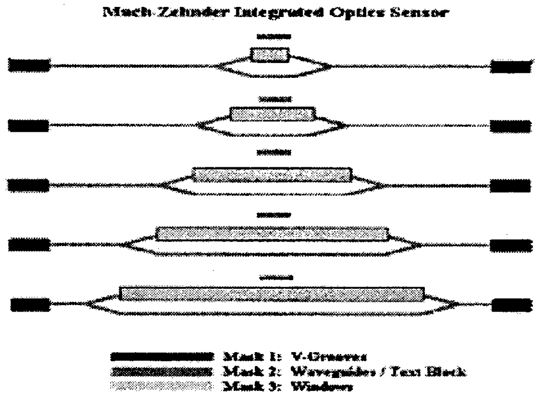

Fig. 3.6 Layout of masks for Mach-Zehnder interferometer

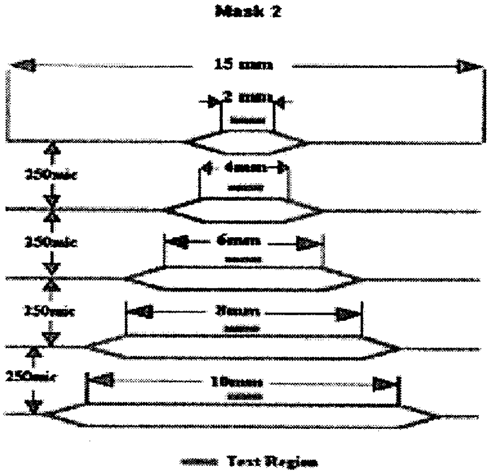

Fig. 3.7 Mask for waveguide patterns

In order to achieve a good coupling between the incoming light from the fiber optic cable and the two arms of the sensor, the Y-coupler used must have a low loss. This was achieved with an angle of separation between the sensor arms of less than 2 degrees, (See Fig.. 3.8) since a large bend in an integrated waveguide can lead to high radiation losses. The Y-coupler was also the most critical feature of the designed sensor since it had the smallest dimensions near the terminating end of the Y where the angled sections approach the 2 μm limit of NJIT's exposure tool (Fig.. 3.9). Therefore, the Y-coupler was examined extensively to ensure that it was being properly patterned in the oxide.

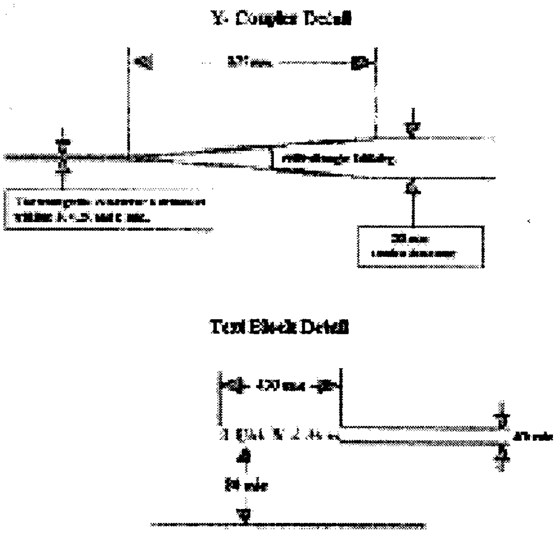

Fig. 3.8 Dimension of Y-splitter and text blocks

To identify the waveguides under the microscope, small blocks of text were used above each sensor device. The text blocks consist of the waveguide width followed by the pathlength for each device (ex. 3 μm X 4 mm). The dimensions of the text blocks are given in Fig.. 3.8.

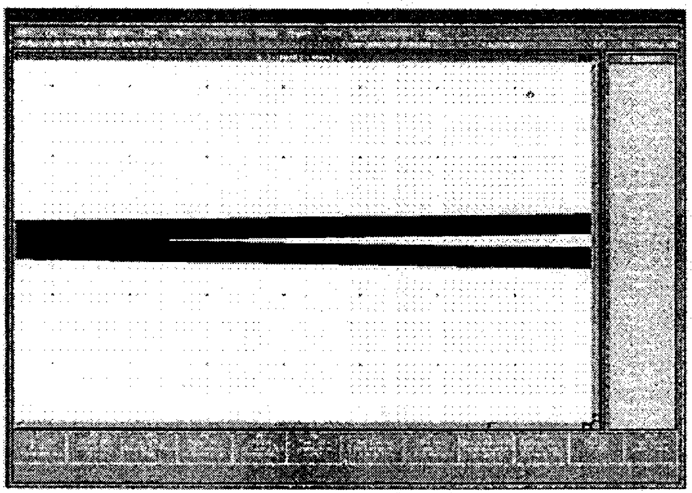

Fig. 3.9 Diagram of Y-splitter angled section

On the second mask, the entire field of the mask was selected to be dark except for the windows over the “sampling” arm of each sensor device. The windows were etched into the protective oxide layer over the entire length of the "sampling" arm of the sensor. The general layout of one of the waveguide groups for the sensor windows is illustrated in Fig.. 3.10. Each window was selected to be 70 microns in width to ensure that the entire "sampling" arm was exposed during processing.

Each sensor "die" was selected to be composed of the 4 groups of 5 waveguides as seen in Fig.. 3.11. The descending order of the groups is in the order of the waveguide widths. Each "die" was separated on the mask by the small cross alignment marks at each corner of the "die". The layout of the dies on the 5” wafer is shown in Fig. 3.12 where there are three rows. The numbers of dies in each row are, going from top to bottom: 2, 6 and 2 dies. This gives a total of 10 dies for testing, and 200 Mach-Zehnder sensors per wafer.

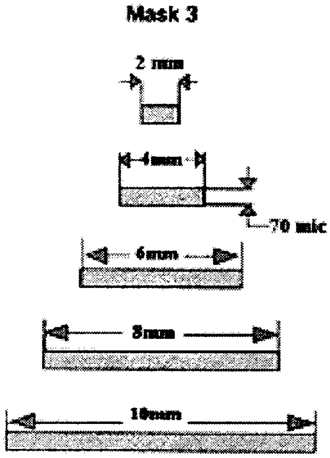

Fig. 3.10 Mask of the window for Mach-Zehnder interferometer

The two masks designed by Mentor Graphics were fabricated by Photronics, Inc. The window mask was produced using optical mask fabrication techniques, while the waveguide mask was produced using e-beam mask fabrication technology. The pattern on the masks was produced in anti-reflective chrome to eliminate optical back reflections and interference in the photoresist during exposure. Both masks were produced using the quartz substrate under the chrome. The waveguide mask was produced using e-beam fabrication because the smallest dimension of 3 microns or less on the mask cannot be produced reliably using optical fabrication. The mask was produced using the e-beam's highest writing resolution of 0.1 μm that is the smallest blocks of chrome that can be removed from the mask surface by the e-beam. This ensured the best reproduction of the sensor pattern.

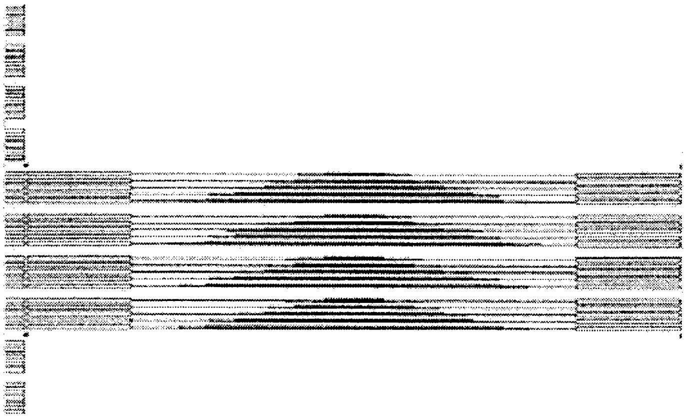

Fig. 3.11 The die of the Mach-Zehnder interferometer

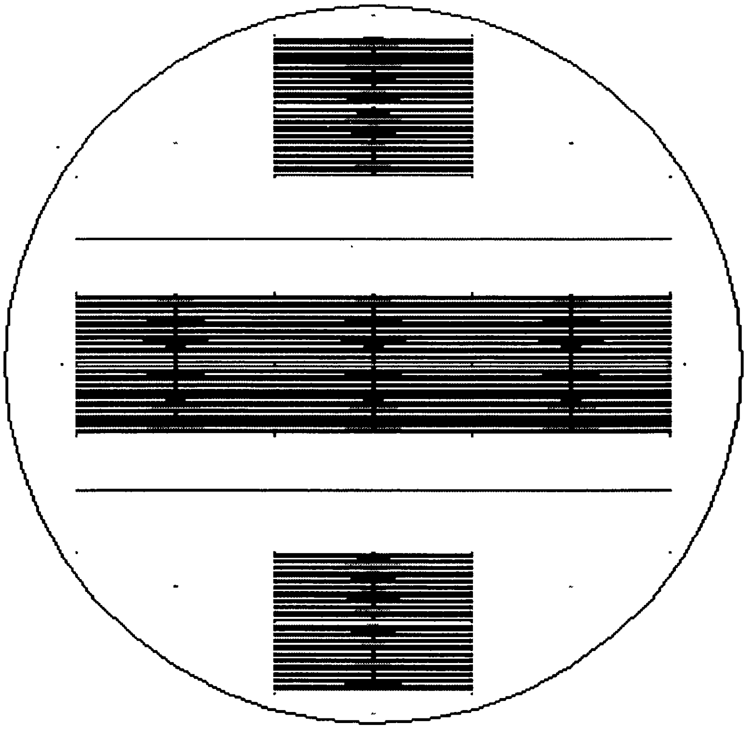

Fig. 3.12 The layout of the Mach-Zehnder interometer in 5" wafer

3.1.4 Optical Test of Mach-Zehnder Interferometer

Different concentrations of ethanol in water were used to experimentally verify a varying interferometric output for different pollutant concentrations. Due to possible changes in coupling efficiency of the light into the waveguide due to accidental motion of the fiber relative to the waveguide (e.g. fiber is bumped or moves due to air currents in the room), all data is normalized to the power through the waveguide with only air surrounding the sampling arm.

The protocol is to align all equipments, waveguide and laser sources. Next, a reference image is recorded corresponding to only air on sampling arm. Secondly, distilled water is introduced onto the sampling arm and captured by imaging the near field images from the waveguide as the light emerges. This protocol was repeated to ensure reproducible readings from the interferometer and ensure that the referencing of the interferometers readings to measurements made with air alone could correct for changing of input coupling to the device.

Reference images were recorded again before introducing chemical solutions of different concentration into the sampling arm and capture their corresponding images. Subsequently, the ratio of intensities of water and solutions with respect to reference air images were calculated according to the equations listed below:

$$\text{Ratio of intensity of water} = \frac{\text{Intensity\_of\_water}}{\text{Intensity\_of\_air}}$$

$$\text{Ratio of intensity of solution} = \frac{\text{Intensity\_of\_solution}}{\text{Intensity\_of\_air}}$$

The normalized intensity of solutions to water is calculated by:

$$\text{Ratio of intensity of solution} = \frac{\text{Ratio\_of\_Intensity\_of\_solution}}{\text{Ratio\_of\_Intensity\_of\_water}}$$

The output images corresponding to the solutions showed a change in intensity compared to that of water. The intensities changed with reference to water were then calculated from the output images by using pixel count using Mathcad V 7.0.

Table 3.4 shows typical data taken from different concentration of ethanol. The index change from water Δn is given by

$$\Delta n = \text{PPM} \times 10^{-6} (n_l - n_{H2O})$$

where PPM represents the concentration of liquid/chemical in parts per million, n_l for ethanol in this experiment is 1.363 and n_{H2O} for water is 1.333.

Theoretical intensity is obtained from

$$\frac{I_l}{I_{\max}} = \frac{1}{2}\left\{1 + \cos\left[\frac{2\pi L(n_b - n_l)\left(\Delta n_{eff}/\Delta n\right)}{\lambda_o}\right]\right\}$$

Where

n_b = Buffer layer index (1.458) over reference arm

n_l = Liquid index over sample arm

I_l = Interferometer output when liquid present over sample arm

I_{max} = Peak interferometer

The term $\Delta n_{eff}/\Delta n$ represents the specific mach-Zehnder index-conversion efficiency based on the particular interferometer design. It indicates the amount of waveguide effective index change that occurs per unit change in liquid index above the waveguide. In our study, $\Delta n_{eff}/\Delta n$ = 0.002 provided the best fit of theoretical data to the experimental data.

Table 3.4 Theoretical normalized output intensity vs concentration

Concentration (PPM)	**Index Change from water (Δn)**	**Normalized Intensity (Theoretical)**
500	0.000155	0.926604138
10000	0.00031	0.920293074
50000	0.00155	0.86160282
100000	0.0031	0.770244443
500000	0.0155	0.014629337
1000000	0.031	0.765954225

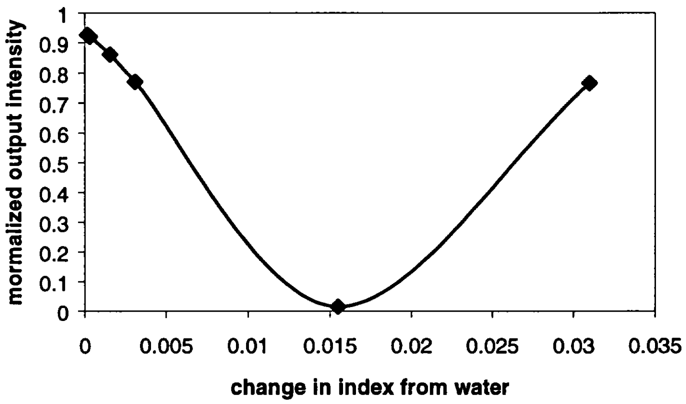

Fig. 3.13 Theoretical normalized output intensity vs. change in index from water

Fig. 3.13 and Fig. 3.14 show the plots of normalized output intensity versus index change from water and the index change versus the concentrations. Theoretical curve indicates phase change (fringe shift) in the interferometer output if interference occurs.

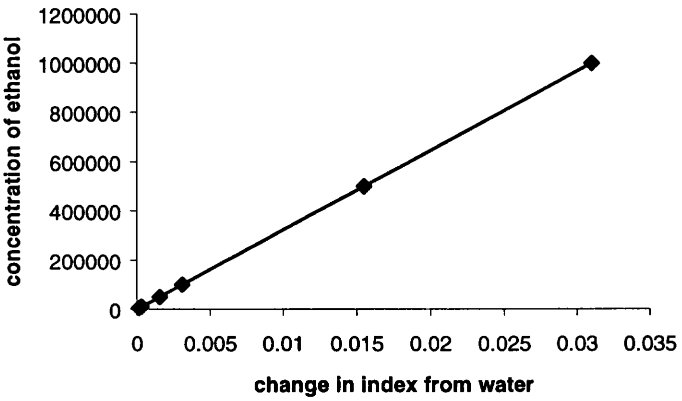

Fig. 3.14 The concentration of ethanol vs. change in index from water

Before the optical test, the wafer was cut up into dies. The test set-up included a Hitachi laser diode, a Thorlabs laser diode controller, a single mode optical fiber (5.5 µm core diameter), microscope, SBIG CCD camera, monitor and video capturing board. A scheme of the experimental setup is shown in Fig. 3.15. Light was coupled to the waveguide and the output intensity measured for different solution placed on the sampling arm. The laser beam was collimated and then focused to the fiber by an aspheric lens. The alignment between the fiber end and waveguide was optimized by using a microscope and Newport XYZ transitional stage. The light emerging from the waveguide was imaged and captured by a CCD camera. In order to test the sensitivity of the sensor to the pollutants, water as well as different ethanol solutions were prepared and dropped on the sample arm. A small refractive index change occurred when ethanol was mixed in water. The corresponding change in interferometric output image was captured by the CCD camera.

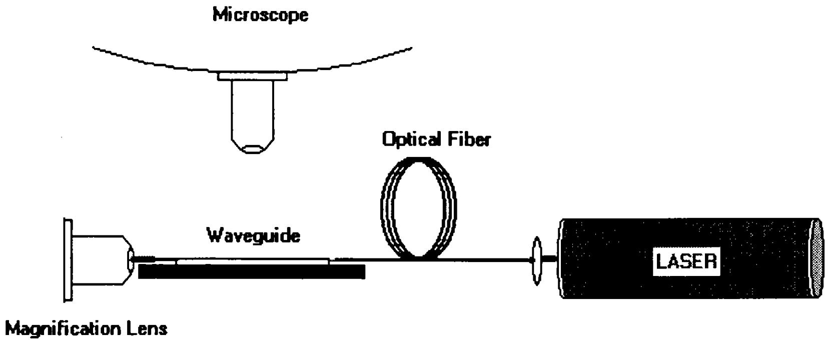

Fig. 3.15 Diagram of Mach-Zehnder interferometer experimental set-up

3.2 Fabrication of Mach-Zehnder Interferometer

Test waveguide was fabricated on 5 inches wafers with <100> orientation. A 15μm thick SiO_2 film was synthesized by low pressure chemical vapor deposition (LPCVD) to act as lower cladding material for the waveguide and prevent light from coupling with the underlying silicon. A 7 μm thick phosphrous-doped (~7.0 wt% P) LPCVD film will be synthesized to act as core material for the waveguide. This layer will be patterned using standard lithographic exposure and etch techniques and subjected to an around 1050 ^{0}C anneal to cause viscous flow and round off the edge. This round-off procedure is necessary to minimize coupling losses between fiber and waveguide. The refractive index of the doped glass will be 1.4666, thus, producing with the underlying SiO_2 (n_l=1.458) substrate a single mode waveguide device. Deposition of 1.2 μm thick undoped

SiO_2 buffer layer over the entire wafer and a subsequent lithographic step will result in selective removal of that layer over the sampling arm of the interferometer. This conFig.uration allows for exposure of the sampling arm (uncoated or coated) to various contaminants in the environment that cause a change in the effective index of that arm. The arm coated with the SiO_2 buffer layer will see a refractive index of n around 1.458. Three, four, five, and six microns-wide waveguides formed the two interferometer paths using a splitting angle of 2^0. The sampling and reference arms had a fixed separation of 50 μm and variable lengths (2, 4, 6, 8, and 10 mm). The processing sequence used in the fabrication of the sensor is shown in Fig. 3.16.

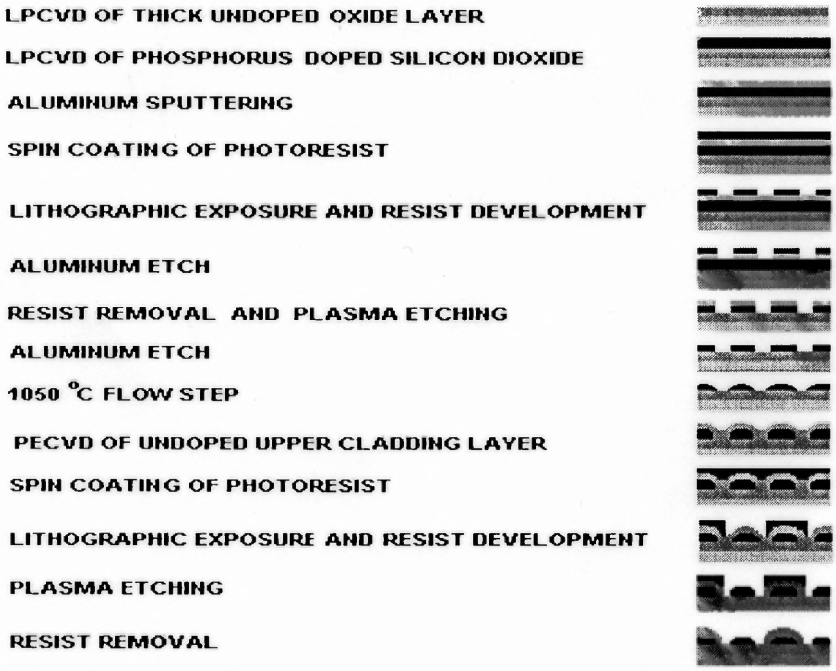

Fig. 3.16 Processing sequence used in fabrication of integrated optical sensor

3.2.1 Film Synthesis by LPCVD

As seen from the indicated sequence, the under cladding and core materials that constitute the waveguide fabrication process are silicon dioxide (SiO_2) and phosphosilicate glass (PSG), respectively. For reliable and reproducible device performance, these films must be uniform both in thickness and composition, be highly transparent to light, be stress-free, and have a low defect density. At the start of this program, the effort was focused on the development of thick SiO_2 and PSG films using diethylsilane (DES), a novel silicon precursor. The interrelationship governing deposition parameter, film composition, film properties, and waveguide performance were established for this novel precursor. DES has several advantages over silane including superior conformality, low particulate formation, low stress, and high crack resistance.

Phosphosilicate glass or P-glass is deposited for use as the core of the waveguide. The P-glass is deposited using the same precursor as for oxide. The source for the Phosphorus is Trimethylphosphite (TMP) which is a colorless liquid with a chemical formula $(CH_3O)_3OP$, a molecular weight of 140.08 and boiling point of 193 ^{0}C. TMP can improve the uniformity and step coverage of the film compared to PH_3, and film has high transparency, low stress and high growth rate. TMP does not have enough vapor pressure to flow into the chamber. It is thus injected into the chamber.

3.2.1.1 LPCVD Reactor The scheme for hot wall low pressure chemical vapor deposition reactor is shown in Fig. 3.17. The reactor consists of fused quartz tube inserted into a Lindbergh three zone furnace. The zone temperatures are controlled by manual settings. A maximum temperature of 1200°C can be reached using this furnace and a gradient of temperature can also be obtained inside the quartz tube. Heating is provided by Lindbergh silicon carbide heating elements. It is equipped with Plantinel II thermocouples which sense the temperature of the zone and the voltage developed which are used for automatic temperature control. The tube and the coils are surrounded with ceramic enclosure. The tube is sealed on both the ends by end caps and metallic rings. During the heating process, thermal expansion of the O-rings may cause leakage in the system. To avoid this problem, water cooling is arranged by cold water circulation. Apart from this, additional cooling is provided by the fans. A MKS baraton gauge with a range of 10 torr is used to monitor the pressure at the input end. The monitored pressure is displayed by MKS display unit. The input seal consists of three provisions for gas inlet, so that, if more than one precursor is used, they will mix together and diffuse inside.

The system is kept at low pressure by vacuum pumps. This system uses a booster pump and a mechanical backing pump. Booster pump is used to enhance the flow of gases and thereby the pumping speed. Mechanical backup does the real pumping and the combination provides a vacuum of as low as a milli torr. Booster pump is a Ruvac single stage roots pump operated at 220 V supply and the backing pump is a Trivac dual stage rotary vane pump. Nitrogen ballast gas is used in the pump to dilute any hazardous outgoing gas. An oil filtration system is also used to separate the micron size dust particles that are accumulated during the pumping process.

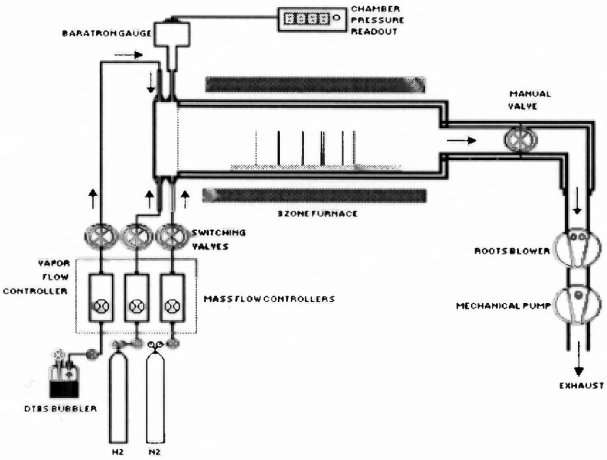

Fig. 3.17 LPCVD reactor

Wafers are loaded inside the tube using a quartz carrier boat. Wafers are kept vertically in the slots provided in the boat. The boat is kept inside of the quartz tube and the tube is sealed by the inlet lid. A manual control valve is provided at the output end to control the rate at which the gas is removed from the reactor. Precursor is allowed through a pneumatic control valve provided at the input end. Unloading of the wafers is done by bringing the reactor to atmospheric pressure by closing the valve and passing a controlled flow of nitrogen into the chamber.

3.2.1.2 Leakage Check A leak would result in a change in the deposit structure (due to oxygen) and could result in haze depending on the size of the leak, therefore a leakage check in the CVD is an important step before making an experiment. When carrying out leak check, all pneumatic controllers and gas regulators should be fully open to the gas cylinder main valves. The capillary is disconnected and the inlet is sealed with a plug because it is not possible to create vacuum in the capillary in the limited time period. After pumping the reaction system for a whole day, closing the outlet valve of the chamber, the pressure increasing rate was measured at a fixed period of time in the chamber to obtain the leakage rate. For this LPCVD system, the leakage rate deviated from 0.13 to 2 mTorr/min. Depending on the chamber condition a very low leak rate for a new chamber and higher leak rate for a chamber after long time will be in service. However, the leakage rate in the system was basically good.

3.2.1.3 Calibration of Gas Flow System The flow rates for the reactant gas DES and O_2 were calibrated by noting the increase in pressure in the reaction chamber with increase in time (the vacuum outlet being sealed). Using the ideal gas law, PV = nRT, the following formula could be deduced to calibrate the flow rate.

$$\frac{dV}{dt} = \left(\frac{V_r}{760}\right)\left(\frac{273}{T_m}\right)\left(\frac{dP}{dt}\right)$$

dV/dt is the flow rate of the tested gas in sccm, V_r is the pre-calculated volume of the reactor (20,900 ± 600 cm^3), T_m is the measured chamber temperature in kelvin and dP/dt is the rate of pressure increase. The tested gas in the vacuum conditions considered as an ideal gas and the reaction chamber was evacuated for several hours before testing. After setting up the flow rate, the gas regulator was opened to introduce the gas flow into the chamber, then the outlet valve of the chamber was closed and the pressure difference in the chamber was measured to obtain the rate of pressure increase. The real flow rate of the tested gas thus can be calculated using the above relation. The accuracy of this calibration involves the gas flow rate, the time interval, and the condition of the chamber should be carefully controlled. A smaller gas flow rate causes a slower pressure increase and thus leads to an easier detection of pressure increase and hence more accurate calibration. A longer time interval for calibration and a good vacuum condition in the chamber are also favored in the accuracy of calibration.

3.2.1.4 Liquid Injection System The liquid injection system, designed and fabricated in house, consists of a glass bubbler connected to a precalibrated capillary tube fastened onto the reaction chamber. The flow rate is inversely proportional to the length of the capillary, while proportional to the pressure differential and the cross sectional area. The injection system has filters for both nitrogen purge and liquid precursor. The bubbler is always maintained at a positive pressure to prevent oxygen leak into it. The liquid injection mechanism is used to inject TMP.

3.2.1.5 Deposition Procedure Silicon dioxide films were deposited on <100> oriented single crystal, single-side polished Si wafers (obtained from Silicon Sense Inc.), and fused quartz wafers (obtained from Hoya, Japan). The details of the Si wafers are given in table 3.5.

The wafers are labeled and accurately weighed (up to 4 decimal places) using an electronic balance. These wafers are then placed vertically on a quartz boat with a dummy wafer on its back side and loaded inside the tube at a distance of 89 cm from the reactor opening. The wafers were placed at 3 cm distance from each other. From front to rear downstreamly, the wafers were labeled as dummy wafer, wafer1, wafer2,..., dummy wafer which in the chapter 4 means the corresponding wafer position.

Table 3.5 Specifications of the Si wafer

Source	Silicon Sense Inc.
Diameter	100 mm/125 mm
Orientation	<100>
Thickness	525 ± 25 μm
Type/Dopant	P/Boron
Resistivity	5 - 15 Ω-cm
Grade	Test

In this study, the precursor gases were TMP, DES and O_2. TMP was lead into the chamber through liquid injection system. DES was delivered from a liquid source bottle. Due to the high vapor pressure of DES a carrier gas was not required. Oxygen was delivered from a high pressure gas cylinder. Both precursor gases were monitored using calibrated automatic mass flow controllers, Applied Materials model AFC 550. Stainless steel delivery lines were used to bring reactants into the reactor. A spare nitrogen mass flow controller was installed to incorporate any necessary additional reactant gas into the chamber or for backfilling. This spare controller could be calibrated for the gases other than nitrogen.

After loading, the furnace was brought to low pressure by pumping down the chamber. The temperature was raised to the required level slowly in steps of about 50°C per 15 minutes. The temperature was allowed to reach the set value in all the five zones before raising it further until the desired value is reached. Once the required temperature was reached, oxygen was first introduced followed by DES and, in the case of PSG films, TMP. That sequence was found to be important in order to minimize carbon incorporation in the films. The pressure was then set to the required value. Among the deposition parameters recorded were the total pressure, reaction temperature and flow rates of the reactants.

Samples were allowed to cool to room temperature and the wafers were removed from the reactor by introducing nitrogen to fill the vacuum chamber and rise the pressure to atmospheric pressure. The samples were then weighed and the deposition rate could be calculated by knowing the mass gain (mg/hr) due to deposition. Samples were observed in an optical microscope for the presence of microcracks and for gas phase nucleation.

Short runs (~2 hrs) were made initially to check the kinetics and resulting film qualities. Once these were established, long runs (>12 hrs) were undertaken to obtain the desired thick films. Deposition temperature was found to be the parameter most crucial in influencing the growth rates and film properties.

3.2.1.6 Film Characterization Film thickness was measured by a Nanospec interferometer which bases its estimation on the monochromatic light interface fringes formed within a zone limited by sample surface and a semi-transparent mirror. The device consists of Nanometrics Nanospec/AFT microarea gauge and SDP-2000T film thickness computer. The thickness of the film deposited on the wafer was measured at five different points. The refractive index provided was first estimated, as for silicon dioxide, 1.46 is the typical value. Deposition rate was determined as the film thickness over the deposition time, and averaged over all the wafers in the run. In the case of P-glass, the samples are analyzed in the same way as the oxide wafers. The Phosphorus content in the films can be found by many techniques, including direct chemical analysis, neutron activation analysis, infrared absorption, electron microprobe, etch rate variation, sheet resistivity after a standard diffusion and variation in the refractive index of the films. In this work the wafers had been sent to Balazs analytical Laboratory to determine the P content in the film.

Refractive index of the silicon dioxide films was determined using Rudolph Research/Autodec ellipsometry. The measurement technique is mainly concerned with the measurement of changes and the state of polarization of light upon reflection with the surface. It employs monochromatic, plane polarized light with its plane of polarization 45° to the plane of incidence. When the elliptically polarized light is reflected from an absorbing substrate its state of polarization is changed. The ellipticity of the reflected beam is determined by the relative phase difference δ and azimuth ψ. An in-built computer program numerically solves the equations generated by these δ and ψ and the refractive index and the thickness of the film is obtained. In all the experiments the angle of incidence was maintained at 70° and the wavelength at 5461Å. Readings were taken at 5 places on the wafer and was averaged out.

The levels of interstitial oxygen and phosphorus were determined by using infrared absorption spectroscopy. The analysis was done on a Perkin-Elmer 1600 series FTIR spectrophotmeter to determine the characteristics of the deposits. A spectrum of percent transmittance or absorption was obtained for samples of known thickness. The composition of phosphosilicate glass can be analyzed by infrared absorption plot. The ratio of the intensity of the P=O absorbance band at ~1325 cm^{-1} to that of the Si-O band at ~1050 cm^{-1} can be correlated with the composition of vapor deposited phosphosilicate glasses over the range 0-20 mol per cent P_2O_5. The properties of PSG that make it useful in a given application may depend on its composition. Hence, it must be possible to determine and control this composition. Composition control is usually achieved by controlling the temperature and reactant gas composition during the CVD of the PSG film. Composition determinations based on the IR spectra of vapor deposited borosilicate and arsenosilicate glasses have proven useful. The IR reflectance spectra of silicate glasses have been employed as a qualitative test for the presence of phosphorus oxide. Tenney and Ghezzo [138] have proposed a method to determine compositions of PSG. From the infrared plot, the linear absorption ratio for the glass (ratio of the linear absorption of PSG to that of pure SiO_2) is calculated. This ratio as a function of the glass composition for different temperatures was plotted by Tenney et al. A approximation for the P=O band area and a corresponding calibration curve was obtained. An average of both methods was used to obtain the phosphorus content in the given glass. In this study, the sample had been sent to Balaze Analytical Laboratory for analysis in order to get the precise content at different temperature.

The stress in the film was determined by a house developed device, employing a laser beam equipment which measures change in radius of curvature of the wafer resulting from the film deposited on one side. The considering the geometry of the instrument used is shown in Fig..3.18.

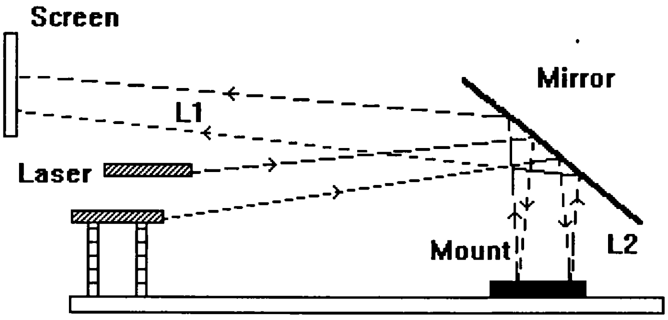

Fig. 3.18 Schema of optical system for stress measurement.

Two fixed and parallel He-Ne laser beams were incident on the wafer surface before and after deposition. The reflected beams from the two surfaces was then projected by an angled plane mirror as two points onto a scale in a certain distance, and thus, the separation can be measured more accurately. The change in separation of these two points was fed into Stony's Equation to obtain actual stress value. The calculation formula is:

$$\sigma_s = ED^2/6(1-v)Rt$$

where E and v are Young's modulus and Poisson ratio of the substrate. D, t are the substrate and film thickness' respectively, R is the radius of curvature of the composite. By convention R is negative for a complex wafer surface (compressive film stress) and positive for a concave wafer surface (tensile film stress). The equation reduces to

$$\sigma_s(\mathrm{MPa}) = 12.3R'/t\ (\mu m)$$

where R' is the difference of the deflection of the projected laser spots after and before deposition.

The optical transmission for the silicon dioxide film and phosphosilicate glass was measured from the film deposited on quartz wafers by using a UV-spectrophotometer.

3.2.2 Photolithography Processes

After LPCVD and characterization, the films were cleaned in M-Pyrol for each 10 minutes by using primary and secondary bath, rinsed in cold DI water for 10 minutes. Wafer drying was done using a spinner. 10 minutes P-clean is the second step. Subsequently, rinsing individually in hot DI water and cold DI water baths for 10 minutes. Then wafer was dried in spinner. Next, a thin layer of Aluminum was sputtered, with Varian 3125 DC magnetron sputtering system, onto the wafer surface to act as a mask layer during dry etch.

Next, the pattern of the waveguides was transferred to the wafer by using photolithographic processing. The mask used for waveguide is shown in Fig..3.7. The first step is the application of photoresist. The photoresist is applied by spin coating technique. This procedure involves three stages: a) dispensing the resist solution onto the wafer; b) accelerating the wafer to the final rotational speed; and c) spinning at a constant speed to establish the desired thickness (and to dry the film). The dispensing stage can either be accomplished by flooding the entire wafer with resist solution before the beginning of the spinning, or by dispensing a smaller volume of resist solution at the center of the wafer and spinning at lower speeds to produce a uniform liquid layer across the wafer. In the next stage the wafers are normally accelerated as quickly as is practical to the final spin speed and finally spinning at the constant speed to obtain desired thickness.

In this work, the rotational speed was maintained at 2000 rpm. The wafers were spun at this speed for a period of 20 seconds. This gave a photoresist of 2μm thickness. Prior to exposure the wafers are softly baked for one minute at 110°C and then cool down for 30 seconds at 18 ^{0}C. The exposure was carried out using a SUSS MA6 mask aligner. The lamphouse is equipped with a 350 W mercury high pressure lamp and a SUSS diffraction reducing optics. The usable wavelength falls between 350-450 nm. The lamphouse has an ellipsoidal mirror, and a 45° cold light mirror. The type of exposure lamp depends on the optical range selected. The cold light mirror reflects the desired short wavelength UV light through a fly's lens and transmits the longer wavelengths to a heat sink located in the bottom of the lamphouse. The lamphouse also contains a condenser lens, diffraction reducing lens plates, a 45° turning mirror and a collimation lens. A holder is provided in the mirror house for a filter. SUSS diffraction reducing exposure system provides a high resolution over the entire exposure area, resulting in steep resist edges and small diffraction effects.

The wafers were exposed for 18 seconds in the SUSS MA6 mask aligner. After the exposure the wafer must undergo "development" in order to leave behind the images which will serve as a mask for etching. The developer is poured on the wafer and allowed to develop for 30 second before it is spun at a high rpm (~2000). This procedure is repeated for another 60 seconds of development. The wafer is then washed with DI water and spun again to remove all the water. The wafers are baked for one minute at 115 ^{0}C to rid of the moisture that may been absorbed by the substrate and make the photoresist hard. The waveguides are then inspected under the microscope for their integrity.

The pattern was then wet etched into aluminum surface by placing it in Al-Etch bath for a few minutes. The wafer then rinsed in cold DI water for 10 minutes. The photoresist was then stripped in hot M-Pyrol primary bath for 10 minutes, secondary bath for 10 minutes and rinsed in cold DI water 10 minutes. Wafer drying was done using a spinner.

3.2.3 Reactive Ion Etching

Reactive ion etching as described before is an anisotropic etching technique. After the lithographic step, waveguide pattern was transferred to the wafer. PSG was exposed. RIE is carried out to remove these PSG and expose the underlying thick silicon dioxide.

Minilock RIE system (Trion Technology) of class 10 clean room in NJIT is a table top plasma RIE etching system designed to supply research and failure analysis with state-of-the-art plasma etch capability. The RIE reactor has four processing gases standard with an option for two or more additional gases that maybe used to anisotropically etch silicon dioxide, silicon nitride, and polyimide. This reactor can also be used to strip photoresist.

The specification of the Minilock RIE system is shown in table 3.6. The PSG film on the wafer surface was typically etched using the conditions in table 3.7. The aluminum layer severed as the mask of the waveguide pattern since the photoresist is easily stripped away. If RIE runs long, a Teflon film from CF_4 is formed on the etching surface, which slows and prevents the ions from attacking the wafer surface, it may be removed by adding some etching agent such as oxygen. But in this study, it was essential to etch the waveguide to depth (waveguide height) of ~7 μm, the polymer problem was not solved even by adding a large mount of oxygen. The wafer was sent out for RIE.

After the waveguide pattern was etched into the oxide, the aluminum was etched off in Al-Etch bath. The wafers were cleaned, rinsed, and dried. The resulting guides were examined with Dektak.

Table 3.6 Specification of the RIE system

Size	35" wide × 26" deep × 47" high
Maximum RF power	500 watts
System power required	300 A, 208 V
Gas channel	Four standard, can be increased to eight with purchase of extra gas cabinet
Maximum wafer size	8"

Table 3.7 Conditions for RIE of SiO_2

Power	250 W
Pressure	750mTorr
Flow rate of CF_4	25 sccm
Flow rate of CHF_3	25 sccm
Flow rate of O_2	0 or some
Temperature	25°C

3.2.4 Synthesis of Upper Cladding Oxide Layer

Next, a thin layer of silicon dioxide was deposited on to the wafer surface to act as an upper cladding layer of the waveguide pattern. The oxide layer was ~ 1 μm thick. The refractive index should be lower than that of the core (1.4666) and around that of the underlying cladding (1.4580). The best way is to use plasma enhanced chemical vapor deposition since PECVD has high deposition rate and is easy to adjust the refractive index of the film.

The deposition was processed in the clean room with Plasma-Therm 790 series system (Plasma – Therm, Inc.) that can be used as RIE (reactive ion etch), PE (plasma etch), PECVD, and ICP (inductively coupled plasma) systems. This system is capable of providing ion densities of the order $10^{13}/cm^3$. Aluminum chamber houses two circular parallel plates through which the RF power (13.56 MHz) can be capacitively coupled to the plasma. The reactor can handle up to 200 mm large wafer. The lower electrode temperature is maintained by running cooling/heating water in the coils. The chamber is constantly kept under a base pressure of about 10-6 Torr with the help of a Leybold turbo-molecular pump backed by a powerful Leybold rotary vane mechanical pump. The chamber lid is opened manually for top loading of the samples. The three pyrex glass view ports on the lid can be used mount plasma diagnostic tools.

The system is using a computer that also allows convenient monitoring of the system status on a graphical interface. The valves are safely interlocked and a number of control sequences built in the software assure smooth and safe running of the equipment. The temperature range used in this system is 80 – 400 ^{0}C and typical deposition temperature is 100 – 350 ^{0}C. The chamber wall is normally set at 50 ^{0}C. In this study, the condition of PECVD SiO_2 is listed in table 3. 8.

Table 3.8 Conditions for PECVD of SiO_2

SiH_4 (3%) flow rate	400 (sccm)
N_2O flow rate	900 (sccm)
Power (RF)	25 (W)
Temperature of substrate	250 ^{0}C
Temperature of chamber wall	50 ^{0}C
Pressure	900 (mtorr)
Growth rate	430(Å/min)

After PECVD, the film needed lithography again to open a window over the sampling arm using window mask of Fig. 3.10. Photoresist acted as the RIE mask for next etching since this time only ~1 μm silicon dioxide was needed to remove and photoresist would be not stripped. After the removal of PECVD silicon dioxide over the window, the sampling arm could be exposed to the environment and reference arm was protected by upper cladding PECVD silica film. Then cleaning of the wafer with M-pyrol was followed in order to remove the photoresist, the final Mach-Zehnder interferometer product was present.

CHAPTER 4

RESULTS AND DISCUSSION

4.1 LPCVD Kinetics of Silicon Dioxide

The deposition kinetics of the SiO_2 films was investigated by monitoring the growth rate of the resulting films after each deposition. The deposition temperature, pressure, reactant flow rates, and wafer position were systematically varied in each deposition so that their effects on the film growth rate would be determined. Aside from the film growth rates, the properties of the SiO_2 films such as the refractive index, density, stress, etch rate, composition, and optical transmittance were also ascertained.

4.1.1 Temperature Dependent Study

In this part of the LPCVD optimization process, two kinds of depositions were made. In the first case, the deposition temperature was varied from 550 ^{0} C to 700 ^{0} C and the oxygen/DES flow ratio had the value of 2 (Fig 4.1). In the second case, the deposition temperature was varied from 700 ^{0} C to 800 ^{0} C and the oxygen/DES flow ratio had the value of 10 (Fig 4.2). The pressure was kept at 200 mTorr for both depositions. The corresponding film growth rates were monitored in terms of the thickness that was measured after each run. The activation energies of reactions were estimated. The film refractive index (Fig 4.3), stress (Fig 4.4 and Fig 4.6), and density (Fig 4.9) were also monitored along the given temperature.

As shown in Fig. 4.1, the deposition rate increased from 180 Å/min to 502 Å/min in the range of 550 ^{0} C - 700 ^{0} C at O_2 : DES = 2 : 1. A slight drop is observed in Fig. 4.2 after 750 ^{0} C at O_2 : DES = 10 : 1. The deposition rates were plotted as the function of 1000/T, where T is the Kelvin temperature. The diagrams show the linear dependence of the logarithmic of film growth rate on inverse temperature. Film growth kinetics can be considered to follow a thermally activated heterogeneous mechanism characterized by the rate equation:

$$\text{Rate}_{\text{deposition}} = K \times \exp(-E/RT)$$

Where

E is the apparent activation energy of deposition

K is rate constant

R is the gas constant

T is absolute temperature

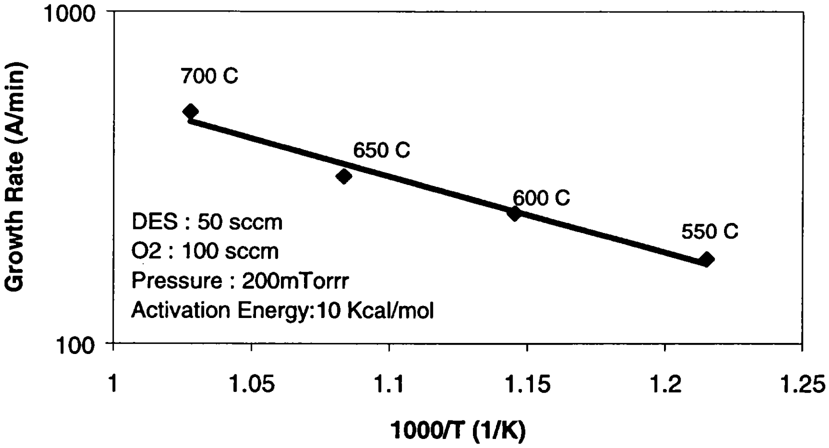

Fig. 4.1 SiO_2 film growth rate on Silicon wafers as a function of deposition temperature at O_2 : DES = 2 : 1

The activation energy of reaction was estimated by linear regression analysis for the points corresponding to 550 ^{0} C –700 ^{0} C. Activation energy of 10 KCal/mol identical to an earlier obtained value of 10 KCal/mol [104] was then observed as indicated in Fig. 4.1. This value suggests a rate mechanism controlled by gas-phase diffusion in the mass transfer limited regime. As seen in Fig. 4.2, the O_2/DES flow ratio was much higher than that of Fig. 4.1. The Arrhenius behavior became less obvious when temperature kept increasing. Either mass transportation or surface reaction served to be a rate-limiting step. In addition, the increased occurrence of reaction reduced the amount of the reactants reaching the wafer surface, which led to a slight drop in deposition rate after 750 ^{0} C in Fig. 4.2.

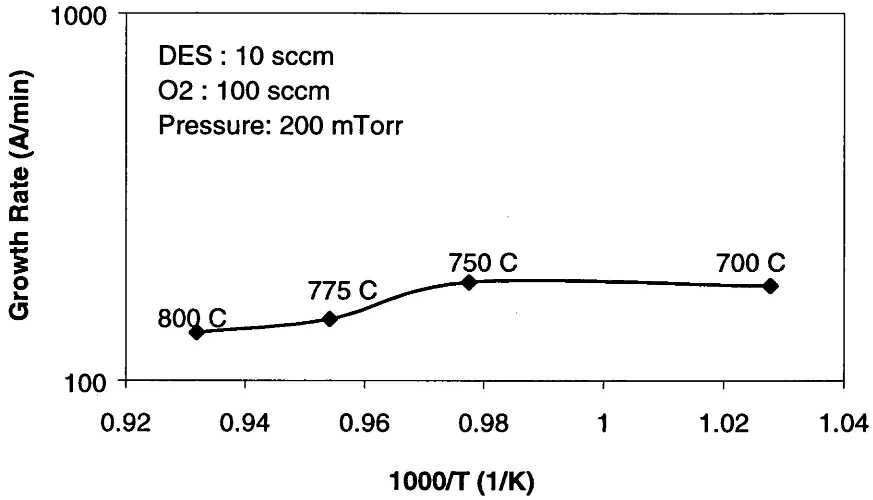

Fig. 4.2 SiO_2 film growth rate on Silicon wafers as a function of deposition temperature at O_2 : DES = 10 : 1

The refractive indices of the films were measured with a Research Auto EL Ellipsometer at a wavelength setting of 632.8 nm at five different points on the wafer. The average was then taken for plotting as the function of temperature as shown in Fig. 4.3. It was observed that the refractive indices were in the range of 1.47 ~ 1.49 with respect to the change in deposition temperatures. In the previous study [104], refractive indices close to a value of 1.45 ~ 1.46 were observed in the temperature range 350 ^{0}C-475 ^{0}C. It was suspected that at these higher temperatures the non-stoichiometric silicon rich films were formed with the higher DES flow rate. At lower temperatures, the refractive indices of the oxide compared with that of a thermal oxide that shows a stoichiometric oxide were observed. The value of 1.45 ~1.46 was indicative of homogenous SiO_2 film. Therefore such a value was considered.

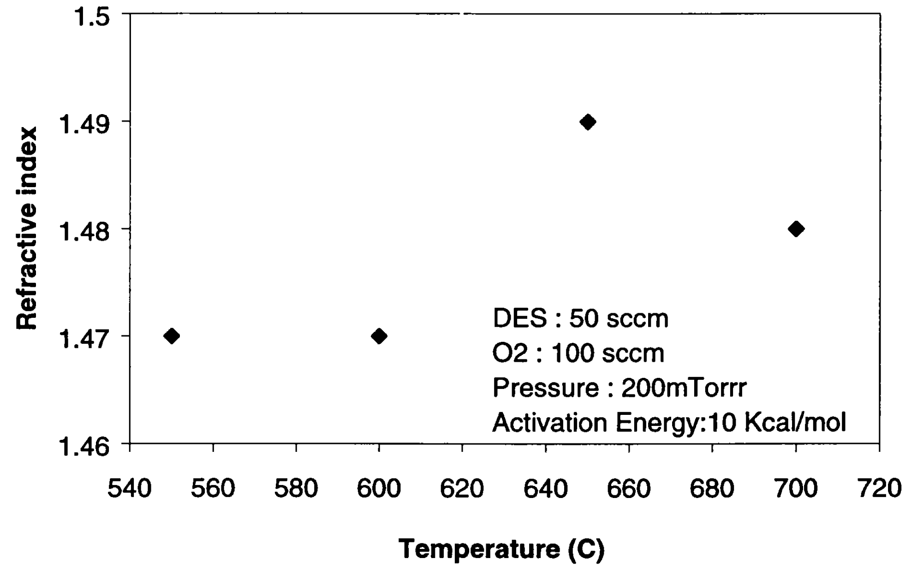

Fig. 4.3 SiO_2 film refractive index as the function of deposition temperature

The stress of the films was tensile throughout as indicated by the positive values at O_2 / DES = 100 sccm / 50 sccm. It was plotted as the function of deposition temperature in Fig. 4.4. The stress as the function of growth rate was shown in Fig. 4.5. At lower temperature, the precursors reacted with each other to form the amorphous film. Oxygen atoms have smaller diameter as compared to those of silicon atoms, which produced the intrinsic tensile stress when oxygen atoms virtually replaced silicon atoms. Since the thermal expansion coefficient of silicon (2.33×10^{-6}/ K) is larger than that of silicon dioxide (0.55×10^{-6} /K) [139], it is easy to relieve the tensile stress after further increasing temperature. At high temperature, silicon dioxide film becomes compressive.

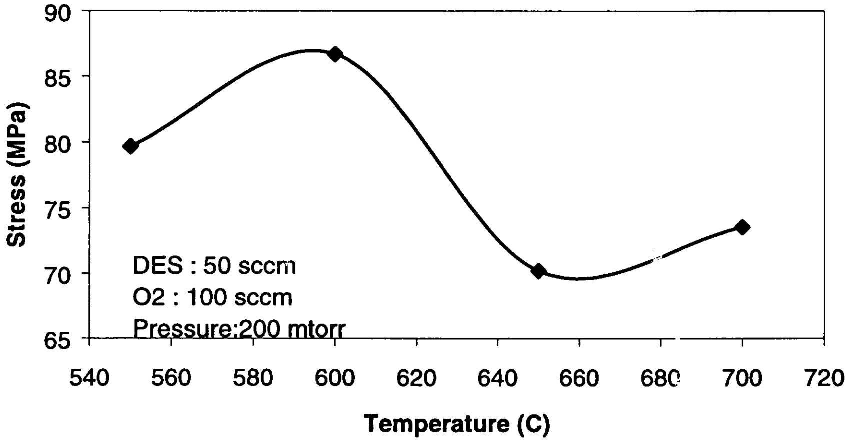

Fig. 4.4 Stress of the SiO_2 film as the function of temperature at O_2 : DES = 2: 1

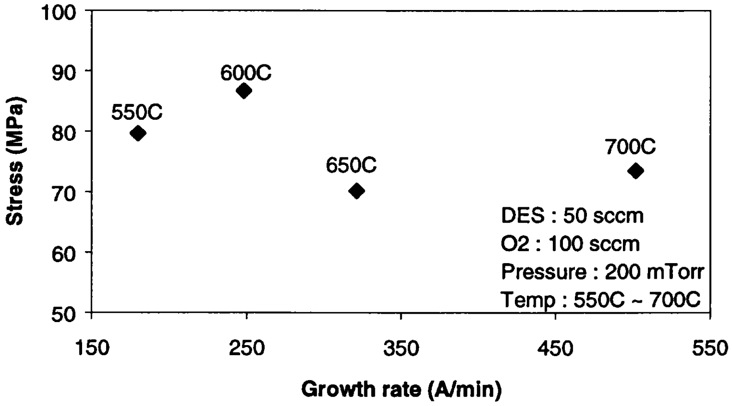

Fig. 4.5 Stress of the SiO_2 film as the function of growth rate

When the deposition conditions were changed to O_2 /DES flow ratio equal to 10 (100 sccm / 10 sccm), and the temperature in the range of 700 ^{0} C – 800 ^{0} C, the stress varied from low tensile at 700 ^{0} C to low compressive at 800 ^{0} C which was highly desirable in the synthesis of the thick films. As shown in Fig. 4.6, at 775 ^{0}C, the stress was as low as 3.88 MPa and compressive. Hence this temperature had been chosen as ideal in the synthesis of thick silicon dioxide films at the oxygen to DES flow ratio of 10:1, and growth rate is 132 Å/min.

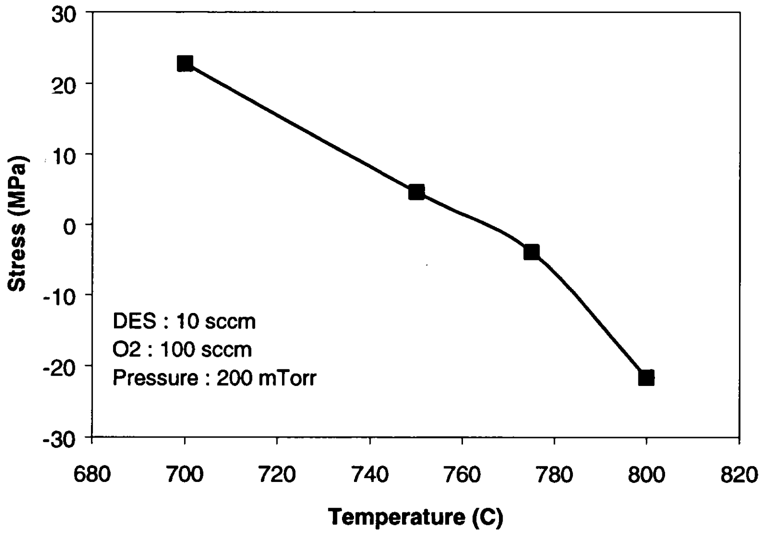

Fig. 4.6 Stress of the SiO_2 film as the function of temperature at O_2 : DES = 10 :1

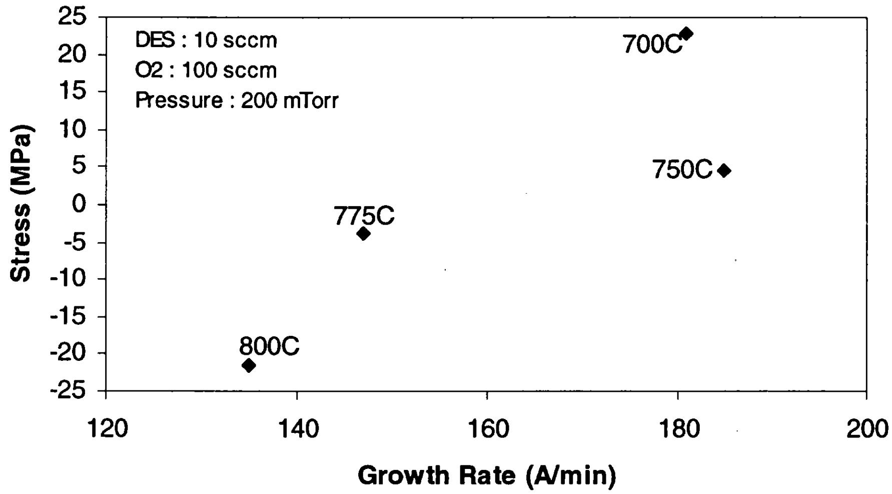

Fig. 4.7 Stress of SiO_2 film as the function of the growth rate

The thickness of the oxide films was measured with a Leitz or Nanospec Interferometer at a wavelength setting of 480 nm at thirteen different points. The average film thickness was then taken for plotting as the function of the mass of the oxide films shown in Fig. 4.8. Although it is almost linear, the small deviation of the data from the line indicated the dependence of density on the process variables as shown in Fig. 4.9. The change of the densities with temperature was observed over the temperature range of 550 ^{0}C ~ 700 ^{0}C. The density values obtained at 550 ^{0}C, 600 ^{0}C, 650 ^{0}C and 700 ^{0}C were individually 1.9307, 2.2788, 2.3201 and 2.3105. Lower film density at 550 ^{0}C was due to the excessive gas phase nucleation or the oxygen rich film. At high temperature, density larger than the value of 2.27 g/cm^3 for thermal oxide was due to the non-stoichiometric silicon rich film formed (the density of silicon is 2.33 g/cm^3).

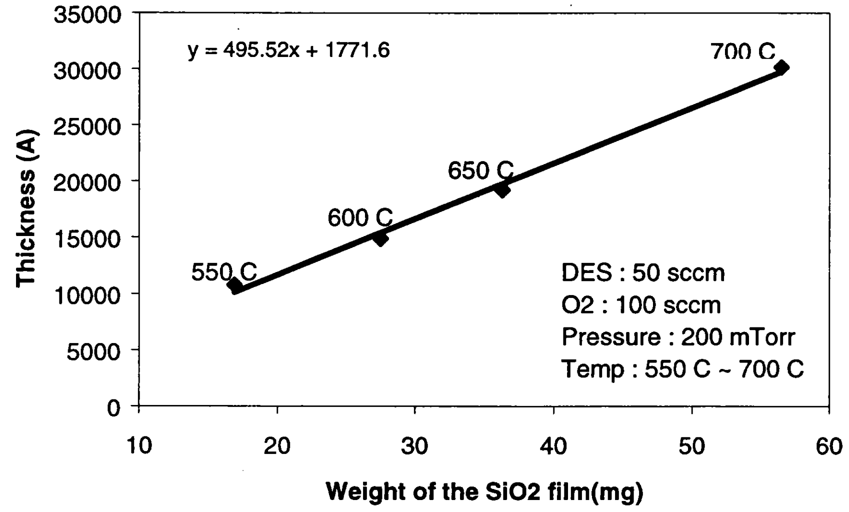

Fig. 4.8 Thickness as the function of the mass of the SiO_2 film

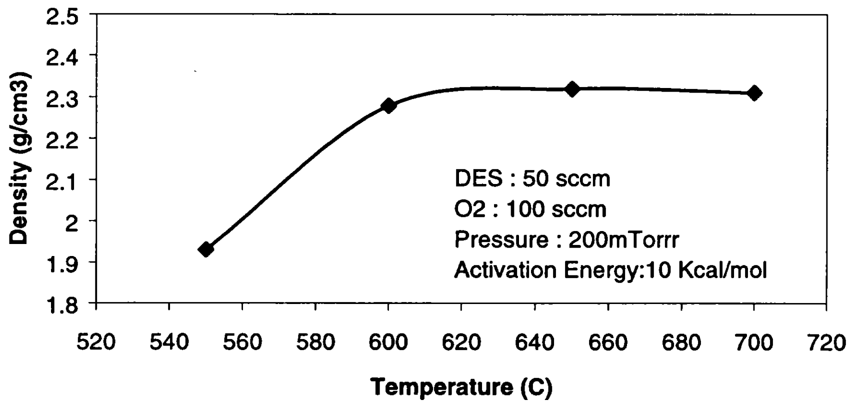

Fig. 4.9 SiO_2 film density as the function of deposited temperature

The thickness uniformity in terms of the thickness variation (%) as the function of deposition temperature was presented. Since higher deposition temperature can improve film uniformity, the variation percentage of the film thickness decreased as the temperature kept going up. As shown in Fig. 4.10, the oxide film deposited at high temperature had better uniformity than that deposited at low temperature. But in our study, the uniformity was not stable.

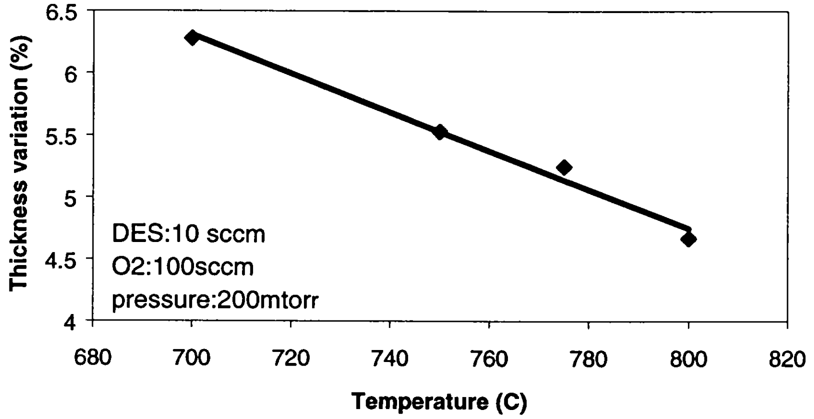

Fig. 4.10 Thickness variation of SiO_2 as the function of temperature

4.1.2 Ratio of Oxygen to DES Dependent Study

Since silicon dioxide films were deposited under various ratios of oxygen to DES, the dependences of the resulting film properties such as growth rate, stress and thickness on the ratio of O_2/DES were investigated. The change of oxygen flow rate did not have much effect on the growth rate of films as shown in table 4.1. When keeping the DES flow rates constant, the growth rates of film showed very small changes (however, there were errors associated with the measurement instruments) although the flow rates of oxygen showed a lot of changes. For example, the growth rate of SiO_2 switched from 146.8 Å/min to 132 Å/min with oxygen flow rate increasing twice (775 ^{0}C), and from 180 Å/min to 201 Å/min with oxygen flow rate increasing 1.5 times (550 ^{0}C). The changes of growth rates from 364Å/min to 502 Å/min (700 ^{0}C) and from 208 Å/min to 321 Å/min (650 ^{0}C) were not so significant since the oxygen flow rate was four times bigger than that before. But if oxygen was kept constant at 700 ^{0}C, the growth rate changed from 181 Å/min to 502 Å/min when DES increased from 10 sccm to 50 sccm. That illustrated the DES diffusion to the surface was the rate-limiting step at these temperatures.

Table 4.1 Properties of the SiO_2 film at pressure = 200 mTorr

Temperature (^{0} C)	Ratio of O_2 : DES	O_2 (sccm)	DES (sccm)	Stress (Mpa)	Thickness (Å)	Growth rate (Å/min)
775	10 : 1	100	10	3.88(C)	47533	132
	5 : 1	50	10	3.5 (C)	52859	146.8
	2 : 1	100	50	crack	Null	Null
700	10 : 1	100	10	22.77(T)	10870	181
	2 : 1	100	50	73.55(T)	30178	502
	1 : 2	25	50	crack	21887	364
650	2 : 1	100	50	70.22(T)	19200	321
	1 : 2	25	50	82(T)	12120	208
550	3 : 1	150	50	91.75(T)	12066	201
	2 : 1	100	50	79.7(T)	10802	180

* T = tensile stress C = compressive stress

From table 4.1, the films tend to be more tensile and easier to crack when the ratio of O_2/DES is reduced. For example, when the O_2/DES ratios were equal to 1 : 2 (T = 700 ^{0}C) and 2 : 1 (T = 775 ^{0}C), the oxide films deposited on both conditions were cracked because of high tensile stress. The same phenomenon occurred at other deposition temperatures. The possibility of cracking for low ratios of O_2/DES was obviously larger than that of high ratios of O_2/DES. It was seen in table 4.3. More than half of the films deposited at lower ratios of O_2/DES were cracked. Even if the films survived, they had very high tensile stress. So lower ratios of O_2 /DES were not favorable to get the thick oxide films since higher DES flow rate increased not only the growth rate of silicon dioxide, but also the intrinsic stress that resulted in the cracking.

Table 4.2 Possibility of cracking at different O_2/DES ratio (P=200 mTorr)

Ratio of O_2 : DES	Number of deposited wafers	Number of cracking wafer	Comment
10 : 1	8	0	Temperature above 700 ^{0}C, Deposition time 6 hours
5 : 1	2	0	Temperature is 775 ^{0}C Deposition time 6 hours
2 : 1	13	9	Temperature is 500 ~ 775 ^{0}C Deposition time 1.5 ~ 6 hours Wafers without cracking have high tensile stress
1 : 2	4	2	Temperature is 500 ^{0}C ~ 700 ^{0}C Deposition time 1 ~ 1.5 hours Wafers without cracking have high tensile stress

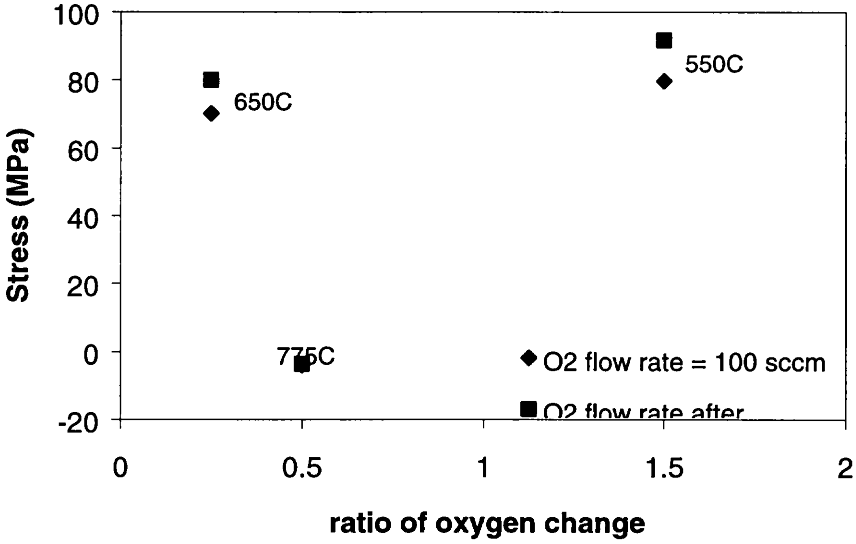

Fig. 4.11 Stress as the function of oxygen change (DES=50 sccm)

The change of oxygen flow rate did not have much effect on the stress of film as shown in Fig. 4.11. The stress did not change much when the flow rate of DES was kept constant. But if the oxygen flow rate was kept constant (100sccm), the stress changed from 22.77 (T) Mpa to 73.55 (T) Mpa at 700 ^{0}C when DES varied from 10 sccm to 50 sccm. It consisted with the leveling effect on film growth rate as discussed before.

4.1.3 Reactive Ion Etching of Undoped SiO_2

The etch rate of the undoped silicon dioxide films is shown in Fig. 4.12. The deposited conditions of the films were: DES =10 sccm, O_2 =100 sccm, deposition temperature = 775 ^{0}C, and pressure = 200 mTorr. The parameters of the RIE were: pressure = 750 mTorr, RF power = 250 W, CF_4 = 25 sccm, and CHF_3 = 25 sccm. The etch rate of silicon dioxide film was 460 Å/min which was very close to that of the thermal growth silica (450 Å/min). But when etching the thick silicon dioxide films, a white polymer layer was produced after long time running (about 15 minutes). This layer was Teflon film. Even after adding a large mount of O_2, it was very difficult to remove this layer

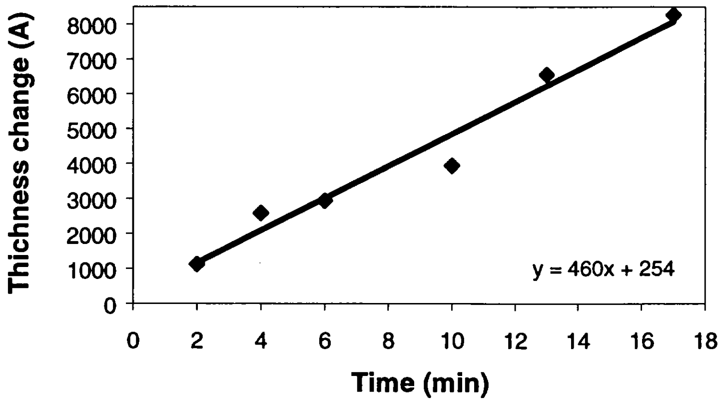

Fig. 4.12 Thickness change of reactive ion etch as the function of time

4.1.4 Position of Wafers Dependent Study

Depletion usually exists for all deposition. In order to study the influence of the hot wall reactor, growth rates of the wafers placed in position No. 1 to No. 8, as shown in Fig. 4.13, had been measured. These wafers were placed vertically on a quartz boat with a dummy wafer on its back side and loaded inside the tube at a distance of 89 cm from the reactor opening. The wafers were placed at 3 cm distance from each other.

Fig. 4.13 Position of wafers from No.1 to No. 8 (from left to right), both ends were dummy wafers

Due to the consumption of reactant on the wall, the partial pressures of the precursors in the deposition zone were reduced and the deposition rate at the rear was slower than that at the front. The depletion in the deposition rate can be defined as:

$$\frac{\text{Dep.Rate(position 1)} - \text{dep.Rate(position 1,2,\ldots,8)}}{\text{Dep.Rate(position 1)}} \times 100\%$$

The depletion percentage as the function of wafer position is shown in Fig. 4.14. It was found that the depletion became large when the distance between the wafer position and the reactor opening increased. It was obvious that the concentration of reactant at the front of reactor was larger than that at the rear.

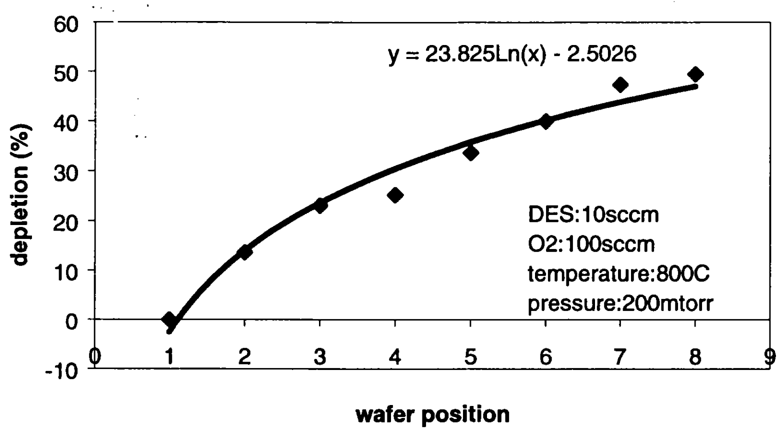

Fig. 4.14 Depletion as the function of wafer position

4.1.5 Optical Transmission of SiO_2 Film

The optical transmittance of the silicon dioxide film is shown in Fig. 4.15. The film was almost 100% transparent to the light with wavelength longer than 300 nm. This meant the film was transparent in the near-infrared and infrared area. Silicon dioxide could thus be used as a waveguide material.

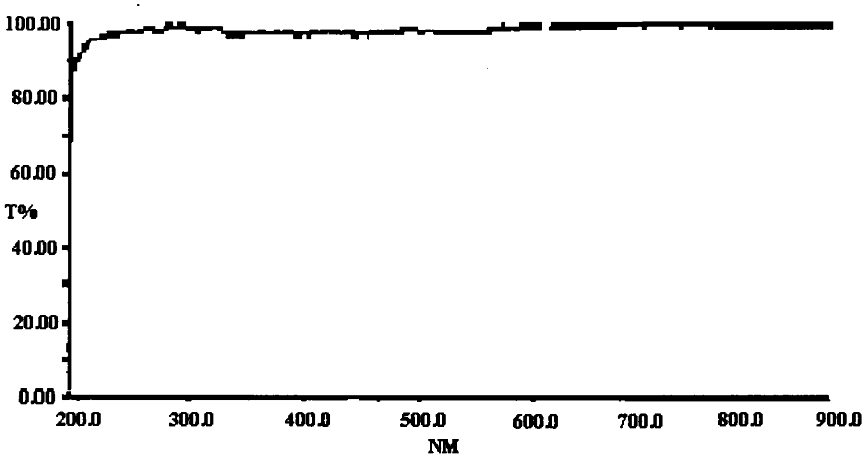

Fig. 4.15 UV spectrum for silicon dioxide.

4.2 LPCVD Kinetics of P-Glass

The phosphosilicate glass thin films were deposited on the silicon wafer and quartz wafer at temperatures ranging between 500 ^{0}C and 775 ^{0}C, and various flow rates of TMP. The properties of PSG as the function of the deposition parameters are presented in this section.

4.2.1 Growth Rate Analysis

The dependence of the growth rate on TMP flow rate is presented in Fig. 4.16. At first, when the TMP flow rate kept going up, the deposition rate increased, then tended to be saturated at the TMP flow rate with the value of 2.5 sccm, and reached the maximum (254 Å/min). After that, the deposition rate decreased with further increasing TMP flow rate. This increase-maximum-decrease behavior of the deposition rate obtained with increasing TMP flow rate had been investigated in the previous study [100], which could be explained by the retardation theory. Here, TMP had a retarding effect on the DES oxidation.

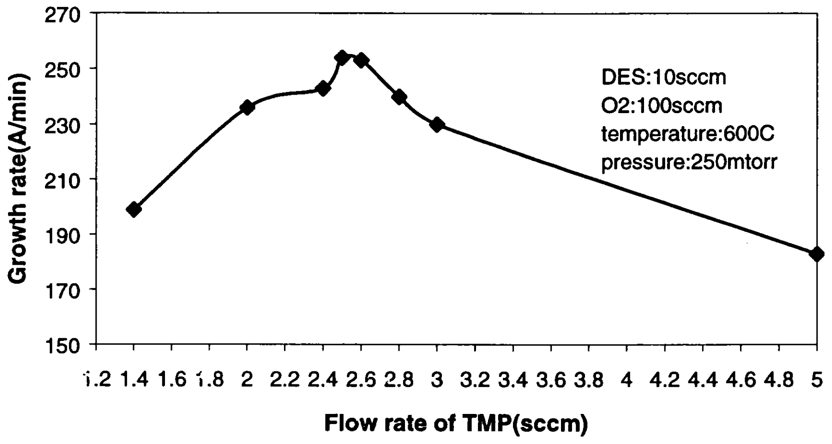

Fig. 4.16 PSG growth rate as the function of TMP flow rate

The temperature dependence of the deposition rate of PSG is shown in Fig. 4.17 and Fig. 4.18. An Arrhenius behavior could not be observed. There were two maximum growth rates 241 Å/min (650 ^{0}C, and TMP = 3sccm) and 183 Å/min (600 ^{0}C, and TMP = 5sccm). When the deposition temperature was further increased, more reactant gases were consumed on the reactor wall or somewhere else, which caused the drop of the deposition rate. The temperature had more significant effect on the deposition rate than TMP flow rate did.

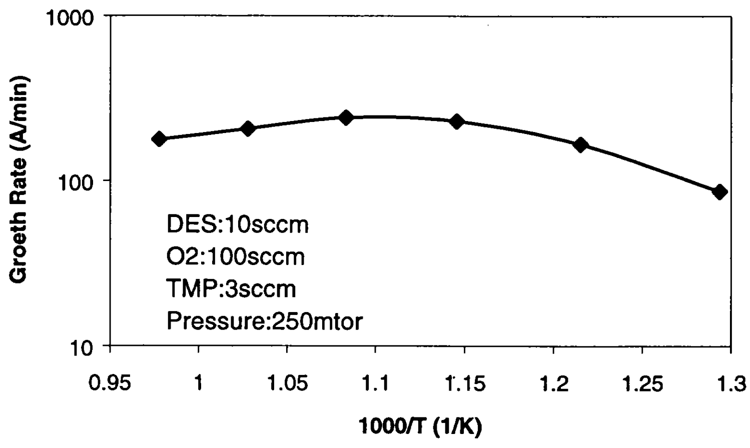

Fig. 4.17 Growth rate as the function of temperature at TMP=3 sccm

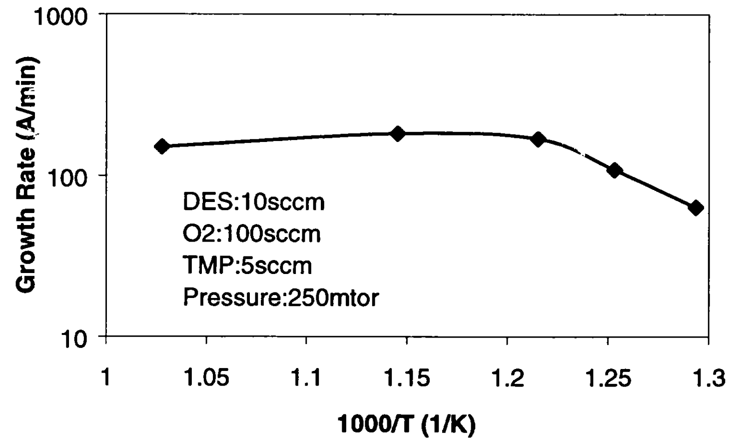

Fig. 4.18 Growth rate as the function of temperature at TMP= 5 sccm

4.2.2 Depletion Analysis

Depletion of the PSG deposition had been studied and the results are shown in Fig. 4.19 and 4.20. It was found that the depletion became large when the TMP flow rate or temperature was increased. This phenomenon was illustrated by the consumption of the reactant gas. The higher temperature or TMP flow rate, the more consumption on the reactor wall. Thus the partial pressures of reactants in the deposition zone were reduced, and the deposition rate at the rear was slower than that at the front. The depletion in the deposition rate of PSG can be defined as:

$$\frac{\text{Dep.Rate of the front one} - \text{Dep.Rate of the back one}}{\text{Dep.Rate of the front one}} \times 100\%$$

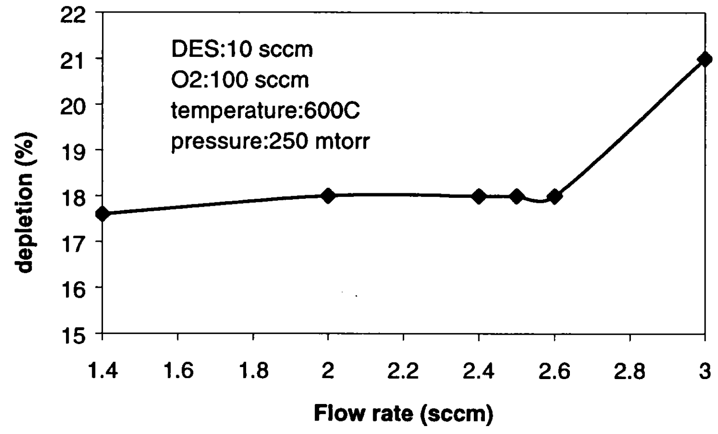

Fig. 4.19 Depletion as the function of flow rate

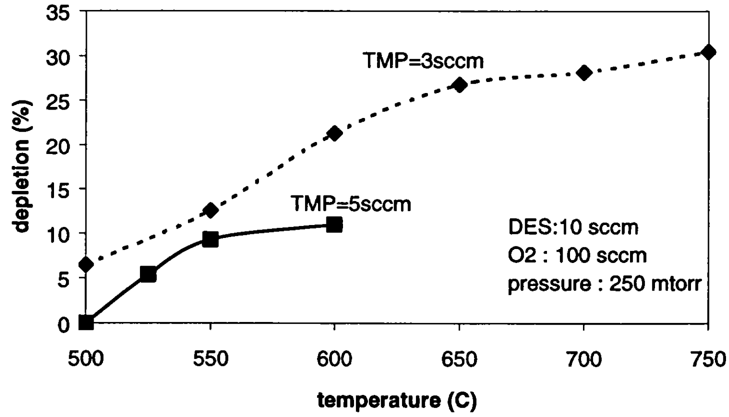

Fig. 4.20 Depletion as the function of temperature

4.2.3 Stress Analysis

The stress in the PSG films prepared as the function of the TMP flow rate and temperature is shown in Fig. 4.21, Fig. 4.22 and Fig. 4.23. As the TMP flow rate increased (Fig. 4.21), the tensile stress dropped gradually. Then tensile stress changed to compressive stress, which in turn increased. The phosphorous oxide in the PSG changed the structure and the thermal expansion coefficient of silicon dioxide. Higher TMP flow rate made silicon dioxide film more compressive.

Fig.s 4.22 and 4.23 depict stress as a function of temperature. The same rule was followed as in the case of the previous silicon dioxide. At lower temperature, amorphous PSG film was tensile because of the intrinsic stress. When the temperature was increased, the difference of the thermal expansion coefficient between PSG and silicon substrate resulted in the compressive stress of the film.

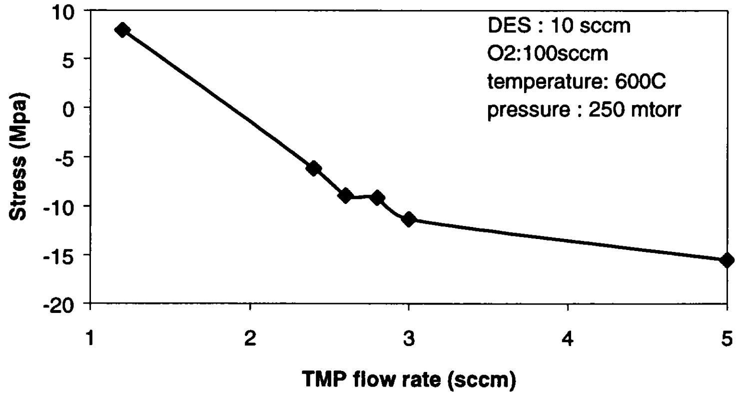

Fig. 4.21 Stress of PSG film as the function of TMP flow rate

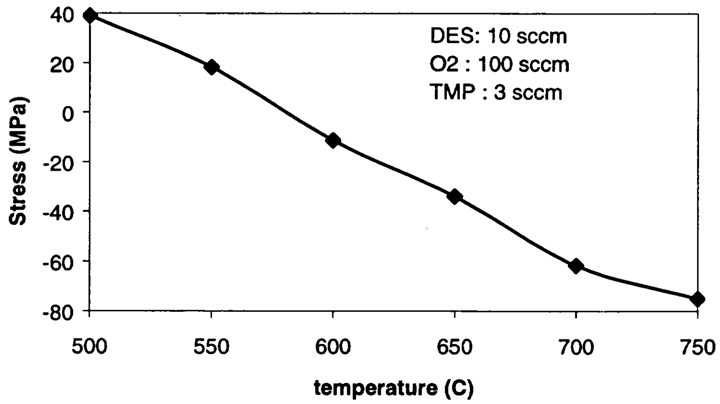

Fig. 4.22 Stress of PSG film as the function of temperature at TMP=3sccm

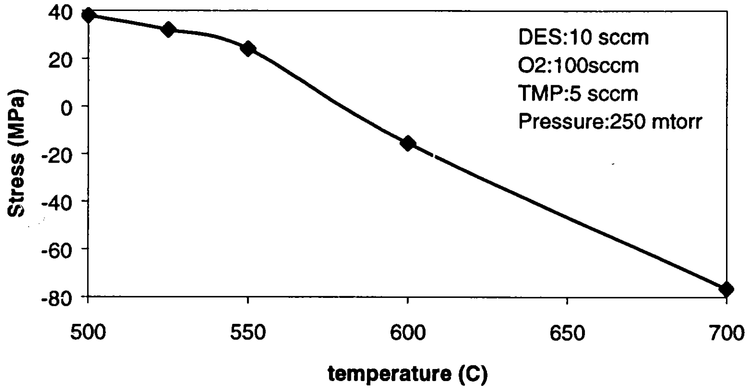

Fig. 4.23 Stress of PSG film as function of temperature at TMP=5sccm

4.2.4 Concentration Analysis

The concentration of the phosphorous oxide increased with the TMP flow rate, and remained saturated at the fixed temperature. It was observed that the phosphorous weight percentage was around 9 % after the TMP flow rate obtained the value of 2.5 sccm at 600 ^{0}C (Fig. 4.24).

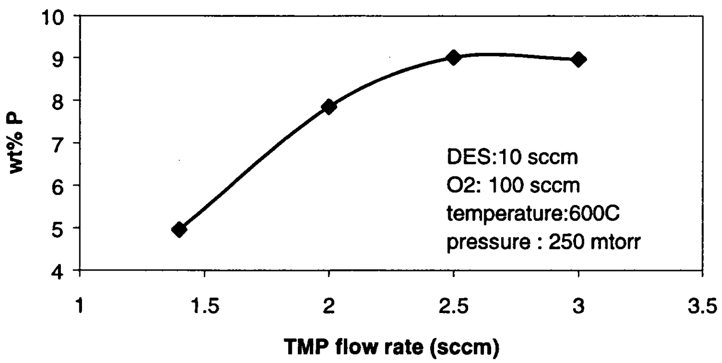

Fig. 4.24 Concentration of phosphorous as the function of TMP flow rate

The weight percentage of the phosphorous in PSG as a function of temperature is plotted in Fig. 4.17. It was observed that as the temperature increased, initially the weight percentage of phosphorous dropped, then increased and gained a maximum of 10.78 % at 650 ^{0}C, and decreased again. It has been already mentioned that the growth rate was also the maximum of 241 Å/min at 650 ^{0}C.

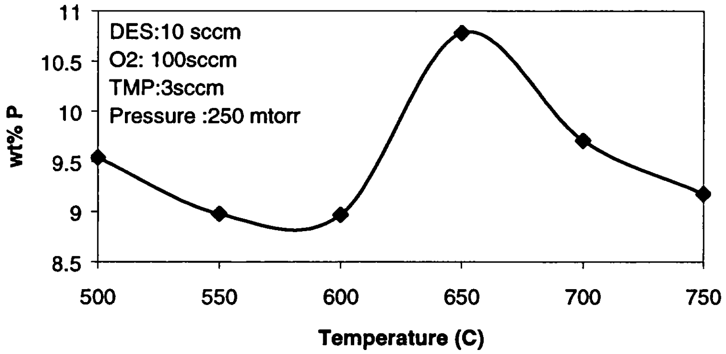

Fig. 4.25 Concentration of phosphorous as function of temperature

4.2.5 Refractive Index Analysis

The refractive index was obtained by averaging 5 points that were measured on every wafer. The dependence of the refractive indices on the deposition temperature is shown in Fig. 4.26 and has the same curve shape as in Fig. 4.25. It indicated that the refractive index analysis was consistent with the previous concentration analysis. The refractive indices got the maximum 1.55 at 650 ^{0}C due to the maximum phosphorous concentration at this temperature. The combination of the phosphorous oxide concentration and the densification decided the refractive index of the film.

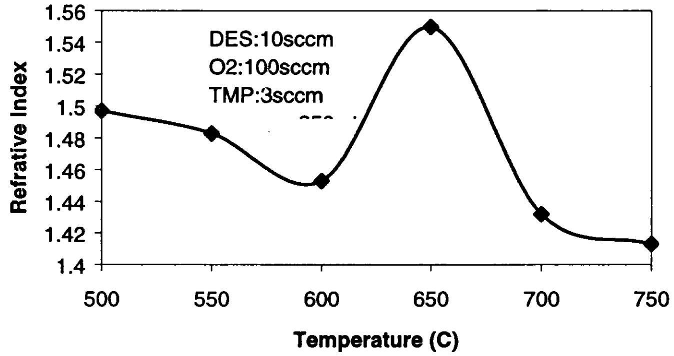

Fig. 4.26 Refractive index of PSG as the function of temperature

Fig. 4.27 shows the refractive index as the function of TMP flow rate. The refractive indices increased with an increase in the TMP flow rate and got the maximum at the TMP flow rate value of 5 sccm. While TMP flow rate was further increased, a slight drop of the concentration of phosphorous oxide, from 9.07 wt% (TMP=2.5 sccm) to 8.97wt% (TMP=3sccm), resulted in the decreasing of the refractive index.

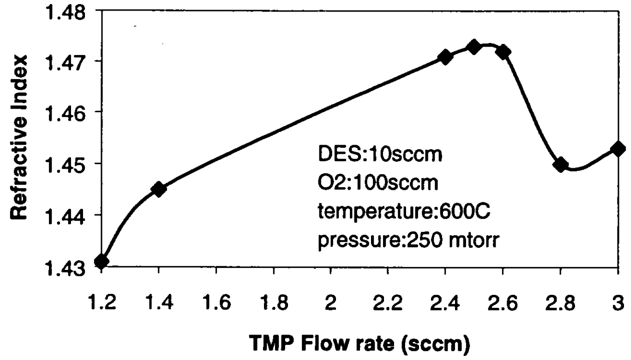

Fig. 4.27 Refractive index of PSG as the function of TMP flow rate

4.2.6 Uniformity of PSG Film Analysis

The thickness uniformity of PSG film is in terms of thickness variation (%) and is plotted as a function of temperature (Fig. 4.28). Contrary to the silicon dioxide film (Fig. 4.10), decreasing the temperature caused an improvement of the thickness uniformity across the wafer. Since the phosphorous oxide concentration became lower when temperature increased from 500 °C to 550 °C, the distribution of phosphorous oxide was not uniform at low concentration, which resulted in the increasing of thickness variation.

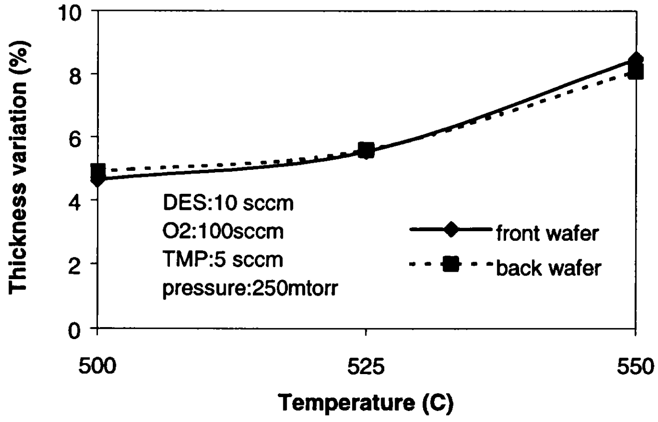

Fig. 4.28 Thickness uniformity of PSG as the function of temperature

4.2.7 FTIR and Optical Transparency of PSG Analysis

For all depositions, the Si-O stretching, bending, and rocking modes were identified at 1080, 800, and 460 cm^{-1} respectively by FTIR spectroscopy. Fig. 4.29 and Fig. 4.30 were FTIR spectrums of the PSG films deposited at different temperatures. The other deposition conditions were: TMP = 5sccm, Pressure = 250 mTorr, and O_2 /DES = 10 : 1 (100 sccm : 10sccm). 1327 cm^{-1} is the typical peak of P-O bonding. The flat peak around 1080 cm^{-1} was due to the vibration of Si-O bonding. No carbon was found in the films. The same explanation could be used for Fig. 4.31 and Fig. 4.32 that were the FTIR spectrums at TMP = 3sccm for different temperature. Other deposition conditions were the same.

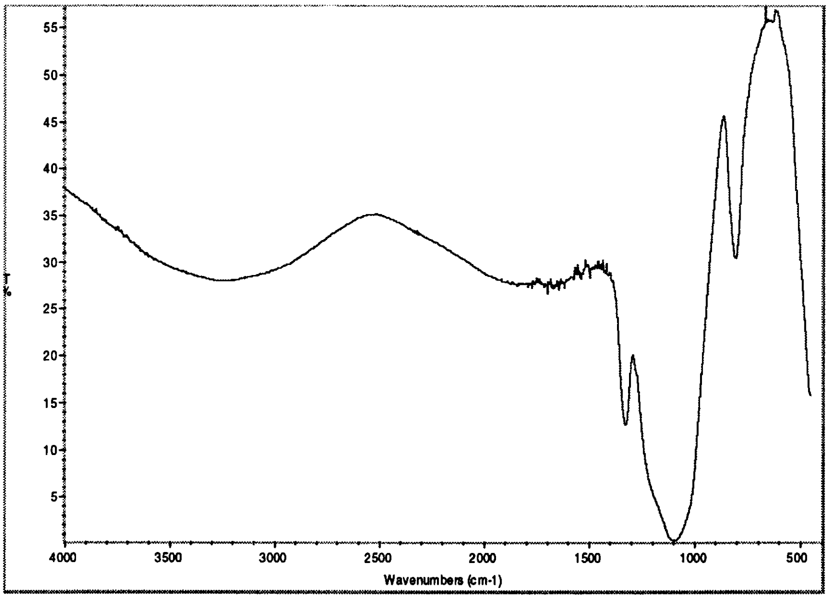

Fig. 4.29 FTIR of PSG film at temperature = 500 ^0C and TMP=5sccm

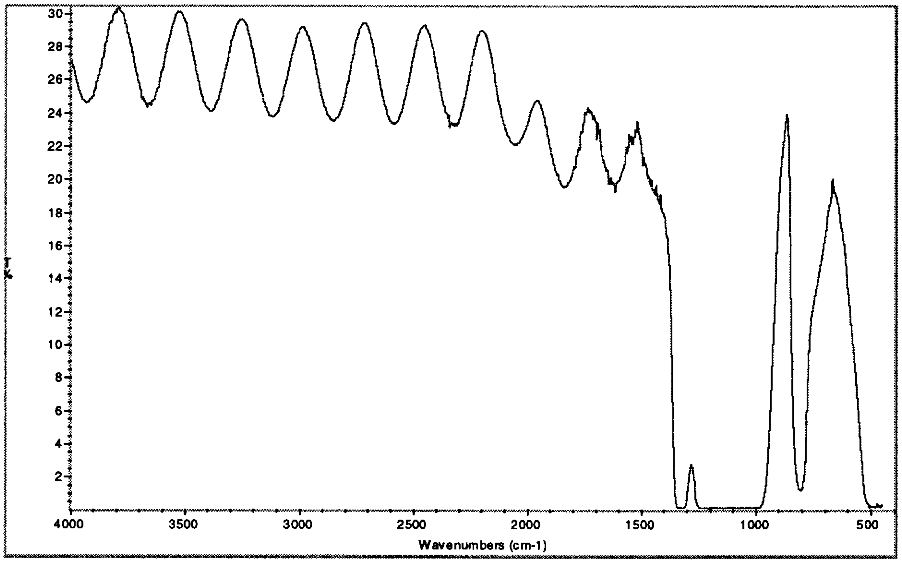

Fig. 4.30 FTIR of PSG at temperature = 600 ^{0}C and TMP=5sccm

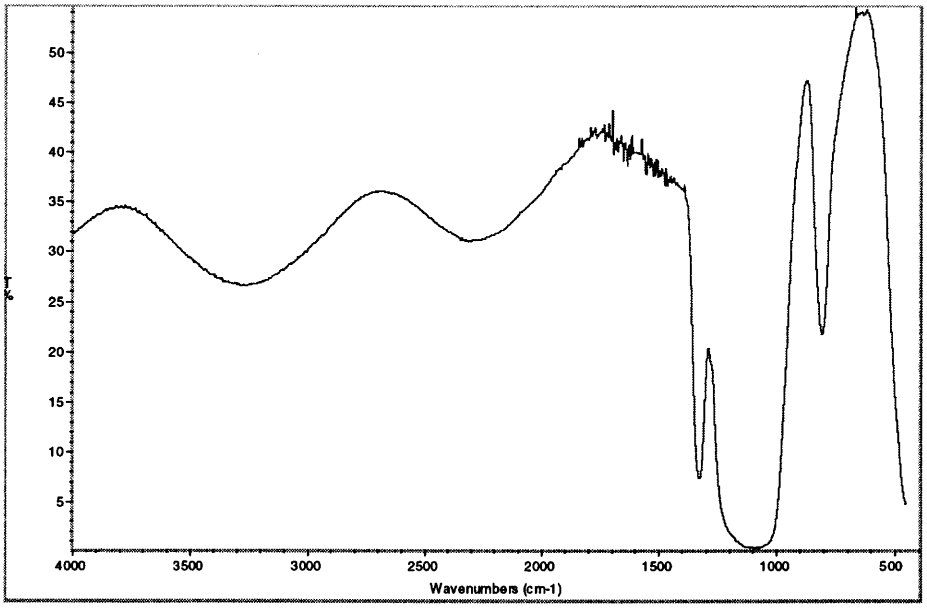

Fig. 4.31 FTIR of PSG film at temperature = 500 ^{0}C and TMP=3sccm

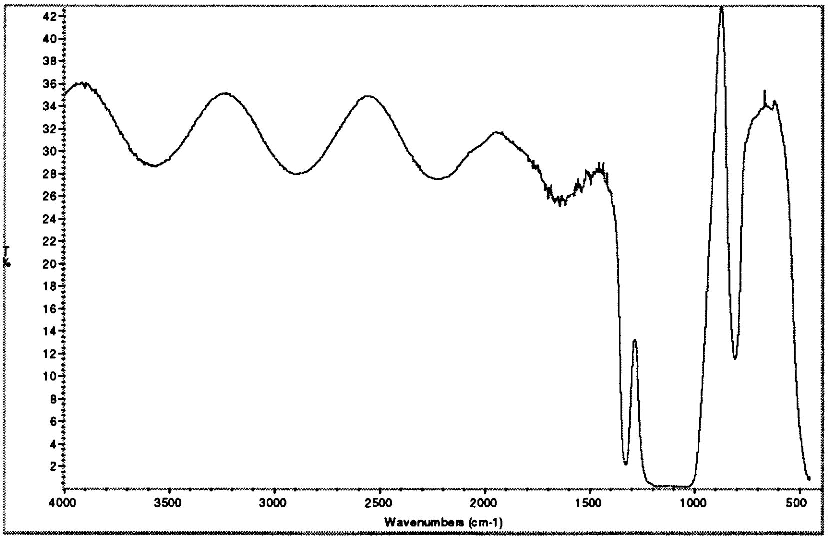

Fig. 4.32 FTIR of PSG film at temperature = 600 ^{0}C and TMP=3sccm

The optical transmission of the phosphosilicate glass was measured using the UV/Visible spectrophotometer and the result is shown in Fig. 4.33. It was seen that a near perfect transparent film was obtained. Optical transmission was an important property to be considered for building an interferometer. A more than 99 % transmission showed that the phosphosilicate glass obtained from LPCVD of DES, TMP and oxygen was an excellent core material for the waveguide

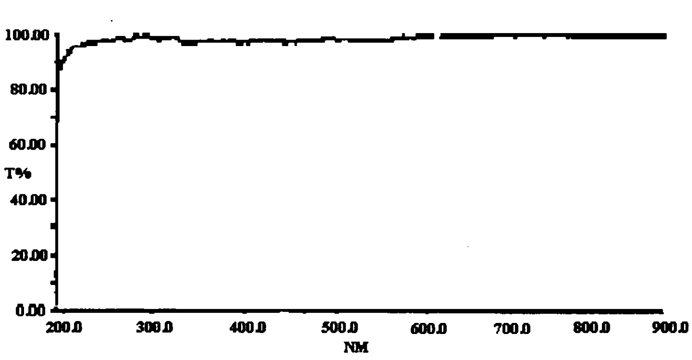

Fig. 4.33 UV spectrum for phosphosilicate glass

4.2.8 Reactive Ion Etching of PSG

PSG was used as the core material and etched 7 μm to get waveguides pattern. Since the polymer was very difficult to be removed, this deep etching could not be processed in the clean room of NJIT and the wafer had to be sent out. But the effects of power and pressure was still studied and presented below.

The etch rate was improved by increasing the RF power as shown in Fig. 4.34. The higher the power, the easier to is to get white polymer film. The effect of the pressure on the etch rate of PSG was less significant than that of the power. Increasing pressure could increase the etch rate as shown in Fig. 4.35, and meantime, the white film was formed as well.

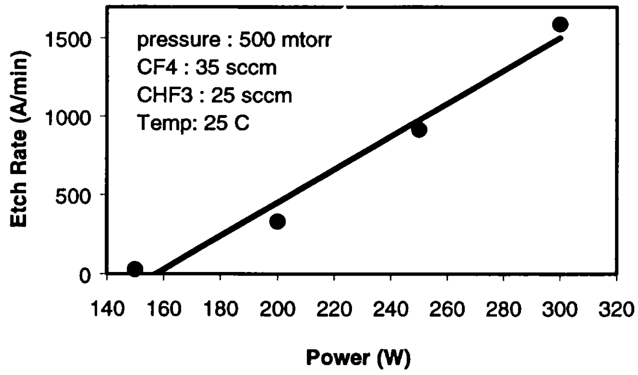

Fig. 4.34 Effect of the power on etch rate of PSG in RIE system

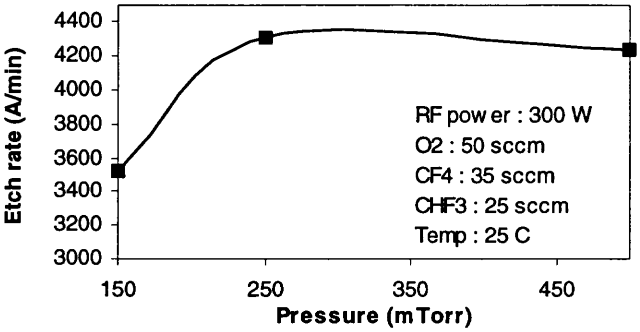

Fig. 4.35 Effect of the pressure on the etch rate of PSG in RIE system

4.3 Waveguide Pattern

The resulting waveguide dimensions were measured with Dektak profilometer, and the results are shown in Fig. 4.36 and Fig. 4.37. As seen from the profile in Fig. 4.37, the etching was not completely in the vertical direction. The average width of a waveguide was 30 μm at the bottom, and 6 μm at the top. The ratio of the bottom width to the top width for per micron described the deviation from the perfect anisotropic etch. The average height for each waveguide was 7.1 μm.

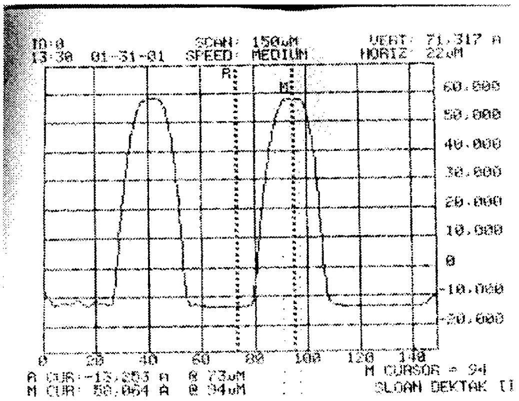

Fig. 4.36 Profile of the pattern of a pair of waveguide

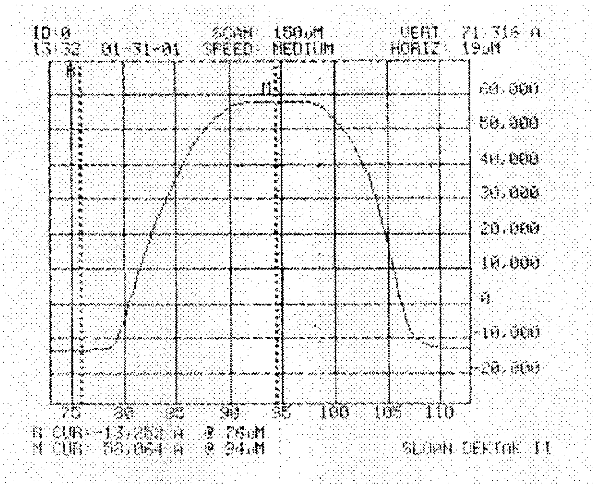

Fig. 4.37 Profile of the pattern of a single waveguide (width = 6 µm)

4.4 PECVD Kinetics of Silicon Dioxide

PECVD silicon dioxide was used as the upper cladding layer since its refractive index was easy to control and the growth rate was high (~ 430 Å/min). The deposition condition is listed in table 3.7. The deposited SiO_2 film had a thickness with a value of ~1.2 µm, a refractive index of 1.453, and the thickness deviation was less than 0.5% across the entire wafer. But the stress was a little high and around 110 Mpa compressive. PECVD SiO_2 film over the sampling arm (window) was removed by the reactive ion etch. The etch rate was 507 Å/min (Fig. 4.38) at the condition listed in table 3.6.

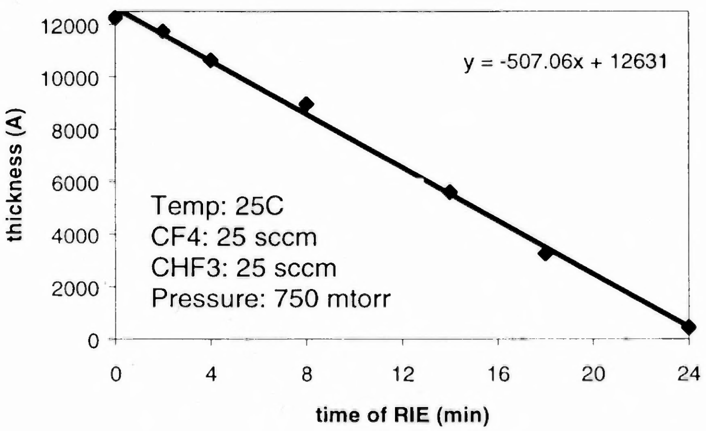

Fig. 4.38 Thickness change of PECVD SiO_2 as the function of RIE time

4.5 Products Analysis

The fabricated device is shown from a top view (Fig. 4.39). The sampling arm is seen to be separated a distance of 50 μm from the reference arm. The dimension of the interferometer is 3 μm in width by 2 mm in length. At both ends the two Y-splitters are readily apparent.

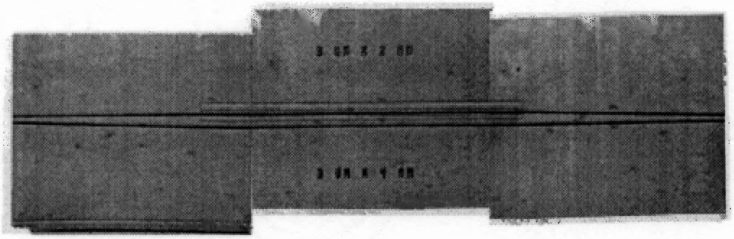

Fig. 4.39 Top view of the Mach-Zehnder interferometer

The cross sections of single waveguide are shown in Fig. 4.40 and Fig. 4.41. It is easier to remove the top PSG from 4 μm waveguide than from 5 μm waveguide during reflowing although they have the same height.

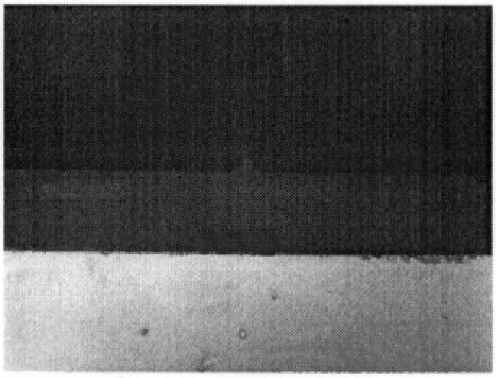

Fig. 4.40 Cross section of 4 μm single waveguide

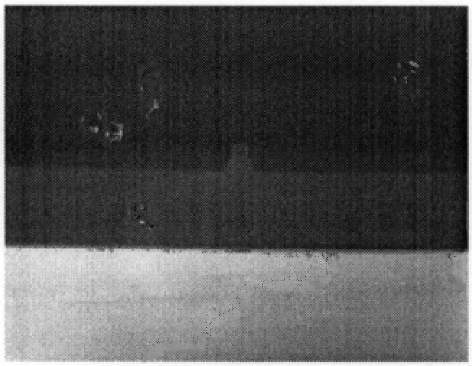

Fig. 4.41 Cross section of 5 μm single waveguide

The cross section profiles of a pair of adjoining waveguides are shown in Fig. 4.42 and Fig. 4.43. Waveguides were cut just before the windows. Fig. 4.42 depicts two 5 μm × 8mm waveguide arms which look identical. Fig. 4.43 is the cross section of 6 μm × 8mm waveguides. The diagram is illuminating both arms with the same dimensions, which is the critical condition of interference for the Mach-Zehnder interferometer.

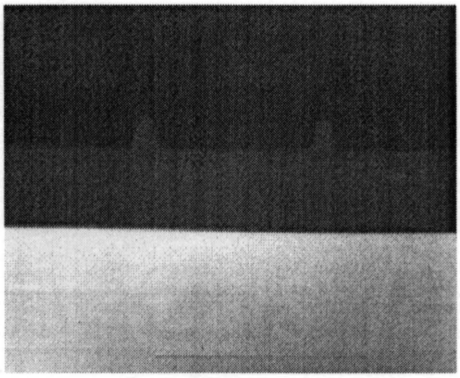

Fig. 4. 42 Cross section of 5 μm × 8mm waveguides

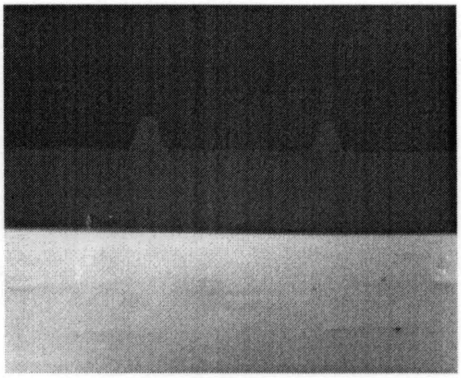

Fig. 4. 43 Cross section of 6 μm × 8mm waveguides

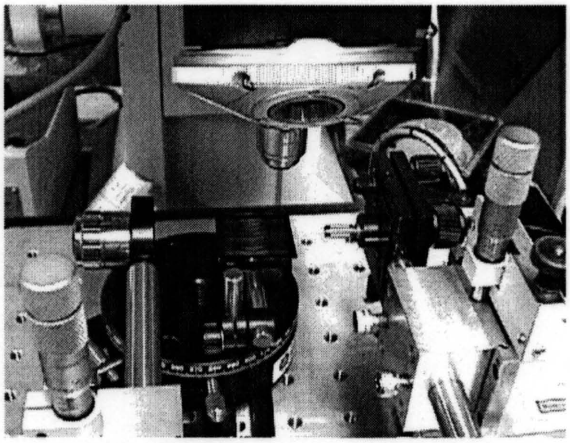

Fig. 4.44 Waveguide coupling experimental set-up

Y-splitter performance was tested by using 628.3 nm helium-neon laser in the set-up shown in Fig. 4.44. In Fig. 4.45 and Fig. 4.46 a pair of light beams of equal intensity are shown after emerging from Y-splitter of different sensors and captured by the CCD camera. Two beams are separately coming from the sampling arm and reference arm. With mirror they could produce interference. These diagrams indicate that Y-splitter worked properly and split the beam evenly.

Fig. 4.45 Image after light go through 5 μm × 8mm waveguides

Fig. 4.46 Image after light go through 6 μm × 8mm waveguides

Fig. 4.47 shows the light going through a single waveguide. There is no change between the intensity of air environment and water environment since the cladding layer is thick enough. The optical loss is mainly due to the coupling.

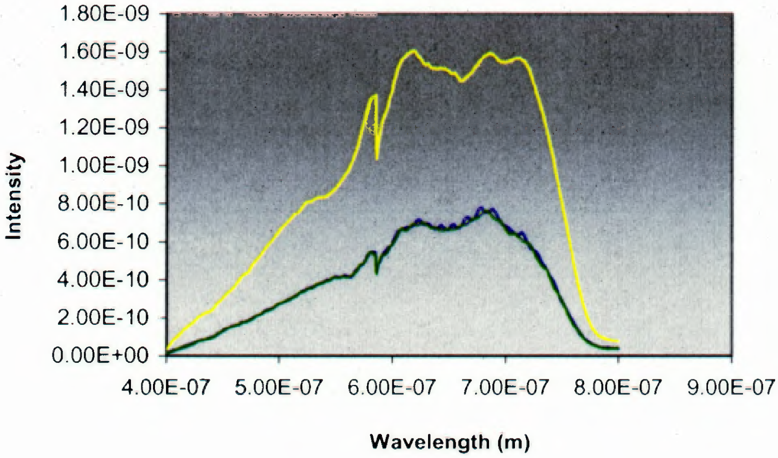

Fig 4.47 Output intensity of a single waveguide as the function of wavelength (Yellow-intensity of light, Blue-air, Green-water)

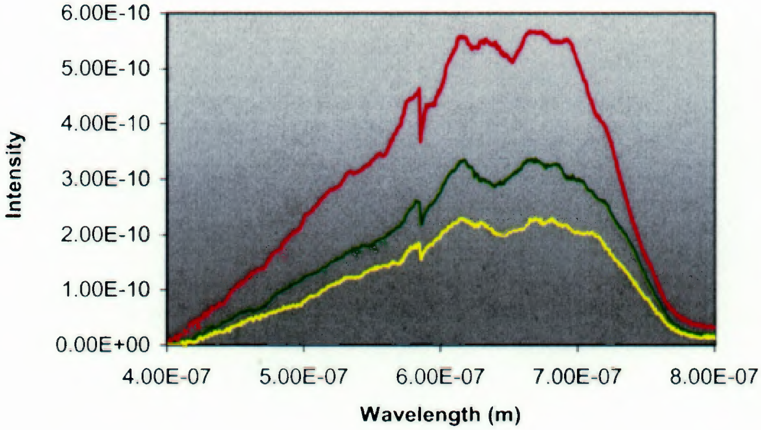

Fig 4.48 Output intensity of different waveguide as the function of wavelength (Red-half single waveguide, Green-half reference arm, Yellow-half sampling arm)

Fig 4.48 is the comparison of the output intensities of the single waveguide, the reference arm and the sampling arm. The sampling arm has higher loss than that of the reference arm because of the open window. The longer the window, the more the optical loss. It is shown in Fig 4.49 as well.

Fig 4.50 is the normalized intensity (to water) as a function of the wavelength. The light went through the whole Mach-Zehnder interferometer. The output intensities change with the different solutions. It illustrates the integrated Mach_Zehnder interferometer of the study is sensitive to the change of the solutions and can work properly.

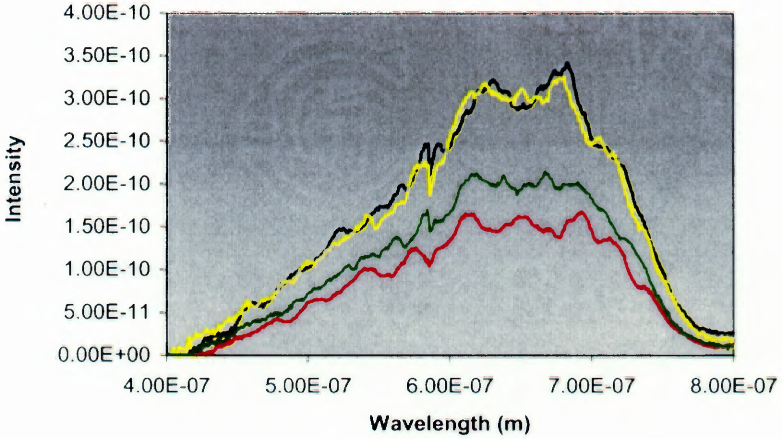

Fig 4.49 Output density of MZI as the function of wavelength (Red-half 6×10 sampling arm, Black-half 6×10 reference arm, Yellow-half 6×2 reference arm, Green-half 6×2 sampling arm)

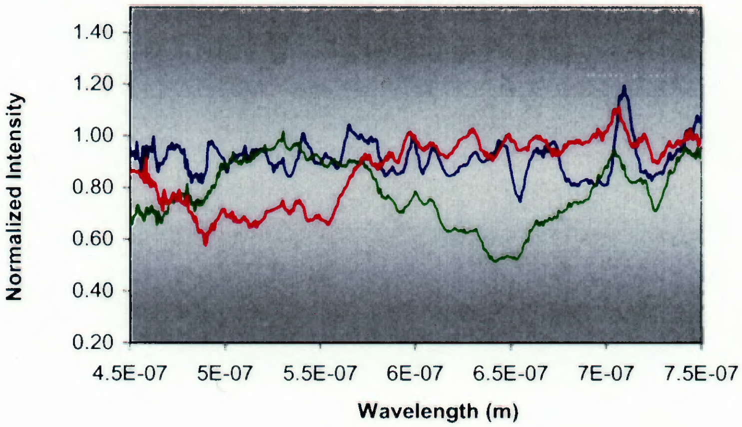

Fig 4.50 Normalized intensity as the function of wavelength (Blue-air, Red-red water, Green-green water)

CHAPTER 5

CONCLUSIONS

In this study, the principles of interferometry were used to produce a novel integrated photonic sensor capable of monitoring and determining in-situ the concentration of numerous analyte species. The sensor has been designed to be compact, portable, rugged, and suitable for real-time monitoring of hazardous emissions. It offers numerous advantages over conventional analytical techniques such as gas chromatography and mass spectrometry including small physical size, geometric flexibility, environmental versatility, real-time and in-situ analysis, instrumental reliability, analyte specificity, insensitivity to electromagnetic interference, and low power requirements. The fabrication of this sensor is based on large scale integrated (LSI) circuit-type processes which allow for a high degree of electronic and photonic integration. In addition to offering the advantage of miniaturization, this technology offers high throughput (hundreds of sensors per silicon wafer) that translates into low cost per device.

This dissertation has mainly focused on the design, fabrication, and test of the integrated photonic sensor for the purpose of monitoring hazardous organics in the environment. The design of the sensor is based on the principles of the Mach-Zehnder interferometer that is constructed from a single mode waveguide. The waveguide consists of a Y-shaped splitter that divides an incident guided optical mode into each arm of the interferometer and interferes the resulting guided optical modes at an emerging Y- shaped splitter. One of the arms of the interferometer is covered by a protective oxide layer to give it a constant effective refractive index, while the other is exposed to the environment through a "window" in the protective layer to allow the effective index of the guide to vary with external conditions. The two resulting modes are interfered which results in an intensity change of the output signal that depends on the differences in the effective indices of each guide. In order to have a single mode planar waveguide, the width of the guide must be determined for the single mode operation. The Mach-Zehnder interferometeric structures that constitute these guides have been designed as a TE single mode waveguide. The operated wavelength and width of the waveguide can be determined by the field distribution and normalized frequency. The fabrication of the sensor involve two lithographic masks, one for patterning the waveguides, and the other for opening windows through the top cladding layer. Two masks were designed with Mentor graphics IC Station on a Sparc 20 workstation network. In order to test the sensor under a variety of waveguide dimensions for optimal performance, several different types of sensors were created with varying lengths and widths.

The test waveguide was fabricated on 5 inches wafers with <100> orientation. A 15μm thick SiO_2 film was synthesized by low pressure chemical vapor deposition (LPCVD) to act as lower cladding material for the waveguide and prevent light from coupling with the underlying silicon. A 7 μm thick phosphrous-doped LPCVD film was synthesized to act as core material for the waveguide. This layer was patterned using a standard lithographic exposure and etch techniques, and subjected to anneal to cause viscous flow and round off the edge. This round-off procedure is necessary to minimize coupling losses between fiber and waveguide. The refractive index of the doped glass was measured to be near 1.466, thus, producing with the underlying SiO_2 (n_l=1.458) cladding a single mode waveguide device. Deposition of 1.2 μm thick undoped SiO_2 buffer layer over the entire wafer and a subsequent lithographic step resulted in selective removal of that layer over the sampling arm of the interferometer. This configuration allows for exposure of the sampling arm (uncoated or coated) to various contaminants in the environment that cause a change in the effective

Table 5.1 Summary of fabrication condition of waveguide

	SiO_2 (underlying cladding)	PSG (core material)	SiO_2 (upper cladding)
Methods	LPCVD	LPCVD	PECVD
Temperature (°C)	775	600	250
Pressure (mTorr)	200	250	900
O_2 flow rate (sccm)	100	100	900 sccm (N_2O)
DES flow rate (sccm)	10	10	400 sccm (3% SiH_4)
TMP flow rate (sccm)	0	2	0
Deposition time	19 Hr 25 min	4 Hr 40 min	30 min
Thickness (μm)	15.37	6.61	1.2
Refractive Index	1.458	1.466	1.453
P wt%	0	7.96	0
Growth rate (Å/min)	132	236	430
Stress (Mpa)	20 (C)	0.93 (C)	110 (C)

index of that arm. The arm coated with the SiO_2 buffer layer saw a refractive index of n = 1.453. Three, four, five, and six microns-wide waveguides formed the two interferometer paths using a splitting angle of 2^0. The sampling and reference arms had a fixed separation of 50 μm and variable lengths. The fabrication conditions of the waveguide are summarized in table 5.1.

The test set-up of the integrated photonic sensor include a Hitachi laser diode, a Thorlabs laser diode controller, a single mode optical fiber (5.5 μm core diameter), microscope, SBIG CCD camera, monitor and video capturing board. Light was coupled into the waveguide and the output intensity was measured for the different solutions placed on the sampling arm. The laser beam was collimated and then focused to the fiber by an aspheric lens. The alignment between the fiber end and waveguide was optimized by using a microscope and Newport XYZ transitional stage. The light emerging from the waveguide was imaged and captured by a CCD camera. In order to test the sensitivity of the sensor to the pollutants, water as well as different ethanol solutions were prepared and dropped on the sample arm. A small refractive index change occurred when ethanol was mixed in water. The corresponding change in interferometric output image was captured by the CCD camera.

This program has succeeded in developing the technology required to design, model, fabricate, and test a novel integrated photonic sensor capable of monitoring VOC contaminants in water. It represents a technology platform that can be readily extended to monitor and quantify simultaneously multicomponent mixtures in water and air in the future.

REFERENCES

1. E.P. Meulenberg and P.G. Stoks, *Anal.Chim.Acta* 1995, 311, 407-413.
2. E.F. Schipper, S.Rauchalles, and R.P.H. Kooyman, *Anal. Chem.*, 1998, 70(6), 1192-1197.
3. P. Kramer and R.D. Schmid, *Biosens. Bioelectron.* 1991, 6, 239-243.
4. M. Minunni and M. Mascini, *Anal. Lett.* 1993, 26, 1441-1460.
5. F.F. Bier and R.D. Schmid, *Biosens. Bioelectron,* 1994, 9, 125-130.
6. A. Brecht, J. Piehler, and G. Lang, *Anal.Chim.Acta* 1995, 311, 289-299.
7. W. Lukosz, *Biosens. Bioelectron.* 1991, 6, 215-225.
8. R.G. Heideman, R.P.H. Kooyman, and J. Greve, *Sens. Actuators,* B1993, 10, 209- 217.
9. A.T. Lenferink, E.F. Schipper, and R.P.H. Kooyman, *Rev.Sci. Instrum.* 1997, 68, 1582-1586.
10. E.F. Schipper, R.P.H. Kooyman, and J. Greve, *Sens. Actuators*, B1995, 24-25, 90-93.
11. Hecht Eugene; *Optics*, third edition, 1998.
12. J. Burck, J.P. Cozen, and B. Beckhaus, *Sens. Actuators*, B18-19, 1994, 291.
13. Z. Ge, C.W. Brown, and J.J. Alberts, *Environ. Sci Technol.*, 1995, 878.
14. J. Sensfelder, J. Burck, and H.J. Ache, *Anal. Chem.*, 1996, 848.
15. Milton Ohring, *The materials Science of Thin Film*, 1992, 149-154.
16. T. Mizutani, M. Yoshida, and A. Usui, *J. Appl. Phys. 19* 1980, 113.
17. William F Smith, P*rinciples of Materials Science and Engineering,* 3rd ed.
18. O. Kubaschewski and E.L. Evans, *Metallurgical Thermochemistry,* 1958.
19. D.R. Stull and H. Prophet, *JANAF Thermochemical Tables,* 2nd ed., 1971.
20. A.S. Grove, P*hysics and Technology of Semiconductor Devices,* 1967.

21. J. Bloem and W.A.P. Claassen, *Philips Tech. Rev. 41*, 1983, 60.

22. Stephen A. Campbell, *The Science and Engineering of microelectronic Fabrication,* 1996.

23. M.S. Kim and J.S. Chun, *Thin Solid Film, 107,* 1983.

24. W. Kern and R.A. Levy, *Chemical Vapor Deposition, Microelectronic Materials and Processes,* 1986, 203.

25. Milton Ohring and D.R. Bradbury, *The Materials Science of Thin Films,* 1992.

26. Michael L. Hitchman and Klavs F. Jensen; *Chemical Vapor Deposition Principles and Applications,* 1993.

27. W. Peters, F.L. Gebhart, and T.C. Hall, *Solid state Technol., 23(9);*1980, 121.

28. J.W. Peters, *IEEE-IEDM Tech. Dig.,*1981, 240.

29. S.D. Allen and A.B. Trigubo, *Chemical Vapor Deposition, The electrochemical Society;* 1981.

30. S.V. Nguyen and A. Nguyen, *J. Electrochem. Soc., 141;* 1994; 1635.

31. K. McAndrews and P.C. Subanek, *Nonuniform Wet Etching of Silicon Dioxide*, J.Electrochem. Soc., 138, 863, 1991.

32. Stephen A. Campbell, *The Science and Engineering of Microelectronic Fabrication*, Oxford University, New York Press 1996.

33. Y. Ozawa and S. Lida, *Fourth Optoelectronics Conference;* 1992, 68.

34. Ryozo Yamauchi, *Fourth Optoelectronics Conference, Julyh* 1992, 66.

35. Michael D. Degrandpre and Lloyd W Burgess, *Appl. Spectroscopy V44,* 1989, 273-279.

36. J. Burck, J.P. Conzen, and B. Bechhaus, *Sensors and Actuators B, 18-19,* 1994, 291.

37. Dianna S. Blair and Lloyd W. Burgess, *Applied Spectroscopy V49,* 1995, 1636.

38. J.P. Corzen and J. Burck, *Applied Spectroscopy V47,* 1993, 753.

39. Hideo Tai and Hiroaki Tanka, *Optics Letters V12, No 6,* 1987.

40. E. Sensfelder and J. Burck, *J Anal Chem;* 1996, 354:848-851.

41. ZhengFang Ge and C.W. Brown, *Environ. Sci. Technol, 29,* 1995, 878-882.

42. P. Heinrich and B. Schrader, *Applied Spectroscopy, V44,* 1990, 1641.

43. R. Krska and K. Taga, *Fresenis Anal Chem. 342,* 1992, 202.

44. B. Zimmermann and J. Burck, *Siliconpolymer-System, KFK Rep. 4967,* 1991.

45. E.R. Adlard, *J. Inst. Pet.*1972, 58-63.

46. R.E. Baier, *J. Geographys. Res.V77,* 1972, 5062.

47. R.D. Cole, *J. Inst. Pet. V54,* 1968, 288.

48. F.K. Kawahara, *Environ. Sci. Technol. V3,* 1969, 150.

49. J.S. Mattson, *Anal Chemical. V 43,* 1971, 1872.

50. J. Burck and J.P. Conzen, *Fresenius J.Anal.Chem. 342;* 1992, 394.

51. J.F. Place and R.M. Sutherland, *Biosensors,* 1985, 321.

52. M.A. Powell and A.O. Donnell, *Opticas & Photonics News,* 1997, 23.

53. E. Bonnotte and C. Gorecki, *J. of Lightwave Technology, V17, No1,* 1999, 35.

54. A.J. McLaughlin and J.R. Bonar, *CLEO'98, CThB5,* 1998.

55. R.G. Hunsperger, *Integrated Optics: Theory and Technology,* 1991, 124.

56. Neil S Lagali and Mohammad R Paiam, *J.of Lightwave Tech. V17, No12,* 1999, 2542.

57. Naoto Yoshimoto and Yasuo Shibata, *Photonics Technology Letter, V10, No4,* 1998, 531.

58. B.J. Luff and J.S. Wilkinson, *Journal of Lightwave Tech., V16, No4,* 1988, 583.

59. Claude Rolland, *OFC '98 Technical Digest,* 1998, 283.

60. S. Khalfallah and P. Dubreuil, *Optics Communications, 167,* 1999, 67.

61. P.R. Longaker and M.M. Litval, *J.Appl.Phys., 40, 4033,* 1969.

62. Anthony Boiarski and Balwant Bhullar, *Scientific Conference on Chemical Defense Research,* 1993.

63. Rene Heidman and R.P.H. Kooyman, *Sensors and Actuators B4,* 1991, 297.

64. Rene Heidman and R.P.H. Kooyman, *Sensors and Actuators B10,* 1993, 209.

65. E.F. Schipper andA.M. Brugman, *Sensors and Actuators B40,* 1997, 147.

66. E.F. Schipper and S. Rauchalles, *Ansl. Chem., 70(6),* 1998, 1192.

67. K. Tiefenthaler and W. Lukosz, *Opt. Soc. Am. B6,*1998, 209.

68. W. Lukosz, *Biosensors Bioelectron., 6,* 1991, 215.

69. D. Jimenez and E. Bartolome, *Optics Communications 132,*1996, 437.

70. E. F. Schipper and R.P.H. Kooyman, *Biosensor & Bioelectronics V11, No3,* 1996, 295.

71. Matti Leppihalme and Timo Aalto, *Proceeding of SPIE, V3936,* 2000.

72. M. Modreanu and P. Cosmin; *LPCVD Silicon oxynitride From Dichlorosilane, Nitrous Oxide and Ammonia; IEEE;* 1995.

73. Kevin K. Lee and Desmond Lim, *Proceeding of SPIE,* 1999, 120.

74. Tim Bestwick, *Proceeding of SPIE,* 1999, 182.

75. Richard A. Soref, *Proceeding of SPIE,* 1990, 408.

76. Tim Bestwick, *Mat.Res. Soc. Symp, V486,* 1998, 57.

77. Rene M. DeRidder, *J. of Quantum Electronics, V4, No6,* 1998, 930.

78. Y.P. Li and C.H. Henry, *IEE Proc.-Optoelectron., Vol 143, No 5,* 1996.

79. E. McGoldrick and S.D. Hubbard, *Proceeding of SPIE, V1374,* 1990, 118.

80. B.H. Verbeek and C.H. Henry, *J.of Lightwave Tech.* 1988, 1011.

81. C.C. Li and Fan Qian, *Conference of SPIE, V3630,* 1999.

82. C.H. Henry, *IEEE LEOS Annual Meeting, Proceeding 2;* 1994, 245-246.

83. R.A. Levy, J.M. Grow, and G.S. Chakravarthy, *Chem. Mater.*,1993, 5, 1710.

84. W.A. Brown and T.I. Kamins, *Solid State Technol.*, 1979, 22 (7), 51.

85. C.M. Drum and M.J. Rand, *J. Appl. Phys.*,. 1968, 39 (9) 4458.

86. L. Zambov, G. Peev, V. Shanov, and S. Drumeva, *Vacuum., ibid,* 1992, 43, 227.

87. J.T. Cotler and J. Chapple-Sokol, *J.Electrochem.Soc.*;140 (7) ,1993.

88. A.C. Adams and C.D. Capio, *J.Electrochem. Soc.,* 1979, 126, 1042.

89. F. Fracassi, R. d'Agostino, and P. Favia, *J.Electrochem.Soc.;* 139 (9), 1992, 2636.

90. C.S. Pai and C.P. Chang, *J.Appl. Phys.*, 1990, 68, 793.

91. C.P. Chang, C.S. Pai, and J.J. Hiseh, *J.Appl. Phys.*, 1990, 67, 2119.

92. M.G. Veprek-Heijman and D. Bontand, *J.Electrochem. Soc.*,1991,138, 2042.

93. T. Emesh, G. D'Asti, J.S. Mercier, and P. Leung, *J.Electrochem.Soc* 1989, 136, 3404.

94. P.G.T. Evert and Van de Ven, *Solid State Tech.*, 1981, 24 (4), 167.

95. U. Mackens and U. Merkt, *Thin Solid Films*, 1982, 97, 53.

96. B.L. Chin, P.G.T. Evert, and Van de Ven, *Solid State Technol.*, 1988, 31 (4), 119.

97. C.S. Gorthy, MS. Thesis, Dept. of Matl. Sci. & Engg., New Jersey Institute of Technology, Newark, New Jersey, 1992.

98. A.C. Adams, *"Dielectric and polysilicon Flim Deposition in VLSI design"* 1983, 93.

99. J. Klerer, *J. Electrochem. Soc.112,* 1965, 503.

100. J.M. Albella and A. Criado, *Thin Solid Film, 36,*1976, 479.

101. J. Klerer, *J. Electrochem. Soc.108,* 1961, 1070.

102. E.L. Jordan, *J. Electrochem. Soc.108,* 1961, 478.

103. G. Smolinsky and R.E. Dean, *Mater. Lett., 4,* 1986, 256.

104. R.A. Levy and P.K. Gallagher, *Electrochem. Soc., 134,*1987, 1744.

105. R.A. Levy and J.M. Grow, *Chem Mater., 5,* 1993, 1710.

106. S. Wolf and R.N. Tauber, *Silicon Processing for the VLSI Era,* 1986.

107. A.C. Adams and C.D. Capio, *J.Electrochem. Soc.,* 1979, 126, 1042.

108. T.Y. Tien and F.A. Hummel, *J A M Ceram Soc.,Vol 45,* 1962, 422.

109. J.M. Eldridge and P. Balk, *Tans. Met Soc.AIME, V242,* 1968, 539.

110. N. Nagasima and H. Suzuki, *J Electronchem. Soc.,:Solid-State Science and Technoloy,V121, No 3,* 1974, 434.

111. N. Nagasima, *J appl.Phys., Vol 43.,*1972, 3378.

112. W.A. PlisKin and H.S. Lehman, *J Electronchem. Soc.,:Solid-State Science and Technoloy, V112,* 1965, 1013.

113. J.W. Mayer and S.S. Lau, *Electronics Materials Science: For Integrated Circuits In Si and GaAs, Macmillan,* 1990.

114. G.L. Schnable and W. Kern, *J Electronchem. Soc.,:Solid-State Science and Technoloy,V122, No 8,* 1993, 1092.

115. A.C. Adams and S.P. Murarka, *J.Electrochem. Soc.*, 1979, 334.

116. T.D. Bonifield, *Deposition Technologies for Films and Coatingbs,* Noyes, New Jersey, 1982.

117. Leon I. Maissel and Reinhard Glang, *Handbook of Thin Film Technology,*197 Chap3-7.

118. Wu Wen Fa and Chiou Bi Shiou, *Semiconductor Science and Tech.,* 1996, 1317.

119. Y. B. Choi and S.J. Park, *The Fourth Optoelectronics and Communication Conference, Volume 2,* 1999, 1634.

120. Norman G. Einspruch, *VLSI Handbook, NewYork,* 1985.

121. Thomas O. Sedgwick, *Rapid Thermal processing, V52,* 1986.

122. S. Sivoththaman, *Materials Res. Soc. Symposium, V387*, 1995, 259.

123. S. Nakashima and T. Katayama, *J. of Electrochemical Soc.* 1996, 244.

124. Li Cheng Chung, *Conference of Laser and Electro,* 1997, 1092.

125. R.M. Wood and A.C. Greenham, *Proceeding of SPIE,V1441,* 1990, 316.

126. J.M. Senior;*Optical Fiber Communication Principle and Practice,* 1985.

127. J.M. Ruano and D. Ortega, *Mocroelectronics Engineering,V46,* 1999,419.

128. A.J. Mclaughlin and J.A. Bonar, *Conference Proceeding-Lasers and Electro- Optic-Society Annual Meeting, V11,* 1997, 508.

129. A. Kilian and J. Kirchhof, *J of Lightwave Tech. V18,* 2000, 193.

130. S. McCulloch and G. Stewart, *International J of Optoelectronics;* 1994, 235.

131. A. Schroth and C. Lee, *Proceeding of IEEE;* 1998, 402..

132. A. Brandengurg and R. Edelhauser, *Sensors and Actuators,B11,*1993, 361.

133. A.N. Sloper and M.T. Flanagan, *Sensors and Actuators, B11,* 1993, 537.

134. A.A. Boiarski and R.W. Ridgeway, *SPIE, V1368,* 1990.

135. N. J. Harrick, *Internal Reflection Spectroscopy, New York,* 1967.

136. D. Gloge, *Appl.Opt.10,* 1971, 2252.

137. A. Yariv, *Optical Electronics in Modern Communication;* 1991.

138. A.S. Tenny and M. Ghezzo, *J Electronchem. Soc.:Solid-State Science and Technology; V140; No9;* 1973,1276.

139. Quick reference manual for silicon integrated circuit technology, 1-20.